Design, Fabrication and Characterization of Micromachined THz Absorbers

by
Ayda Mamaghani
M.S., Electrical and Electronic Engineering, Boğaziçi University, 2012

Submitted to the Institute for Graduate Studies in
Science and Engineering in partial fulfillment of
the requirements for the degree of
Doctor of Philosophy

Graduate Program in Electrical and Electronics Engineering
Boğaziçi University
2020

ACKNOWLEDGEMENTS

It is my great chance to have unique and supporting people around me. In all of my life stages, my beloved ones surrounded me with their care and enthusiasm. Of course achieving successes and aims have not come true without their presence. Foremost, I would like to express my sincere gratitude to my advisor Prof. Dr. Arda Yalcinkaya, and Co-advisor Assoc. Prof. Dr. Hamdi Torun for the continuous support of my Ph.D. study and research for their patience, motivation, enthusiasm, guidelines, and immense knowledge.

I would also like to thank Prof. Gunhan Dundar, Assoc. Prof. Dr. Onur Ferhanoğlu, Assist. Prof. Dr. Baykal Sarioglu and Assist. Prof. Dr. Sema Dumanli Oktar for taking part as committee members of my thesis defense and their valuable comments to improve my thesis.

In this way, I would like to express my most profound appreciation to my parents. My mother Mahnaz, who has been stayed beside me whit her unconditional love throughout my journey, made my hopes and wishes come true to this moment. Most importantly, I would like to express my profound gratitude to my beloved father, Mir Eisa, for his endless support, encouragement, and consistency. Besides my parents, my beloved sister Dr. Ainaz Sadeghzadeh has the symbols of them; without her encouragement, I would not finish this level. I can not pass without mentioning that motivation comes from my brothers Dr. Arman and Dr. Arvin Sadeghzadeh. Last but not least, I would like to thank my husband, Dr. Emir Mamaghani, for supporting me spiritually. I appreciate my son Aren Pasha. His presence in my life made me concentrated on my aims and goals.

This work was dedicated to my beloved uncle, Hassan Amu, who had started the adventure of my learnings from the very beginning with alphabet instruction.

ABSTRACT

Design, Fabrication and Characterization of Micromachined THz Absorbers

The purpose of this research is to develop a new class of THz absorbers for imaging and sensing applications that can provide improved functionality and performance. These absorbers consist of periodic arrays of layered cells made of a back-plane metal layer, opaque to transmitted radiation, a dielectric substrate as a spacer, and a metallic patterned layer as resonating part. Once electromagnetic wave impinges, the structure reflects the incident wave, except in a specific frequency band determined by the absorber's physical properties. In the presence of a blocking layer which eliminates transmitted power, absorption in that specific frequency band occurs. The effective permittivity and permeability of absorber unit cell reach the same value and be negative simultaneously to have perfect absorption. Negative values of ϵ and μ do not happen in nature. At this point, "metamaterials" are introduced. Metamaterials (MMs) are artificially engineered structures used in THz absorbers. MMs' concept is derived from replacing the natural materials with engineered materials where their sizes are much smaller than the given wavelength. Intriguing properties of MM are achieved from the degree of the skillfulness of its structure (geometry, shape, orientation, and size), while its chemical construction plays an insignificant role. Currently, THz absorbers are in use as medical and security applications. Many types of MM based absorbers have been introduced based on their shapes, sizes, and configurations. This research has focused on absorbers with a low dependency of absorber's performance on the exciting wave's incidence and polarization angle. Besides, we demand these structures to operate in a wide range of frequency spectra designed to, with small dimensions of the patterned array compared to the wavelength; in other words, we concentrate on the design of wideband THz absorbers.

In Chapter 1, we start with a brief introduction to THz radiation and its benefits and applications. It also comprises an overview of the history and theory of MMs. Various designs demonstrating the performance and operating frequency bands of MMs and their applications have been studied. A comprehensive study of wave propagation in the right and left-handed media is presented in Chapter 2. Basic models of proposed MM absorbers are introduced in Chapter 3. The principle of resonance is based on a lumped LC circuit and broadband operation provided in this chapter. Afterward, the design, Fabrication, and characterization of a MEMS-based THz metamaterial-based absorber are described in Chapter 4. A new 3D design inspired by honeycomb structures as broadband and incident wave independent absorber has been proposed. Chapter 5 includes the design, simulation, fabrication process, and measurement results of this 3-dimensional MM based broadband absorber. The proposed absorber exhibits excellent absorption characteristics. The unique feature of the proposed approach is having very low sensitivity with respect to the incidence angle. The ability to maintain their absorption properties in THz frequencies, unlike their small feature sizes compared with traditional approaches, made these porous structures attractive for sensing applications. Throughout this dissertation, both physical and numerical interpretations of the spectral behavior of new designs are provided. Physical insight into the operating mechanism is the key to further improvements and creates more complex surfaces with desired frequency responses.

ÖZET

Mikro İşlenmiş THz Emicilerin Tasarımı, Üretimi ve Karakterizasyonu

Bu araştırmanın amacı, gelişmiş işlevsellik ve performans sağlayabilen uygulamaları görüntüleme ve algılama için yeni bir THz soğurucu sınıfı geliştirmektir. Bu soğurucular, bir arka düzlem metal katmandan, iletilen radyasyona opak, aralayıcı olarak bir dielektrik substrattan ve rezonans parçası olarak metalik desenli bir katmandan oluşan katmanlı hücrelerin periyodik dizilerinden oluşur. Elektromanyetik dalga çarptığında, yapı, soğurucunun fiziksel özellikleri tarafından belirlenen belirli bir frekans bandı dışında, gelen dalgayı yansıtır. İletilen gücü ortadan kaldıran bir engelleme tabakasının varlığında, bu özel frekans bandında emilim meydana gelir. Emici birim hücrenin etkin elektriksel geçirgenliği ve manyetik geçirgenliği aynı değere ulaşır ve mükemmel soğurmaya sahip olmak için aynı anda negatif olur. ϵ_r ve μ_r negatif değerleri doğada görülmez. Bu noktada "metamalzemeler" tanıtılmaktadır. Metamalzemeler, THz emicilerde kullanılan yapay olarak tasarlanmış yapılardır. MM'lerin konsepti, doğal malzemelerin moleküllerini ve atomlarını, boyutları verilen dalga boyundan çok daha küçük olan mühendislik malzemeleriyle değiştirmekten türetilmiştir. MM'nin ilgi çekici özellikleri, yapısının (geometri, şekil, yönelim ve boyut) becerisinin derecesinden elde edilirken, kimyasal yapısı önemsiz bir rol oynar. Şu anda, THz emiciler tıbbi ve güvenlik uygulamaları olarak kullanılmaktadır. Şekillerine, boyutlarına ve konfigürasyonlarına bağlı olarak birçok MM tabanlı emici türü tanıtılmıştır. Bu araştırma, emicinin performansının EM dalgasının gelişi ve polarizasyon açısına düşük oranda bağımlı olduğu emiciler üzerinde odaklanmıştır. Ayrıca, bu yapıların, dalgaboyuna kıyasla dizinin küçük boyutları ile tasarlanmış çok çeşitli frekans spektrumlarında çalışmasını talep ediyoruz; diğer bir deyişle, geniş bantlı THz soğurucuların tasarımına odaklanıyoruz.

Bölüm 1'de, THz radyasyonuna ve faydalarına ve uygulamalarına kısa bir girişle başlıyoruz. Aynı zamanda MM'lerin tarihi ve teorisine genel bir bakış içerir. MM'lerin performansını ve çalışma frekans bantlarını ve uygulamalarını gösteren çeşitli tasarımlar incelenmiştir. Sağ ve solak medyada dalga yayılımının kapsamlı bir çalışması Bölüm 2'de sunulmuştur. Önerilen MM soğurucularının temel modelleri ve geniş bantlı emici tasarım Bölüm 3'te anlatılmıştır. Rezonans ilkesi, bu bölümde sağlanan lumped LC devresine dayanmaktadır. Daha sonra, MEMS tabanlı THz metamalzeme tabanlı soğurucunun tasarımı, Üretimi ve karakterizasyonu Bölüm 4'te açıklanmaktadır.

Geniş bantlı ve çarpan dalga açısından bağımsız emici olarak petek yapılarından esinlenen yeni bir 3D tasarım önerildi. Bölüm 5, bu 3 boyutlu MM tabanlı geniş bant emicinin tasarımını, simülasyonunu, üretim sürecini ve ölçüm sonuçlarını içerir. Önerilen soğurucu, mükemmel soğurma özellikleri sergilemektedir. Önerilen yaklaşımın benzersiz özelliği, geliş açısına göre çok düşük hassasiyete sahip olmasıdır. Geleneksel yaklaşımlarla karşılaştırıldığında küçük özellik boyutlarının aksine, soğurma özelliklerini THz frekanslarında muhafaza etme yeteneği, bu gözenekli yapıları algılama uygulamaları için çekici hale getirdi. Bu tez boyunca, yeni tasarımların spektral davranışının hem fiziksel hem de sayısal yorumları sağlanır. İşletim mekanizmasına ilişkin fiziksel içgörü, daha fazla iyileştirmenin anahtarıdır ve istenen frekans yanıtlarıyla daha karmaşık yüzeyler oluşturur.

TABLE OF CONTENTS

LIST OF FIGURES

LIST OF TABLES

LIST OF SYMBOLS

A	Absorptivity *or* cross sectional area of current sheet
a	Lattice constant
a_n	Mean radius of ring
$\tilde{\mathbf{B}}$	Magnetic flux density
C	Capacitance
c	Speed of light
c_0	Speed of light in vacuum
C_{11}	Self capacitance of sphere 1
C_{22}	Self capacitance of sphere 2
C_{12}	Mutual capacitance as a result of charge induction
C_{21}	Mutual capacitance as a result of charge induction
C_L	Left-handed capacitance times unit length
C_m	mutual capacitance between spheres
C_R	Right-handed capacitance per unit length
C_s	Self capacitance of sphere
$\tilde{\mathbf{D}}$	Electric displacement
d	spacing between rings *or* distance between sheets
$\tilde{\mathbf{E}}$	Electric field
E	Energy
f_c	collision frequency of the electrons
g	gap size
$\tilde{\mathbf{H}}$	Magnetic field
h	Planck's constant
$\tilde{\mathbf{J}}$	Current density
$\tilde{\mathbf{k}}$	Wavevector
k	Wavenumber
L	Inductance
L_L	Left-handed inductance times unit length

L_m	mutual inductance between spheres
L_R	Right-handed inductance per unit length
L_S	Self inductance of sphere
l	side length
n	Refractive index
P	Pore size
Q	Quality factor
Q_c	Quality factor of conductor
R	Reflection
R_{in}	Inner ring radius
R_{out}	outer ring radius
R_{sc}	Short circuit resistor
r	radius of wire *or* inner radius of ring
$R_{\parallel}$	Reflection coefficient in TM mode
$R_{\perp}$	Reflection coefficient in TE mode
$\tilde{\mathbf{r}}$	Position vector
r_{12}	Reflection coefficient from media to air
r_{21}	Reflection coefficient from air to media
r_n	Radius of a ring in each segment of sphere
$\tilde{\mathbf{S}}$	Poynting Vector
S_{11}	Reflection coefficient of port 1
S_{12}	Transmission coefficient
T	Transmission
$T_{\parallel}$	Transmission coefficient in TM mode
$T_{\perp}$	Transmission coefficient in TE mode
t_{12}	Transmission coefficient from air to media
t_{21}	Transmission coefficient from media to air
t_{metal}	thickness of metallic layer
t_p	thickness of Parylene
t_{Sub}	thickness of substrate
v_e	Energy velocity

v_p	Phase velocity
w	Ring width
Y'	Admittance per unit length
Z'	Impedance per unit length
Z_L	Impedance for pure left-handed media
α	Blending parameter *or* scale
$\tilde{\beta}$	Complex propagation phase
β	Polarization angle
β_r	Propagation phase
δ	Dialectic loss *or* skin depth
ϵ	Electrical permittivity
ϵ_r	Relative permittivity
ϵ_0	Electrical permittivity of free space
η_0	Characteristic impedance of free space
Θ_i	Incident angle
Θ_r	Refraction *or* reflection angle
θ_t	Transmission angle
κ	Extinction coefficient
λ	Wavelength
μ	Magnetic permeability
μ_0	Magnetic permeability of free space
μ_r	Relative permeability
ν	Frequency
ρ	Electrical resistivity
σ	Electrical conductivity
ϕ	Angle of refraction
ω	Angular frequency
ω_p	Angular plasma frequency
ω_{se}	Angular series frequency
ω_{sh}	Angular shunt frequency

LIST OF ACRONYMS/ABBREVIATIONS

3D	Three Dimensional
Au	Gold
BW	Band width
CCD	Charge coupled device
CMOS	Complementary Metal Oxide Semiconductor
CoNi	Cobalt-Nickel
CRLH TL	Composite right/left-handed transmission line
CSRR	Complementary split ring resonator
Cu	Copper
CVD	Chemical vapor deposition
DFT	Discrete Fourier transformation
DNG	Double negative
DPS	Double positive material
FDTD	Finite difference time domain
FFT	Fast Fourier transform
EM	Electromagnetic
ENG	Epsilon negative
EPD	Electrophoertic deposition
FSS	Frequency selective surfaces
FWHM	Full width half maximum
IR	Infrared
LHM	Left handed material
MEMS	Micro Electro Mechanical Structure
MM	Metamaterial
MNG	Mu negative
NETD	Noise equivalent thermal difference
NIM	Negative index material
PD	Photodetector

PEC	Perfect electric conductance
PMC	Perfect magnetic conductance
PLH	Purely left handed
PS	Polystyrene
Q-factor	Quality factor
RHM	Right handed material
S-parameter	Scattering parameter
Si	Silicon
SEM	Scanning electron microscope
SNG	Single negative
SPP	Surface plasmon polaritons
SRR	Split ring resonator
TDS	Time domain spectroscopy
TE	Transverse electric
TEC	Peltier thermo electric coole
TEM	Transverse electromagnetic
THZ	Terahertz
THz-QCL	THz- Quantum cascade laser
Ti	Titanium
TL	Transmission line
TM	Transverse magnetic

1. INTRODUCTION

1.1. Overview

The Terahertz regime is a region of the electromagnetic spectrum corresponding to about 300 Gigahertz to 3 Terahertz (wavelengths of 1 millimeter to 0.1 mm). This part lies between the microwave and the optical frequencies. The terahertz regime is promising for its unique properties. Same as microwave radiation, THz waves have the ability to penetrate through broad types of non-conducting materials similar to microwave radiation but in shallower depth. but in shallower depth. THz radiation, like X-rays, can penetrate through body tissue. As it is non-ionizing and nondestructive, so it can be a safer replacement for medical X-rays. These unique properties make researchers design THz devices and detectors. For this aim, the THz wave energy is required to be effectively absorbed. Naturally, THz absorbers do not exist, so artificially designed materials with strong absorption peaks, "metamaterials" (MMs), have been introduced around 2000 in the microwave frequency range [1]. Metamaterials become an appealing area because of their material characteristics, which are not found in nature. MMs are composed of sub-wavelength structures of periodic unit cells in various shapes and sizes. Structural size and shape control the electromagnetic response at a specific frequency band. Metamaterials are also promising for enhancing the amount of absorbed energy of electromagnetic waves in various frequency bands: microwave [2, 3], terahertz [4, 5] and infrared [6] frequencies. Different configurations of MM absorbers have been reported as double split ring resonators [7, 8], triple hexagonal shaped resonators [9], metallic leaf-shaped cells [10], cross-shaped [11] and metallic strip [12]. Mostly the absorption bandwidth of absorber based on MMs is limited and narrow. Albeit for ultra-sensing applications, a high Q-factor and strong resonance are crucial, but, in many applications such as terahertz imaging and detection, extending MMs' absorption bandwidth is needed. One of the employed methods is stacking different layers or unit cell structures to combine the resonant bands [13–15]. These types of structures are complicated to design and fabricate. As an alternative, we introduced a broadband absorber by combining different sizes of metallic patches to improve a THz absorber bandwidth by increasing the number of absorption bands, as explained in Chapter 3. In addition to planar designs, in this work, and Chapter 5, we present a 3-dimensional porous structure that is able to achieve broadband absorption.

1.2. THz Radiation, Benefits, Applications

THz radiation does have some uniquely attractive qualities: For example, it is nonionizing, yet images can be produced (deconvolution enhances image resolution [16]). THz radiation's photons are not much energetic to harm atoms and molecules in biological samples, as a study by Frank De Lucia, has shown that a terahertz signal will decrease in power to $2{\times}10^{-7}$ percent of its original strength after traveling just 1 mm in a solution similar to human body tissue [17]. This makes THz devices applicable for surface imaging like skin cancer, check for cracks in tiles on the space shuttle, and early identification of tooth decay (proximal caries) [18]. THz waves can enter through non-conducting materials like clothing and plastics, leading to many important technological applications such as sensing of hidden explosives materials by applying THz time-domain spectroscopy (THz-TDS) in "transmission mode" [19–21], and reflection mode [22]. Security detection of hidden weapons in the form of noninvasive scanning [23, 24] and a 360 ° rotating imaging scheme [25], noninvasive imaging of cancerous cells [26], and biomedical sensing covering "DNA/RNA, amino acids/peptides, proteins, and carbohydrates of cells and tissues", [27, 28] are some other applications of THz waves. Despite these properties, there are technological limitations to realize devices capable of generating radiation at terahertz frequencies and detectors at this band.

1.3. Metamaterial, Design Approaches

In-between two fundamental regimes, namely microwave and infrared regimes, there is a range usually regarded as the "terahertz gap". At gigahertz frequencies, electrons are the fundamental particles, and from infrared to optical wavelengths, the photon is the principal particle inside the natural materials. For the THz gap, numerous efforts have focused on the search for "terahertz materials". However, it is challenging to come across natural elements in this range. Artificial systems, called metamaterials, where unit cells composed of miniature inclusions of shaped conductive metals ($< \lambda/10$) in a homogeneous medium response to EM waves at terahertz frequencies by oscillating electrons inside the "sub-resonators". The physical foundations of the metamaterial media were emerged from linear electromagnetism from the idea of Veselago [29]. In particular, the author theoretically proved that Maxwell's equations do not deny the existence of materials with simultaneously negative ϵ and μ. Metamaterials are multi-layer engineered structures composed of one or more builder bulk materials. They have effective material parameters with negative properties such as "refractive index" [30], "thermal expansion" coefficient [31] or "Hall coefficient" [32] and have properties as perfect lens [33]. These multi-layer structures make it possible to tune ϵ and μ negative simultaneously. While both permittivity and permeability are negative, the refractive index will be negative as well. The metamaterial properties go beyond the natural materials (The prefix meta means beyond which is originated from the ancient Greek word).

The most prevalent approaches to design metamaterials with simultaneous negative ϵ and μ are combinations of thin wires and split ring resonators (SRRs). It has been proposed in [34] at microwave frequencies, and the schematic is represented in Figure 1.1. The unit cell's resonance properties result in anomalous electromagnetic radiation, and thus negative refraction index has been observed in a very narrow frequency range.

In Chapter 2, we will show how such a structure results in simultaneous negative permittivity and permeability. The size and the period of unit cells of most metamaterials are much smaller than the operating wavelength. Therefore, such a structure can be represented as a homogeneous media with effective permittivity and permeability values. Compositions based on metal-dielectric structures are broadly used in MMs' design in different frequency ranges [35], we will study in the next section. An alternative approach to forming metamaterial is transmission line structures [36] that are extensively used in microwave technique as small antennas. In contrast to a wire and SRR structures, transmission lines are non-resonant and mostly planar.

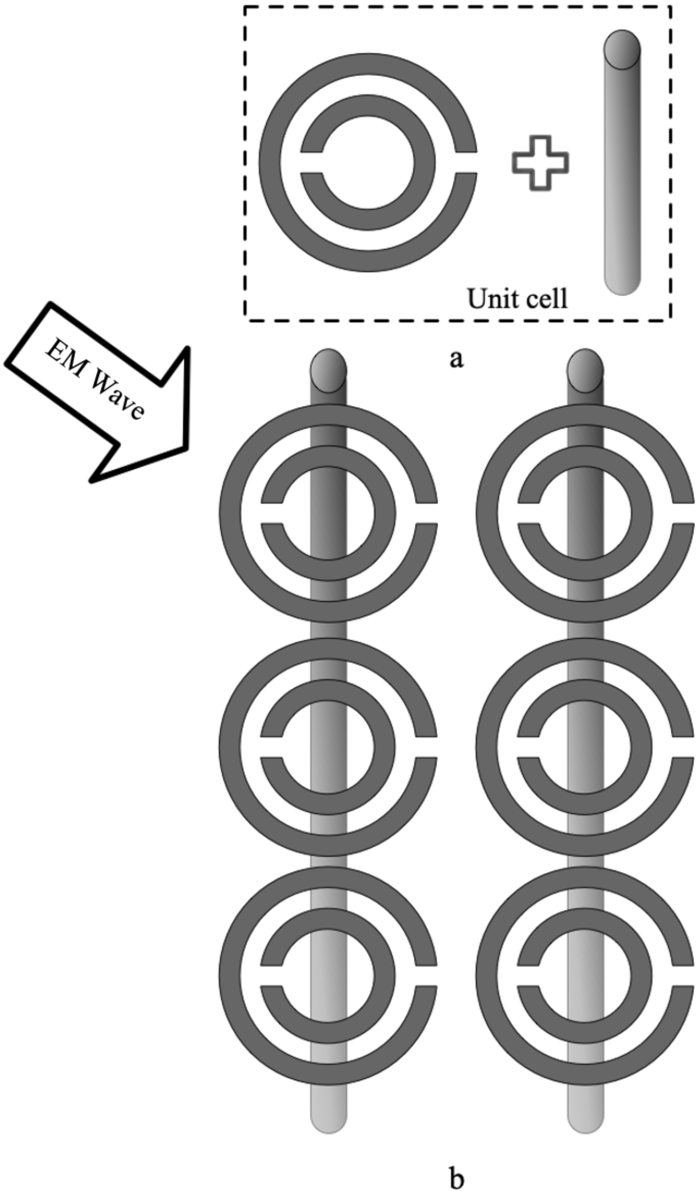

Figure 1.1. (a) The unit cell for SRRs and wire structure, (b) array form of SRRs and wire.

1.4. Metamaterial Absorbers

Metamaterials have become one of the most assuring materials in attempts to obtain perfect absorption. The structure that can absorb the incident EM wave's energy in the corresponding frequency band is named MM absorbers. This special feature makes MM absorber have much inherent applicability in the military field, for example, radar stealth [37], or for civilian such as solar energy harvesting [38] and sensors [39]. To build that kind of compositions; it is essential to lessen reflected/ transmitted power from/ through the device over the working frequency range, thus increasing the absorption. This is linked with the imaginary part of the refraction index, which contributes to losses. As a result, it is desirable to maximize the losses. Performance of MM absorber is governed by geometrical characteristics unlike the traditional material, which often takes effect primarily by the constitutive materials, such as ferrites and iron carbonyl [40]. Besides, their sub-wavelength dimensions offer the design of EM wave absorbers with a thickness much shorter than the wavelength ($< \lambda/10$). The first MM-based perfect absorber was first introduced by Landy et al. in 2008, operating in the microwave frequency band [41]. His design was composited by a metal-dielectric structure as a perfect MM absorber, consisting of electric resonators and magnetic resonators. Their proposed structure obtained almost 1 absorption. Nowadays, MM-based absorbers' performances have been progressed, and their working frequency bands have been extended to microwaves, THz, infrared and visible ranges because of their excellent ability to scale. However, the effective absorption band of these kinds of MM absorbers is narrow. Broadband THz absorbers are crucial components for various purposes like wireless communications, sensing, energy harvesting, and imaging. Recently some MM absorbers have shown fairly considerable absorption bands in the THz band; there is still numerous request for ultra-wideband effective absorbers.

1.5. MM Absorbers In Different Frequency Ranges

In this section, we will review several MM absorber examples in various frequency bands.

1.5.1. MM Absorber In Microwave Frequencies

The earliest material with left-handed properties in the GHz frequency range have been presented and studied in [41]. It is the combination of thin metal wires and split ring resonators (SRRs). The first set artificially makes the effective permittivity negative, while effective permeability is negative because of the second one. The most promising and potentially successful structures for microwave technique are SRRs. Various possible configurations of the unit cell of SRRs are shown in Figure 1.2. The SRRs may be designed in rectangle shapes properly. Microwave SRRs are sufficiently studied at [42]. It examines the dependency of the transmitted power of incident EM wave within single-and double-ring SRRs on the system's parameters such as the dimension and configuration of the SRRs, volume of the unit cell, dielectric characteristics of the medium SRRs embedded, and SRR adjustment relative to the incoming EM radiation.

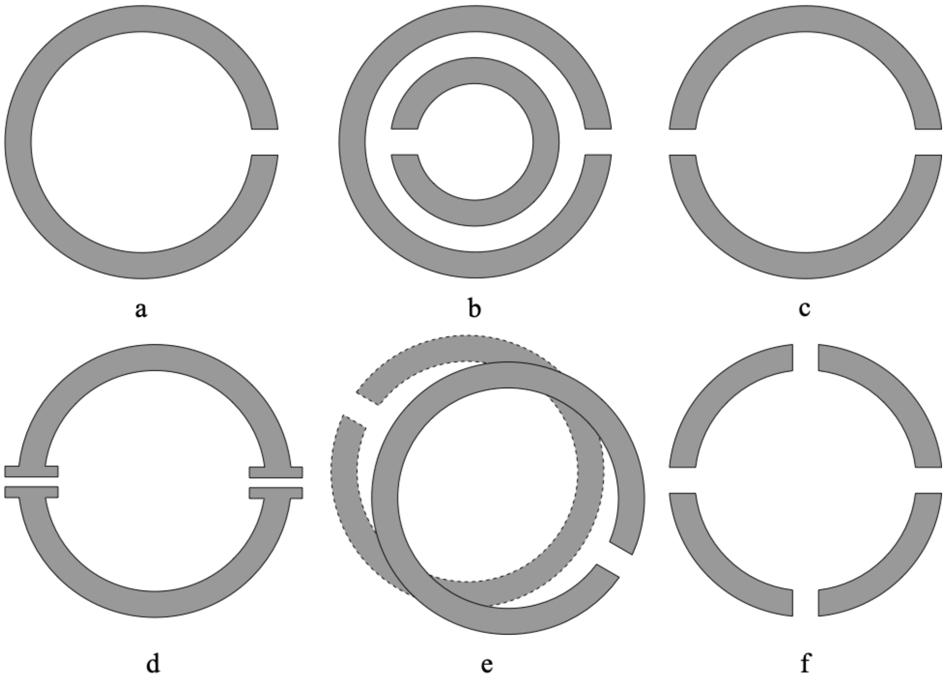

Figure 1.2. Various circular SRR configurations.

In [43] a dual-band switchable metamaterial electromagnetic absorber in GHz frequencies studied with a square split ring in combination with a diode as depicted in Figure 1.3(a,b). "Spiral" and "multiple split-ring resonators" formed by the model of 1.2(b) for the fulfillment of miniaturized magnetic metamaterials in GHz frequencies, have been presented [44].

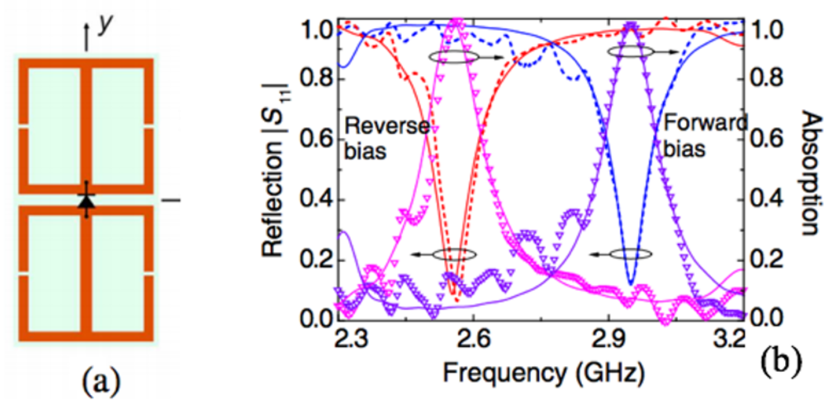

Figure 1.3. (a,b) MM absorber design and its characterization in GHz frequency band [43].

1.5.2. MM Absorber In Infrared Frequencies

Several MM-based infrared absorbers have been demonstrated. The first unit cell design consists of layers in the same plane, each having a cut wire enveloped by two continuous wires, all enclosed in a dielectric medium, as shown in Figure 1.4(a,b). The amount of absorption is 0.9 in the IR region, which is achieved for a single layer numerically [45].

Another unit cell comprises a gold disk or rectangle array separated by a dielectric layer from a gold ground plane. The studies accomplished an absorptivity of 88 % at roughly 1.6 μm wavelength [46] (Figure 1.4(c,d)). Some other designs include complicated isotropic or anisotropic chiral structures of various configurations: G-shaped and U- shaped structures, asymmetric rings, etc. [47–50]. "Chiral plasmonic metasurface" structures are illustrated to operate over the wavelength range from 1.3 μm to 1.8 μm as near infrared absorbers. It is given that an absorptivity of 87 % obtained by chiral structures [51]. The chiral structures are widely used in the technique of infrared wavelengths, as well as optical devices.

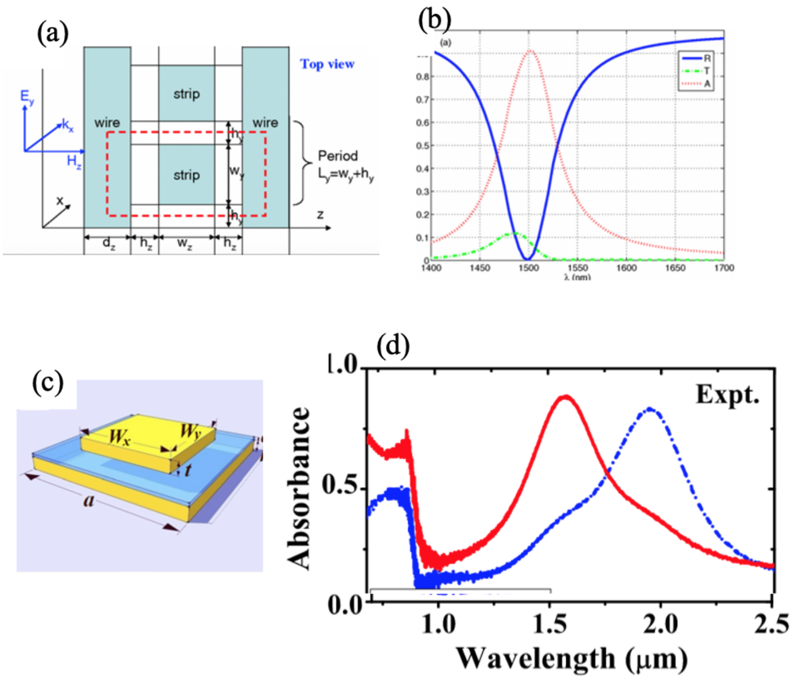

Figure 1.4. MM absorber designs in infrared frequency band, (a,b) [45], (c,d) [46].

1.5.3. MM Absorber In THz Frequencies

Many of the MM designs which can effectively absorb light at a high angle of incidence in the THz frequencies are introduced in a comprehensive review [52]. The first metamaterial-based absorber in THz band presented by Landy et al. [53] demonstrated a simulated absorptivity of $\approx$ 70% at 1.3 THz and BW $\approx$ 200 GHz. An absorber that operates at 1.6 THz with a resonant absorptivity of 97% has been demonstrated at [54] as the first generation of perfect MM absorber is presented in Figure 1.5(a,b). Experimentally verification of THz metamaterial absorbers with a broad and flat absorption band has brought in [55] in a frequency band of 0.9- 1.1 THz. A polarization-insensitive broadband terahertz absorber is presented and demonstrated [56]. Numerically, the polarization-insensitive broadband absorption is more than 0.9, in a frequency band from 4.904 THz to 6.632 THz. (see Figure 1.5(c,d)).

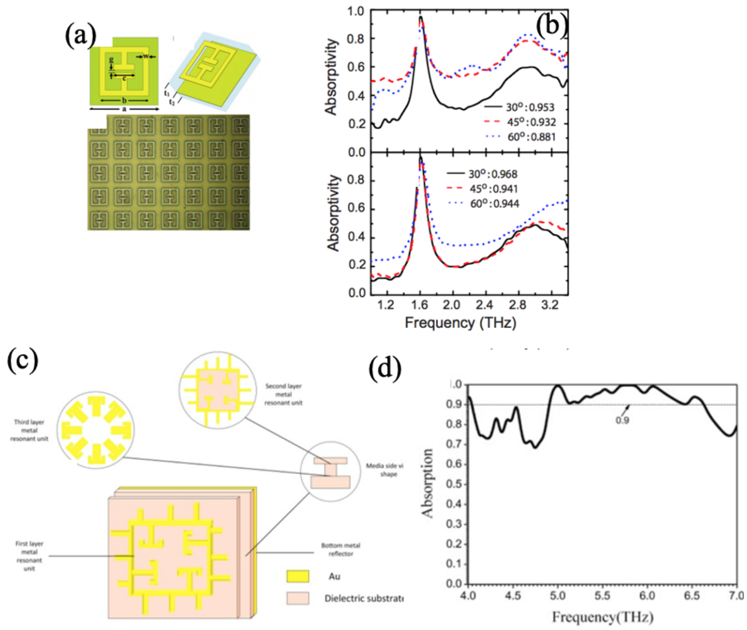

Figure 1.5. MM absorber designs in THz frequency band, (a,b) [54], (c,d) [56].

Recently a single-band conventional metamaterial absorber based on the strontium titanate (STO) enhanced absorption peak to 99.4 % at 5.8 THz [57]. Another work theoretically proposed a triple-band perfect metamaterial absorber based on a split ring resonator with three absorption peaks at frequencies of 3.56 THz, 10.38 THz, and 12.96 THz with absorption efficiency 99.57%, 99.98%, and 99.76%, respectively [58]. However, these metal-dielectric composites suffer from a relatively narrow bandwidth because of their resonating nature, restricting their potential applications. This motivates us to design broadband absorbers. Usually, resonators with different resonant frequencies are utilized to excite various overlying absorption bands to increase the operating bandwidth [59], for example, in [60] by a random distribution of thin ring-shaped metal pieces absorbance performance improved in the microwave regime. One of the most effective ways to broaden absorption band is stacking multilayer metal-dielectric composites [61, 62], as in [63] assorted dimensions of metallic strips, which are stacked on polyimide layers with equal spacing, improve the amount of absorptivity to 0.95 in a band of 0.81-1.32 THz. This perfect wideband absorption is achieved by losing the absorber's thinness, being lightweight, and increasing fabrication and design complexities. Recently a broadband THz absorber is designed by vanadium dioxide square loop. The absorption is increased to 96% in the frequency range from 3 THz to 7 THz by increasing the conductivity of vanadium dioxide, which is dependent on material properties [64]. In this study, numerical results showed that the bandwidth of absorption rate above 90% is 1.25 THz. For broadband operation, some complicated unit cell shapes composed of two 90 degree crossed dumbbell-shaped doped-silicon grating arrays [65] which absorbing more than 95% ranging from 0.92 THz to 2.4 THz., supercells of fractal crosses absorbers [66], experimentally verified average absorption is 83% from 2.82 THz to 5.15 THz, are introduced in THz frequencies, limiting the ease of modeling and fabrication.

2. Wave propagation, in Different Media, RHM and LHM

2.1. Electromagnetic Radiation

Electromagnetic radiation consists of sinusoidally varying electric field (E) and magnetic field component (H), perpendicular to each other and orthogonal to the direction of propagation of the EM wave. These electric and magnetic fields progressing within space at the speed of light ($2.998\times10^8 m/s$). It does not comprise mass or charge and travels in discrete packages of energy called "photons". As photon packets travel, the electric and magnetic fields turn direction. The number of turns, or oscillations, that happen in one second is the frequency, f. The frequency unit is oscillations per second, or simply s^{-1} (Hertz). The distance over which the electric and magnetic components of EM wave travel make one complete oscillation called the wavelength, or wavelength of the radiation, λ. Wavelength is the distance between maxima of either electrical or magnetic component, i.e., from crest to crest. The wave characteristics of EM radiation are found in the relationship of velocity to wavelength and frequency, stated in the formula as;

$$c = \lambda\nu, \tag{2.1}$$

where c is velocity, λ is wavelength, and ν is frequency. When radiation passes through a medium comprising particles (atoms, electrons, a material unit cell), its propagation is slowed down (velocity) due to its interaction with bounded electrons in the particles. Since the frequency is invariant by passing from one medium to another and determined by the source, the wavelength must decrease. The range of all probable frequencies of electromagnetic waves is named EM spectrum. The lowest frequencies are at one end of the spectrum, while the waves with higher frequencies are at the other end. The spectrum is divided into regions with different wave types. At the lowest frequencies, we have radio waves ($\lambda \approx 1mm$). Then, as we raise frequency, we discover microwaves, infrared radiation, and visible light waves. Shifting to higher frequencies, we have ultraviolet radiation, X-rays, and gamma rays. Gamma rays have the highest frequencies of all the EM waves ($\lambda \approx$ 10-9nm). The electromagnetic nature of photons all over the EM spectrum is the same, but their energy levels differ and are directly proportional to their frequency ($E = h\nu = hc/\lambda$) and measured in eV. In confronting with various materials, their interaction is altering because of the energy level. The different behavior of EM waves inside materials can determine various applications. For example, Radio waves have the lowest energy and frequency and the longest wavelength used in communications. Gamma rays are capable of penetrating large body parts [67], have the highest energy and frequency, and the shortest wavelength. The summary is collected in Table 2.1.

Table 2.1. Electromagnetic Radiation Summarized by Frequency Bands and Applications.

Radiation	**Frequency**	**Wavelength**	**Application**
Gamma Rays	10^{24} - 10^{20}	$< 1pm$	Treat tumours, Sterilizing
X-Rays	10^{17} - 10^{20}	$1nm$ - $1pm$	Human body and objects Imaging
Ultraviolet	10^{15} - 10^{17}	400nm - 1nm	Fluorescent Tubes, Security Marking
Visible Light	4 - 7.5×10^{14}	750nm - 400nm	Fiber-optic communication
Near Infrared	10^{14} - 4×10^{14}	2.5μm - 750 nm	Feed ingredients recognition
Infrared	10^{13} - 10^{14}	25 μm - 2.5 μm	Thermal Imaging, Remote Control
Microwaves	3×10^{11} - 10^{13}	1 mm - 25 μm	Treat tumours, Sterilizing
Radio Waves	$< 3 \times 10^{11}$	$> 1mm$	Communications, Broadcasting, Radar

An Electromagnetic wave to be generated needs stimulated electric charges which radiate energy. A common way of producing electromagnetic waves is to applying a sinusoidal voltage source to an antenna, which causes each end of the antenna bars to charged to opposite charges. As the charges continue to oscillate between the bars, electric fields are produced and moved away with light speed. The charges' motion also produces a current, which sets up a magnetic field enclosing the bars. Figure 2.1 represents the electric and the magnetic field lines produced by an electric-dipole antenna.

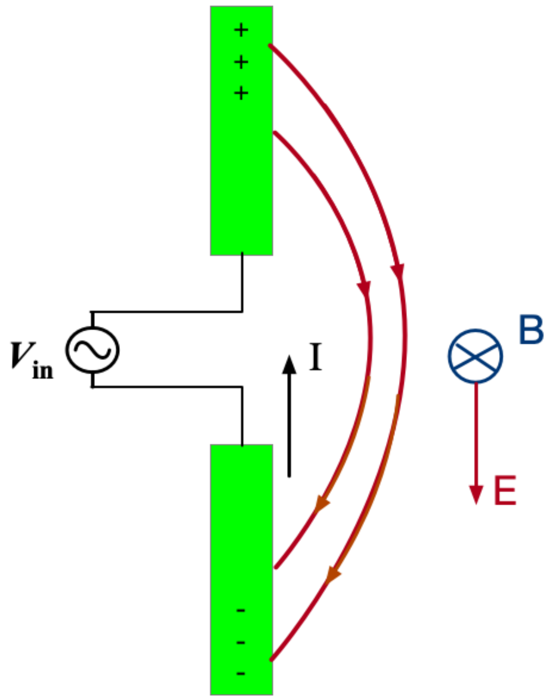

Figure 2.1. Electric and magnetic field formations at the moment the current is upward.

The continuous induction of a magnetic field because of the presence of a time-varying electric field and vice versa creates EM radiation. In section 2.3, we will see the relationship between electric field and magnetic field.

2.2. Interaction of Radiation

When an electromagnetic wave strikes a medium, some portion of it transmits through the medium (T), some part reflects from the medium (R), or absorption of EM wave (A) may occur. Refraction, polarization, diffraction, or scattering are the special forms of T, R, and A, which may happen depending on the medium's composition and the EM wave's wavelength. Reflection occurs when the incident wave encounters an object and skips off. Very smooth surfaces such as mirrors and metal surfaces at THz frequencies reflect almost all incident beams. Lasers use the reflective behavior of EM waves to map the elevation of surfaces [68]. Absorption happens when photons from the incident wave impinge atoms and molecules and make them vibrate. As the media's molecules move, this vibration converts to heat. Thermal energy is the heat that is emitted from the media. The wavelength of this radiated thermal energy is longer and corresponds to the infrared region, which is suitable to apply in thermal imaging [69]. When an EM wave (light) passes around the edge of an object or a slit, "diffraction" happens, which is the slight bending and spreading of the wave. The amount of bending depends on the wavelength and the size of the opening. It happens when an electromagnetic wave hits an object with a dimension comparable to the wavelength of the striking beam. Diffraction and interference of light from slits or gratings are used in spectrometers to separate wavelengths, and identifying materials [70]. The traveling of an electromagnetic wave in different media causes the change in the beam's speed, bending the incident wave. This is called "refraction". Different wavelengths of EM waves are slowed at different rates, which causes them to bend at different angles. Colors of rainbow composed while visible light passes within the glass prism. Transmission of waves occurs when waves passing through a given point or medium without changing the direction. Transmission of a wave is a special form of refraction. Scattering occurs when waves diverge from the expected path and spread out in various directions. It varies based on the wavelength of the incident wave and the size of the medium. Small particles (molecules) in the atmosphere scatter out the short (blue) wavelengths in all directions much more than long wavelengths, so that, scattering of light makes the sky appear to be blue (Rayleigh scattering) [71]. The EM wave emitted from a source is generally unpolarized, which means light has oscillations at random directions, perpendicular to the direction of propagation. Unpolarized light converted into polarized light by Polarizing filters. A polarizing filter blocks or transforms randomly oriented vibrations into either a linear, circular or elliptical electromagnetic wave so that the EM wave is said to be polarized. The light reflects from a nonmetallic flat surface, like a window, or the surface of a lake can become polarized. When the light hits a horizontal surface, it reflects the horizontal waves more than the rest of the waves, causing a glare. Vertically polarized filters block the horizontally polarized light at polarized sunglasses [72].

2.3. The Modern Electromagnetic Wave Theory and Derivation of Electromagnetic Waves from Maxwell's Equations

Four equations made the electromagnetic wave theory's fundamentals which are known as Maxwell's equations. They express the primary ideas of the interaction rules between material and electromagnetic energy, from the remarkably long wavelengths of radio, television, radar, and microwaves, to the shorter wavelengths of visible light and ultraviolet light in various scientific regulations. Maxwell's equations identify the origins of electric and magnetic fields and their relationships to each other. For reference, Maxwell's equations are listed below;

$$\nabla \cdot \tilde{\mathbf{D}} = \rho, \tag{2.2}$$

$$\nabla \cdot \tilde{\mathbf{B}} = 0, \tag{2.3}$$

$$\nabla \times \tilde{\mathbf{E}} = -\frac{\partial \tilde{\mathbf{B}}}{\partial t}, \tag{2.4}$$

$$\nabla \times \tilde{\mathbf{H}} = \frac{\partial \tilde{\mathbf{D}}}{\partial t} + \tilde{\mathbf{J}}. \tag{2.5}$$

The electromagnetic properties of most media can be characterized by the constitutive relations,

$$\tilde{\mathbf{D}} = \epsilon \tilde{\mathbf{E}}, \tag{2.6}$$

$$\tilde{\mathbf{B}} = \mu \tilde{\mathbf{H}}, \tag{2.7}$$

$$\tilde{\mathbf{J}} = \sigma\tilde{\mathbf{E}}. \tag{2.8}$$

This is the feature of Maxwell's equations, which describes electromagnetic waves and their simple characterization of materials in terms of conductivity, σ ($\frac{S}{m}$), permittivity, ϵ ($\frac{F}{m}$), and permeability, μ ($\frac{H}{m}$). However, by considering Maxwell's first-order differential equations in the frequency domain and re-writing them;

$$\nabla \times \tilde{\mathbf{E}} = -j\omega\mu\tilde{\mathbf{H}}, \tag{2.9}$$

$$\nabla \times \tilde{\mathbf{H}} = j\omega\epsilon\tilde{\mathbf{E}}. \tag{2.10}$$

Assuming an isotropic media with no surface charge or current source and by taking the curl of Faraday's law (Eq. 2.4),

$$\nabla \times (\nabla \times \tilde{\mathbf{A}}) = \nabla(\nabla \bullet \tilde{\mathbf{A}}) - \nabla^2\tilde{\mathbf{A}}, \tag{2.11}$$

and Gauss's law, replacing $\tilde{\mathbf{B}}$ with $\mu\tilde{\mathbf{H}}$, and using Ampere's law (Eq. 2.5) to replace $\nabla \times \tilde{\mathbf{H}}$ Helmholtz wave equation becomes as below;

$$\nabla^2\tilde{\mathbf{E}} - \epsilon\mu\frac{\partial^2\tilde{\mathbf{E}}}{\partial t^2} = 0, \tag{2.12}$$

where $\epsilon\mu = \frac{1}{\mathrm{c}^2}$, and c $= \frac{c_0}{n}$, having c_0 as the speed of light in vacuum and c is the speed of light inside the material with a refractive index of n. These quantities are expressed as

$$c_0 = \frac{1}{\sqrt{\epsilon_0\mu_0}}, \tag{2.13}$$

$$n = \frac{c_0}{c} = \sqrt{\epsilon_r\mu_r}, \tag{2.14}$$

where ϵ_r and μ_r is relative permittivity and relative permeability of the media EM wave interacts. $\tilde{\mathbf{E}}$ field represented by sinusoidal wave as a function of space $\tilde{\mathbf{r}}$ and time t as $\tilde{\mathbf{E}}(\tilde{\mathbf{r}}, t) = E_0 \cos(\omega t - k{\cdot}r)$. Substituting this $\tilde{\mathbf{E}}$ field into the wave equation, we find the dispersion relation between the frequency and the wavevector $\tilde{\mathbf{k}}$ for the EM waves,

$$\omega = c|\tilde{\mathbf{k}}|, \tag{2.15}$$

$$|\tilde{\mathbf{k}}| = \frac{2\pi}{\lambda} = \frac{n}{c_0}\omega. \tag{2.16}$$

The angular frequency, ω, is simply related to frequency, f, as $\omega = 2\pi f(rad/s)$. k is called as wavenumber (rad/m) and is the magnitude of the wavevector. It depends on λ, stating that by changing the material, wavelength differs so that the $\tilde{\mathbf{k}}$.

Consider an arbitrary uniform plane wave which is propagating in z-direction and linearly polarized in x-direction is represented as $\tilde{\mathbf{E}}(z, t) = \tilde{\mathbf{x}} E_x \cos(\omega \mathrm{t}$ - k$\cdot z)$. We can find $\tilde{\mathbf{H}}(z, t)$ using Faraday's law (Eq. 2.4),

$$\frac{\partial \tilde{\mathbf{H}}}{\partial \mathrm{t}} = -\frac{(\nabla \times \tilde{\mathbf{E}})}{\mu_{\mathrm{o}}}. \tag{2.17}$$

We can evaluate the curl of $\tilde{\mathbf{E}}$ as

$$\nabla \times \tilde{\mathbf{E}} = \tilde{\mathbf{x}}\left(\frac{\partial \mathrm{E_z}}{\partial \mathrm{y}} - \frac{\partial \mathrm{E_y}}{\partial \mathrm{z}}\right) + \tilde{\mathbf{y}}\left(\frac{\partial \mathrm{E_x}}{\partial \mathrm{z}} - \frac{\partial \mathrm{E_z}}{\partial \mathrm{x}}\right) + \tilde{\mathbf{z}}\left(\frac{\partial \mathrm{E_y}}{\partial \mathrm{x}} - \frac{\partial \mathrm{E_x}}{\partial \mathrm{y}}\right) = -\tilde{\mathbf{y}}\frac{\partial \mathrm{E_x}}{\partial \mathrm{z}}. \tag{2.18}$$

Then, by integrating over time, it becomes;

$$\tilde{\mathbf{H}}(\mathrm{z}, \mathrm{t}) = \sqrt{\frac{\epsilon_{\mathrm{o}}}{\mu_{\mathrm{o}}}}\tilde{\mathbf{E}}(\mathrm{z}, \mathrm{t})\tilde{\mathbf{y}}, \tag{2.19}$$

$$\tilde{\mathbf{H}}(\mathrm{z}, \mathrm{t}) = \tilde{\mathbf{y}}\frac{\tilde{\mathbf{E}}(\mathrm{z}, \mathrm{t})}{\eta_{\mathrm{o}}}. \tag{2.20}$$

The equations above state that EM fields are transverse, i.e., in a medium that is homogeneous $\tilde{\mathbf{E}}$ and $\tilde{\mathbf{H}}$ are completely correlated [73]. The magnitude of the electric field is $\eta_{\mathbf{0}} = \sqrt{\frac{\mu_0}{\epsilon_0}}$ times that of the magnetic field; This is a characteristic of transverse electromagnetic (TEM) waves. In free space, η_0 is known as the characteristic impedance of free space and approximately equals 377 ohms. Figure 2.2 illustrates how these electric and magnetic fields are in phase but orthogonal to each other and propagation's direction.

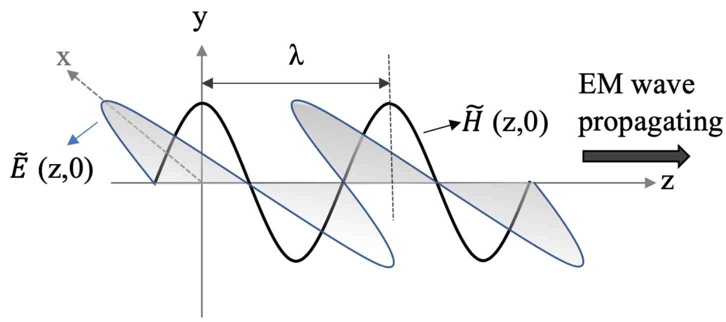

Figure 2.2. +z propagating y-polarized uniform plane wave of a magnetic field with a wavelength λ.

2.4. Wave Propagation in Left-Handed Media

Consider the Maxwell's equations (Eq.2.9, Eq.2.10) and plane wave form of $\tilde{\mathbf{E}}(\tilde{\mathbf{r}}, t) = E_0 \cos(\omega t - k{\cdot}r)$ and having the dispersion function (Eq.2.16) and knowing that n is $\sqrt{\epsilon_r \mu_r}$, then

$$|\tilde{\mathbf{k}}| = \sqrt{|\epsilon||\mu|}\omega. \tag{2.21}$$

It comes from the equation above that the sign of $|\tilde{\mathbf{k}}|$ will remain unchanged when ϵ and μ are both positive. A negative value of only ϵ or μ makes the propagation vector imaginary; thus, the incident EM wave will be decaying instead of propagating. It is also obtained a positive value after a simultaneous change of the signs of permittivity and permeability. Let us rewrite Maxwell's curl equations for plane wave solutions and time-harmonic notations, this time considering the sign change of ϵ and μ,

$$\tilde{\mathbf{k}} \times \tilde{\mathbf{E}}(\tilde{r}) = \omega\mu\tilde{\mathbf{H}}(\tilde{r}), \tag{2.22}$$

$$\tilde{\mathbf{k}} \times \tilde{\mathbf{H}}(\tilde{r}) = -\omega\epsilon\tilde{\mathbf{E}}(\tilde{r}). \tag{2.23}$$

Therefore, for positive ϵ and μ , $\tilde{\mathbf{E}}$, $\tilde{\mathbf{H}}$, and $\tilde{\mathbf{k}}$ form a right-handed orthogonal system of vectors. If $\epsilon < 0$ and $\mu < 0$ simultaneously then $\tilde{\mathbf{E}}$, $\tilde{\mathbf{H}}$, and $\tilde{\mathbf{k}}$ develop a left-handed triplet, as depicted in Fig.2.3. This is the main idea of naming a simultaneous negative ϵ and μ media as "left-handed" media [74].

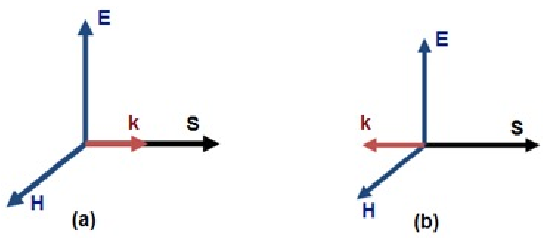

Figure 2.3. Illustration of the system of vectors E, H, k, and S for a plane transverse electromagnetic (TEM) wave in (a) an ordinary right-handed and (b) a left-handed medium.

The signs of real parts of the effective complex constitutive parameters indicates their signs, whereas their imaginary parts represent electric or magnetic losses, respectively. Energy conversion equation obtains the energy flow known as the Poynting vector [75] as

$$\tilde{\mathbf{S}} = \tilde{\mathbf{E}} \times \tilde{\mathbf{H}}. \tag{2.24}$$

Poynting vector provides information about the EM field's propagation direction and information about energy transport direction in the EM field. It is unaffected by a synchronous change of sign of ϵ and μ. Thus, $\tilde{\mathbf{E}}$, $\tilde{\mathbf{H}}$, and $\tilde{\mathbf{S}}$ still set a right-handed triplet in a left-handed medium. Accordingly, in such media, energy and wavefronts propagate in opposite directions (”backward propagation”), a unique characteristic of left-handed materials. Their capacity to support backward waves, which are waves whose power propagates in the opposite direction of their energy, appeals most of the surprising, extraordinary electromagnetic characteristics of these media such as inverse Doppler effect [76] and Negative Goos- Hanchen shift [77].

2.4.1. Refractive Index

According to Snell's law, when an EM wave travels from one medium to another, it generally bends or refracts. This law gives us a way of predicting the amount of bend dependent on the refractive indices of two media. The refractive index, $\tilde{\mathbf{n}}$ of a material is a dimensionless quantity that reflects the speed of EM wave within the material. It also characterizes how the waves are directed at the boundaries of two materials with different refractive indices. When the EM wave travels in an interface of a slab from media 1 to media 2, the wavevector's tangential components continued along with the interface based on boundary conditions. The relation between refraction indices of two media and angles brought by Snell's law,

$$\frac{\sin\theta_{\mathrm{i}}}{\sin\theta_{\mathrm{r}}} = \frac{|k_2|}{|k_1|} \equiv \frac{n_2}{n_1}. \tag{2.25}$$

The refraction phenomena in the interfaces of two different materials described as shown in Figure 2.4, medium 2 is an LHM and n_2 is the refractive index, and medium 1 is an ordinary one with the refractive index of n_1. θ_i is the incident angle, and θ_r is the refraction angle in medium 2. As we discussed in Section 2.4, in a medium with simultaneously negative permittivity and permeability, rays still propagate parallel to the energy flow, though the wavevector is in the opposite direction. Accordingly, the incident beam is deflected to the opposite side of the surface normal when the index is positive; in contrast, the exiting ray diverges to the same side of the normal for a negative index [78]. The Eq. 2.14 for a left-handed material can be written as

$$n = -\sqrt{\epsilon_r \mu_r}. \tag{2.26}$$

simultaneous change of sign in ϵ and μ, does not influence the sign of n^2; consequently, the low-loss left-handed media is expected to pass the EM radiation (transparent), and EM wave can propagate through LHM. A positive amount of n makes the vectors of phase velocity v_p (wavevector) and energy velocity v_e or Poynting vector, $\tilde{\mathbf{S}}$, parallel. If the refractive index is negative, they point in opposite directions as shown in Figure 2.4.

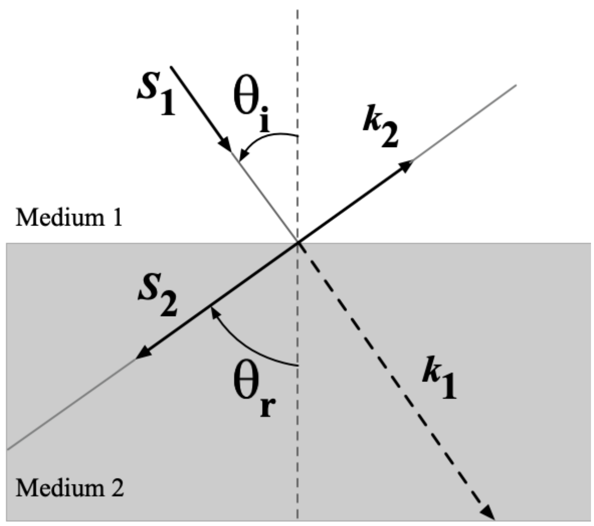

Figure 2.4. Refraction of EM wave travelling from an ordinary medium (1) to a left-handed medium (2).

2.4.2. Transmission, Reflection and Absorption Coefficients

In this section, a general formulation with a complete solution for electromagnetic waves interacting with a slab of a negative isotropic medium is provided. After showing that the characteristic waves in negative isotropic media are backward waves, the incident wave's reflection and transmission coefficient to a slab is calculated. The medium is assumed to be lossless, isotropic, and homogeneous with electrical and magnetic parameters ϵ and μ. It is well known that reflection happens when an EM wave strikes a boundary between two optical media with different refractive indexes. Figure 2.5 shows a plane wave entering the boundary connecting two homogeneous media. Based on Maxwell equations the boundary conditions at the interface among two media, can be obtained as

$$D_{1n} = D_{2n}, \quad B_{1n} = B_{2n}, \quad E_{1t} = E_{2t}, \quad H_{1t} = H_{2t}, \tag{2.27}$$

where the indexes n and t imply normal and tangential, respectively. The first two equations declare that if the charges are absent at the interface, the normal components of D and B will be continuous. In contrast, the last two questions declare that in the nonexistence of sources at the interface, the tangential components of E and H are continuous. By considering that the LH medium (medium 2) is weakly dispersive with ϵ_2 and μ_2, we obtain the following boundary conditions at an RH/LH interface,

$$E_{1n} = -\frac{\epsilon_2}{|\epsilon_1|}E_{2n}, \quad H_{1n} = -\frac{\mu_2}{|\mu_1|}H_{2n}, \quad E_{1t} = E_{2t}, \quad H_{1t} = H_{2t}. \tag{2.28}$$

At the boundary between an RH medium and an LH medium, the tangential elements of $\tilde{\mathbf{E}}/\tilde{\mathbf{H}}$ stay continuous while their normal components regenerate as antiparallel.

In general, from the incident wave, $e^{j\tilde{\mathbf{k}}_{\mathbf{i}}\tilde{r}}$, in medium 1, a reflected wave, $e^{j\tilde{\mathbf{k}}_{\mathbf{r}}\tilde{r}}$, and a transmitted wave in medium 2, $e^{j\tilde{\mathbf{k}}_{\mathbf{t}}\tilde{r}}$ are generated. It can be shown that the tangential component of the wavenumber is continuous at the junction between two media $\tilde{\mathbf{k}}_{1,tan} = \tilde{\mathbf{k}}_{2,tan}$ [79]. This condition proves that incident, transmitted, and reflected wave vectors need to be in the incidence plane. The proportion of the amplitude of the reflected wave to the wave incident at the junction is the reflection coefficient. It determines how an impedance discontinuity reflects a portion of an electromagnetic wave in the transmission medium. The transmission coefficient is the fraction of EM incident

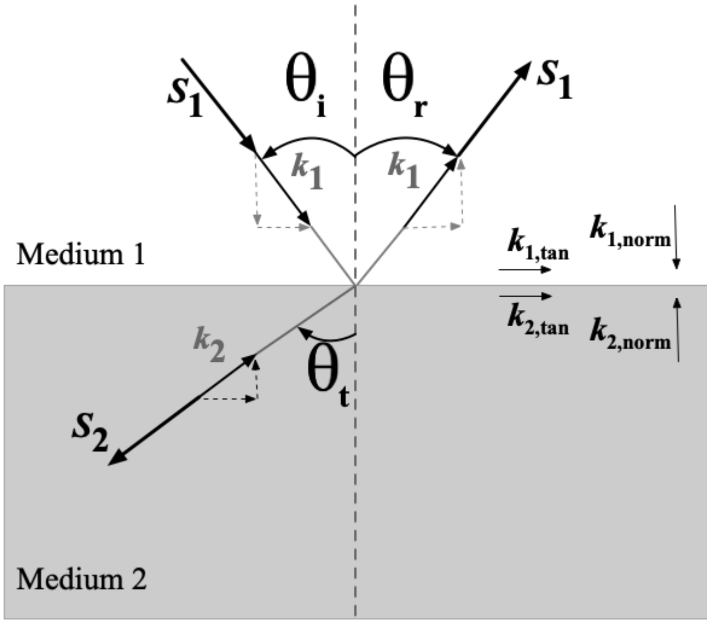

Figure 2.5. Illustration of the incoming, reflected, and transmitted waves at an RH(medium 1)/LH (medium 2) interface.

wave transmitted through a media. It is a ratio of the amplitude of the transmitted wave to the wave incident at the interface. Transmission and reflection coefficients at an jointing between two media, which one of them is LH medium for TM (parallel polarization) and TE (perpendicular polarization) modes, are given with Fresnel coefficients by [80, 81], as

$$R_{\parallel} = \frac{-\epsilon_{r1}|k_{2z}| - (-|\epsilon_{r2}|)k_{1z}}{-\epsilon_{r1}|k_{2z}| + (-\epsilon_{r2})k_{1z}} = \frac{\eta_2 \cos\theta_2 - \eta_1 \cos\theta_1}{\eta_2 \cos\theta_2 + \eta_1 \cos\theta_1}, \tag{2.29}$$

$$T_{\parallel} = \frac{2\left(-\epsilon_{r1}|\epsilon_{r2}|(-|\mu_{r2}|)/\mu_{r1}\right)k_{1z}}{\epsilon_{r1}(-|k_{2z}) + (-|\epsilon_{r2}|)k_{1z}} = -\frac{2\eta_2 \cos\theta_1}{\eta_2 \cos\theta_2 + \eta_1 \cos\theta_1}, \tag{2.30}$$

$$R_{\perp} = \frac{-|\mu_{r2}|k_{1z} - \mu_{r1}(-|k_{2z}|)}{-|\mu_{r2}|k_{1z} + \mu_{r1}(-|k_{2z}|)} = \frac{\eta_2 \cos\theta_1 - \eta_1 \cos\theta_2}{\eta_2 \cos\theta_1 + \eta_1 \cos\theta_2}, \tag{2.31}$$

$$T_{\perp} = \frac{2(-|\mu_{r2}|)k_{1z}}{-|\mu_{r2}|k_{1z} + \mu_{r1}(-|k_{2z}|)} = \frac{2\eta_2 \cos\theta_1}{\eta_2 \cos\theta_1 + \eta_1 \cos\theta_2}. \tag{2.32}$$

η_1 and η_2 are the intrinsic impedance of medium 1 and 2. In comparison with the inteface between two right handed media we changed the sign of constitutive parameters and wave vector of media number 2 as : $\epsilon_{r2} = -|\epsilon_{r2}|$, $\mu_{r2} = -|\mu_{r2}|$ and $k_{2z} = -|k_{2z}|$, because of the fact that this medium is LH. As comes from the Eq. 2.29 - Eq. 2.32 the reflection and transmission coefficients of a incident beam to interfaces of RH/RH and RH/LH media are the same except the phase of transmission in TM mode which is reversed in a RH/LH interface. The reflected wave will be generated only if the medium impedance changes, i.e., if η_1 is not different from η_2, and is the same with intrinsic impedance, perfect transmission without reflection will obtain.

2.4.3. Losses

In this section, we introduce losses in a medium. For this, let us rewrite the permittivity and permeability of the material considered,

$$\epsilon_r = \epsilon' - j\epsilon'' = \epsilon'\left(1 - j\tan\delta_e\right), \quad \tan\delta_e = \frac{\omega\epsilon'' + \sigma_e}{\omega\epsilon'}, \tag{2.33}$$

$$\mu_r = \mu' - j\mu'' = \mu'\left(1 - j\tan\delta_m\right), \quad \tan\delta_m = \frac{\omega\mu'' + \sigma_m}{\omega\mu'}. \tag{2.34}$$

As comes from Equation. 2.33 and Equation. 2.34 the imaginary parts of ϵ_r and μ_r indicate losses. $\omega\epsilon''$ express loss due to dielectric damping, σ_e loss because of finite electric conductivity, $\omega\mu''$ loss from magnetic damping, and σ_m loss coming from finite (fictitious) magnetic conductivity. The refractive index of such a medium is generally a complex number depending on wavelength,

$$\tilde{\mathbf{n}}(\lambda) = n(\lambda) + i\kappa(\lambda). \tag{2.35}$$

Equations Eq.2.29 - Eq.2.32 which have been derived in section 2.4.2, represent only wave reflection from a medium and wave transmission through it. Concurrently, while EM waves propagating a conducting material, it induces a current in it. This induced current generates heat due to the transformation of a portion of the incident radiation's energy. Usually, such loss is defined by the absorption coefficient [82]. Therefore, for compatibility, we consider that the absorption coefficient is the quantity in Eq.2.36. This declaration obeys the law of "energy conservation". Clearly, such a description is general and independent of direct or averaging calculation process,

$$R + T + A = 1. \tag{2.36}$$

In a medium, some portion of radiated power upon a surface is transmitted (T) through it, or reflected (R) from the surface or absorbed by it (A).

Without considering the material's refractive index, the reflected power from the interface of two materials can be discarded by impedance matching. One can get the advantages of losses as a part of complex negative refraction in perfect absorbers with zero R and T, which turns A = 1.

2.5. Transmission Line Approach in LHM

When a structure's fundamental average cell size is much shorter than the wavelength of incident EM beam, λ_g, it is called an effectively homogeneous structure. Because LHMs are effectively homogeneous structures, they can be fundamentally formed as "transmission lines" (TLs). To obtain a negative index of refraction, such TLs are typically loaded with a network of series capacitors and shunt inductors. In the presence of a left-handed capacitance and inductance, a real LH structure necessarily includes C_R and L_R. This concept as a composition of right and left-handed TLs (CRLH), introduced by Caloz et al. in [83]. Purely LH (PLH) structure does not exist. Magnetic fluxes are induced because currents flow along C_L. Consequently, a series inductance L_R is additionally existing; besides, voltage gradients present due to currents flowing across L_L, which corresponds to a shunt capacitance C_R. The right-handed network contributes as parasitic series inductance and shunt capacitance; as frequency rises, the right-handed network will be the dominant one. A plane transverse electromagnetic(TEM) wave is a wave for which the electric and magnetic field vectors lie in a transverse plane or perpendicular to the propagation axis. This is the basic kind of wave that presents on an ideal transmission line. The equivalent circuit model for such a lossless CRLH TL is shown in Figure 2.6.

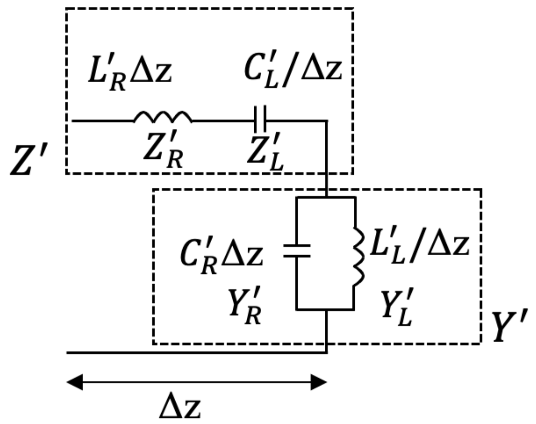

Figure 2.6. Ideal CRLH transmission line equivalent circuit model.

In this figure $Z'(\Omega/m)$ is per-unit length impedance, $L_R(H/m)$ is a RH per-unit-length inductance in series with a LH times-unit-length capacitance $C_L(F.m)$. $Y'(S/m)$ is a per-unit- length admittance, $C_R(F/m)$ is a RH per-unit-length capacitance in parallel with a LH times-unit-length inductance $L_L(H.m)$. At low frequencies $\omega \to 0$, $Z'_R \to 0$, $Y'_R \to 0$, so that the CRLH transmission line becomes equivalent to a pure LH TL ($L'_R = C'_R = 0$). At high frequencies $\omega \to \infty$, $Z'_L \to 0$, $Y'_L \to 0$, so that the CRLH TL becomes equivalent to a pure RH TL ($L'_L = C'_L = 0$). Analysis of the TL network has been done based on generalized telegraphist's equations. The characteristic impedance $Z_c(\Omega)$, describing the voltage and current on the line obtained,

$$Z_c = Z_L\sqrt{\frac{(\omega/\omega_{se})^2 - 1}{(\omega/\omega_{sh})^2 - 1}}, \tag{2.37}$$

where Z_L is the pure LH impedance, $Z_L = \sqrt{\frac{L'_L}{C'_L}}$ and the series and shunt resonance frequencies (rad/s) are as;

$$\omega_{se} = \frac{1}{\sqrt{L'_R C'_L}}, \tag{2.38}$$

$$\omega_{sh} = \frac{1}{\sqrt{L'_L C'_R}}. \tag{2.39}$$

Transmission line theory can analyze the propagation characteristics of the structures shown in Figure 2.6. The voltage and current of the transmission line and its components agree with the electromagnetic field components. For isotropic homogeneous medium, the impedance and admittance can be written as $Z = j\omega L$, $Y = j\omega C$ whereas those variables for left-handed transmission line are defined as $Z' = \frac{1}{j\omega C}$, $Y' = \frac{1}{j\omega L}$.

Although forming left-handed media as transmission line structures is convenient [84], another approach is to describe unit cells, and total systems based on equivalent circuits [85]. We will describe our proposed designs based on lumped circuit elements in the next chapters.

2.6. Left- Handed Media

Nearly all isotropic natural materials have positive values of permittivity and permeability more than unity. They thus are determined as DPS (double positive) materials. Materials with negative ϵ or μ only are termed as SNG (single negative) materials depending on negative effective parameters classified as ENG (epsilon-negative) and MNG (mu-negative). Being negative value of each, the refractive index of the incident beam becomes imaginary and damped (evanescent). Thus electromagnetic waves can still propagate in such material and decay. Consider that the material is opaque to radiation if its thickness is greater than the characteristic attenuation length of the electromagnetic wave. We need to introduce ENG and MNG media first to construct artificial material with left-handiness properties and simultaneously negative permittivity and permeability values. The double negative structure (DNG) realizes with a combination of ENG and MNG media. Either the Drude or Lorentz model defines permittivity and permeability. They are evaluating the optical properties.

2.6.1. Epsilon Negative Media

The most known natural ENG-material in which the dielectric constant is negative in a specific frequency range is the plasma. Regular ϵ-negative materials are metals. The Drude model explains metals' dielectric constant as a frequency function. The permittivity of metal is negative at frequencies under plasma frequency [86]. For instance, the metals behave as ENG materials in infrared and optical frequency ranges as the plasma frequency approximately is into the ultraviolet region. Therefore the propagation of light is infeasible in metals in these frequency ranges; that is why the metals are shiny and opaque in the visible range. Thin metallic wires were described as one of the earliest structures with negative electrical permittivity [87]. However, a square matrix of infinitely long parallel thin metal wires, enclosed in a dielectric medium, has been recognized an ENG media as shown in Figure 2.7. The propagation of electromagnetic waves in such a structure is similar to propagation in plasma. The electrical permittivity of composite material is negative at frequency ω smaller than ω_p, where ω_p is the structure's plasma frequency. It is a function of the radius and placement period of wires; therefore plasma frequency of such a structure is verified. Plasma frequency for the longitudinal plasma mode expressed as [88]

$$\omega_p^2 = \frac{2\pi c^2}{a^2 \ln(a/r)}. \tag{2.40}$$

Effective permittivity can be written as [89]

$$\tilde{\epsilon_{eff}} = \epsilon_0 \left(1 - \frac{\omega_{\mathrm{p}}^2}{\omega\left(\omega - jf_{\mathrm{c}}\right)}\right), \tag{2.41}$$

where ω_p is the plasma frequency, a is lattice constant, and f_c is the collision frequency of the electrons and corresponds to dissipation due to finite conductivity of wires. As shown in Figure 2.7 the array of metallic wires is similar to bulk material, but as

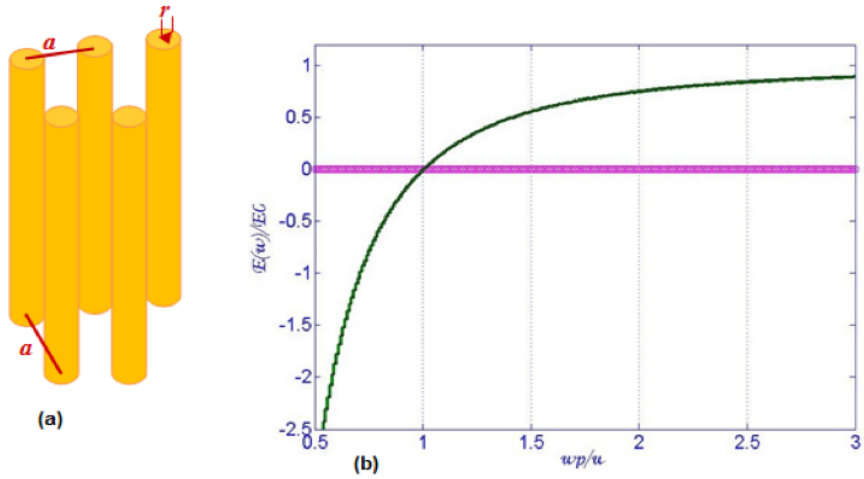

Figure 2.7. (a) Metallic wire media as ENG and (b) effective permittivity plot versus frequency. (a),(b) [34].

they are separated into thin wires with infinite longs, the effective electron density is decreased. The density is proportional to the volume of thin wires to the vacuum area. So the plasma frequency is a function of geometries of wires i.e., the radius of wires and the lattice constant a.

2.6.2. Mu-negative Metamaterials

In MNG-materials, accordingly, permittivity is positive, and permeability is negative. Some gyrotropic materials exhibit such characteristics in a certain frequency range. Materials such as ferrites stay slightly effective are heavy may not own highly acceptable mechanical characteristics [90]. Although antiferromagnets close to resonance frequencies in the far-infrared reveal $\mu < 0$ are natural materials capable of negative magnetic response [91]. In contrast, we will show, microstructured materials can be designed with negative magnetic permeability. The first and the most widely-used MNG-structure is the split ring resonator [1]. SRRs can be both round and square geometrically, as seen in Figure 2.8(a,b). They are characterized as high-conductive resonant structure, in which the capacitance between the two rings counterbalances the inductance. In the presence of a perpendicular time-varying magnetic field applied to the rings, a current is induced at the rings' surface. In return, the current produces a secondary magnetic field. In dependence on the structure's resonant properties, it can either resist or magnify the incident magnetic field, thus concluding positive or negative permeability. MNG-structures includes spiral structures [92], S-shaped [93] resonators, as well as Rolling MNG-structures, termed as Swiss rolls [94] which are entirely suitable for low-frequency applications. For a circular double split ring res-

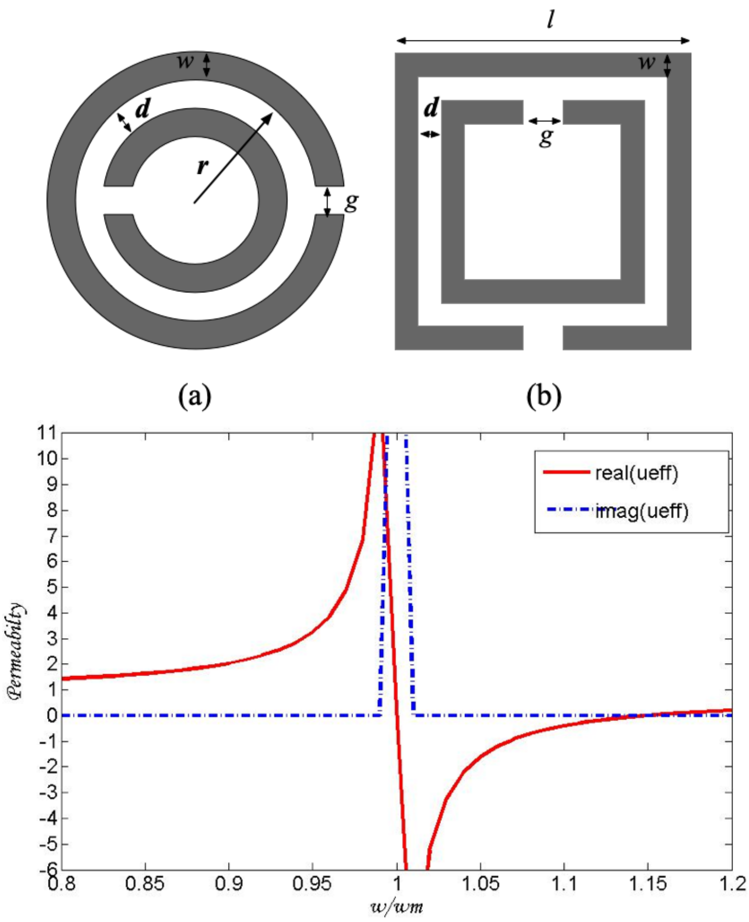

Figure 2.8. The first MNG- material unit cells: a) round, b) square, (c) Permeability of an SRR versus frequency [34].

onator in the vacuum, where the thickness is negligible, we can write the following approximate expression for effective μ [1],

$$\mu_{eff} = 1 - \frac{\pi r^2/a}{1 + \frac{2\sigma i}{\omega r \mu_0} - \frac{3d}{\pi^2 \mu_0 \omega^2 \epsilon_0 \epsilon r^3}}. \tag{2.42}$$

where a is the unit cell length, d is the interval between the rings, r is the radius of the inner ring, and σ is the electrical conductance. As shown in Figure 2.8 (c), magnetic permeability is negative for specific frequencies determined by physical parameters.

2.7. DNG- Metamaterials

Concurrently occurring negative values of ϵ and μ do not belong to the normal materials in nature, so they are created artificially. Such artificial media are named in different sources double negative metamaterials (DNG) [95], backward wave media [96], negative-index materials (NIMs) [97], and negative-phase-velocity [98]. A negative value of the refraction index achieves by negative material constants. DNG metamaterials are also called "Left-Handed Materials" (LHM) [29] because electric field, magnetic field, and the direction of phase velocity follow a left-hand rule system, distinctive from conventional materials (double positive (DPS)). we conclude our discussion in Figure 2.9.

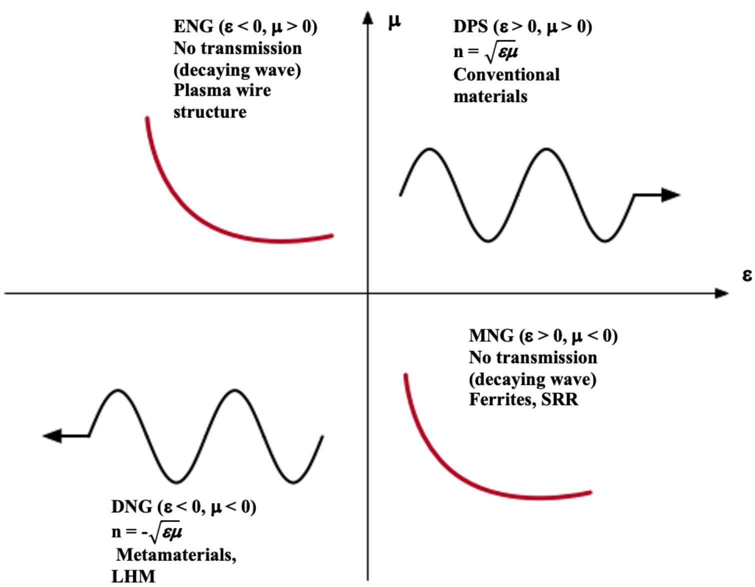

Figure 2.9. ϵ an μ coordinate system

3. BroadBand THz Absorbers based on Square patch Metamaterial

The existence of SRR introduced by Pendry [1] is proven in microwave regime experimentally. By increasing the studies for DNG, the combination of SRR and wires get more interest. Among the papers at terahertz frequencies, Yen et al. achieved a magnetic response at 0.8–1.3 THz in the planar microstructure SRR composites as measured by spectroscopic ellipsometry [99]. It is predicted that numerous applications will thrive within the THz frequency range. In this chapter, we will report the results for DNM we achieved in our previous works at microwave regime [34]. Then we discuss the proposed THz absorber. The proposed model is evolved from a square ring with backside gratings to a square patch with backside blanket metal. Design, fabrication, and characterization are included. The resonance behavior of square ring resonators shows inconsistency by changing the direction of E and H fields. Polarization insensitive absorbers have been the main purpose of this thesis; for this goal, we will focus on designing, characterize, and fabrication of such devices in section 3.2.2. As we will see, the symmetry of patch MM makes them insensitive to the polarization direction. The problem with those MM absorbers is their narrow resonant band. The frequency selective surface (FSS) absorber, consisting of different-size patches, will be an effective method to broaden the absorption band. In the last section, a multiband THz absorber constructed by multi-size square patches is introduced.

3.1. MM Absorber Based on Split Ring Resonators in GHz Band

Split Ring Resonator is one of the commonly used devices that exhibit electromagnetic metamaterial behavior. This device can be defined structurally by single or double metal loops in circular or square shapes with single or multiple splits. Periodic combination of metallic thin wires and SRRs in an array form have attracted much attention recently in technology fields. Negative permittivity and negative permeability are accomplished individually by wire arrays and SRR arrays, respectively. As

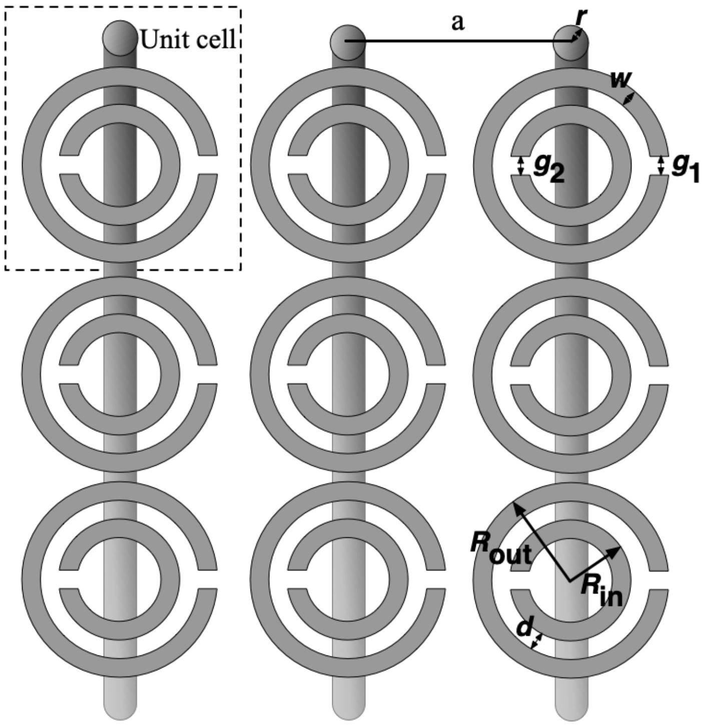

Figure 3.1. Combination of split ring resonator and wire as GHz absorber

they provide simultaneous negative permittivity and negative permeability medium, the electromagnetic wave will propagate; thus, the reflected wave will see a gap at its frequency band. This gap explains the resonance behavior of the SRR + wire structure. In the vicinity of its magnetic resonant frequency, incident EM wave induces a strong circulating current in the metallic loop resulting in resonance. In addition to this magnetic resonance, a strong electric field in the gap exists around the plasma resonance. This is fundamental for an inductive- capacitive resonance of SRR structure. The resonance frequency is determined by the inductance (L) of metallic rings and the gap capacitance (C). The resonant field is susceptible to any change in the gap region. It means resonance frequency shifts as micro-particles are trapped in the gap. This effect has been used for sensing applications [100]. Fabrication compatibility with microelectronic circuits is one of the attractive features of the ring resonators. Complementary split-ring resonators (CSRRs) patterned on the ground plane of a microstrip line provides high sensitivity, which is suitable for detection of cracks in metallic and non-metallic materials [101]. Split-ring resonators have also found applications in the two-dimensional displacement sensor design based on a microstrip line loaded [102]. The flexibility of working around a specific nominal resonance frequency in a very narrow band enhances the utility of SRRs for sensing application [103]. For example, a tunable resonant frequency overlapping half-ring resonator was reported with its magnetic actuator in [104]. The experimental results indicate that changing of an overlapping gap can control the resonant frequency with a few MHz resolution in a tuning range of 38 %. In this section, based on the facts discussed already, we will study SRR Metamaterial behavior. The array construction is made with SRR and wire as shown in Figure 3.1.

3.1.1. Characterization

We model our structure with an RLC resonator, which mathematically can prove the working frequency band of the proposed structure before fabrication. Each ring has a defined R, C, and L value, corresponding to their geometrical properties. Also, we should consider the role of a mutual inductor in between two rings because of the coupling factor.

Table 3.1. Dimensions and expected resonance frequencies of SRR absorbers.

Design	**1**	**2**	**3**	**4**
R_{out} **(mm)**	2.6	3	3.6	4
w **(mm)**	0.9	0.9	0.9	0.9
R_{in} **(mm)**	1.5	1.9	2.5	2.9
g (mm)	0.2	0.2	0.2	0.2
$\mathbf{t}_{metal}(\mu\mathbf{m})$	14	14	14	14
$\mathbf{t}_{Sub}(\mu\mathbf{m})$	130	130	130	130
f (GHz)	5.9	4.73	3.49	3.23

This metamaterial absorber can be interpreted as a two-port network. This two-port network contains two series RLC branches that are parallel. Previously we reported 4 different SRR with various radius sizes. Table 3.1 is concluded the designs and predicted resonance frequencies based on S-Matrix. The scattering parameters are well-suited tools to study the transmission also reflection spectra [105]. They can explain the behavior of a two-port circuit in high frequencies.

The fabricated structure is a double SRR made of copper on an FR4 substrate. In all designs, the thickness of the FR4 layer and metallic strip is constant. Also, the size of the split and the gap between rings are similar and 0.2 mm. A finite difference time domain model (FDTD) has been developed using HFSS to simulate absorption, transmission, and reflection characteristics of devices. The transmission and reflection spectrum extracted and compared with the lumped model we introduced. These would give us useful information about the design of new structures. The transmission spectra for design number 1 and 4 depicted in Figure 3.2. As we expected, because of capacitive and inductive load added to the ring by increasing the rings' dimension, the resonant frequency experiences a blue shift. Increasing the SRRs geometries decrease the resonant frequency.

In comparison between FDTD simulation and LC equivalent circuit models, we can see a mismatch of 20 %. Consider that the results Table 3.1 has concluded, are the resonant frequencies calculated from lumped element formulations. The modeled plots also consider lumped capacitances and inductors even though the FDTD simulation may consider the effects of other parameters such as neighboring mutual capacitances and inductances. Besides, the material properties used in simulations may differ. We add the backside metal wire and expect to see the left-handed effect. Simulated spectra for transmission (blue line) and reflection (red line) of a single unit cell SRR MM are plotted in Figure 3.3. For the MM absorber, we used the dimensions of design number 3. The transmission peak and reflection deep appear at 3.89 GHz. As shown, this structure's behavior is reversed compared to the simple SRR structure (without wire). The structure is reflecting except for a narrow frequency band around resonance.

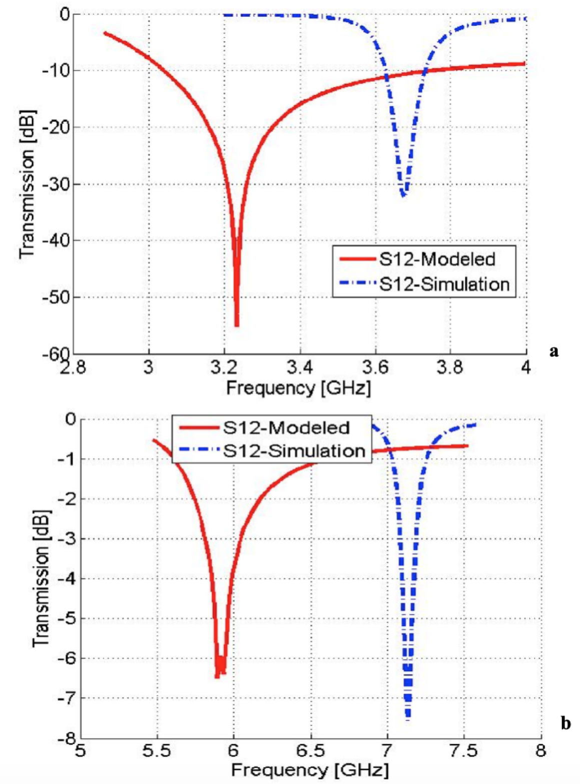

Figure 3.2. Plotted transmission spectrum for (a) Number 4 and (b) 1 designs (4 mm and 2.6 mm radii). The red-line shows the extracted curve from the analytical model, and blue-dash is the HFSS result [34].

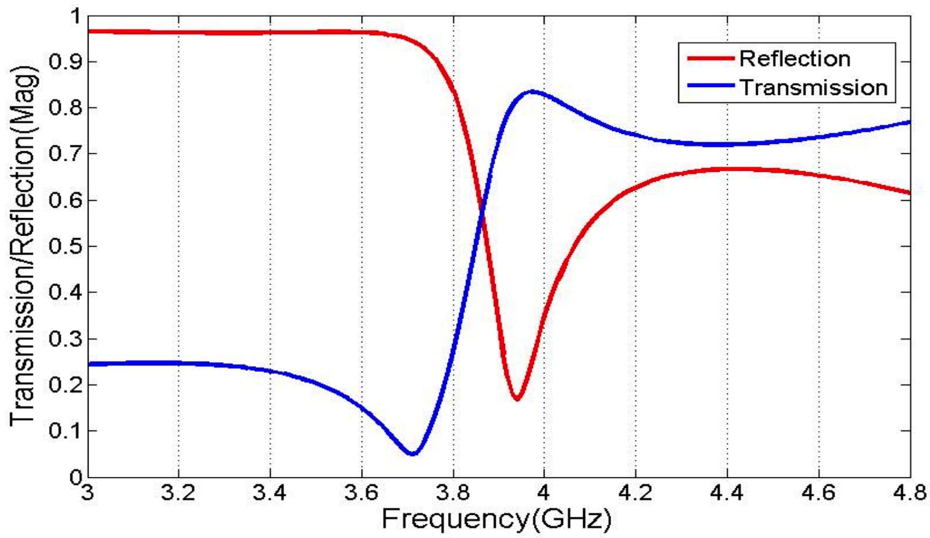

Figure 3.3. Simulated reflection (red line) and transmission (blue line) of proposed Metamaterial design [34].

3.1.2. Measurements

The measurements were performed using a pair of horn antennas and patch antennas at a certain separation between them. Measurements are carried on over the 3-8 GHz frequency band. The measurement for metamaterial designs has been done using a Network Analyzer (Rohde and Schwarz ZVA40).

For the measurements at transmission mode, the antennas should set normal to the sample facade. Transmission measurements were calibrated to the transmission between the horns while the sample is discarded (transmitted power through the air). The reflection mode measurements were carried on by placing the source and receiving horns on the same side of the sample and bouncing the microwave incident beam off the sample. The source and receiver antennas were each bent with an angle of about 7.5 to normal on the sample face. The reflection measurement was calibrated using a sample-sized sheet of copper as a reflecting mirror. In both measurements, the propagation direction was polarized across to the gap. Experimental results are plotted with the results achieved with HFSS to have a comparison as seen in Figure 3.4 It is obviously

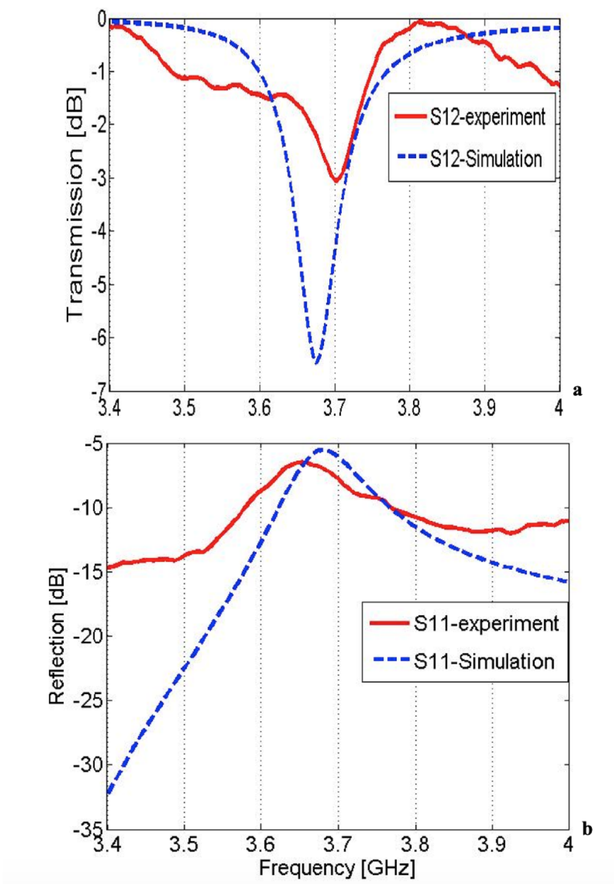

Figure 3.4. Plotted measured (a) transmission, (b) reflection spectrum for number 4 design (4 mm radii). Red-line shows the extracted data from the network analyzer, and blue- dash is the HFss result [34].

seen that there is a good match between numerical simulation and measurement results. These experiments have been repeated several times with different types of antennas for getting more realistic conclusion.

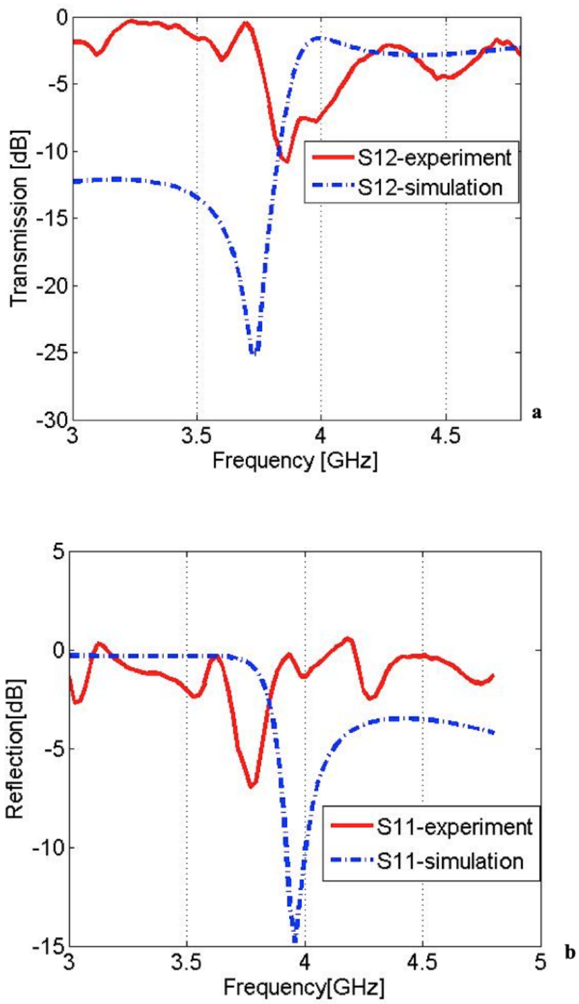

Figure 3.5. Plotted measured (a) transmission, (b) reflection spectrum for MM design (3.6 mm radii). Red-line shows the extracted data from the network analyzer, and blue- dash is the HFss result [34].

The experimental results for MM design are shown in Figure 3.5. At frequencies lower than resonance, we expect to observe zero transmission between ports, but the measurement results show that antennas transmit power out of the resonance band. This comes from the fact that, in reality, antennas transmit power in every direction in an isotropic fashion beside perpendicular mode.

3.2. THz Metamaterial Design

3.2.1. THz MM Absorber Based on Single Square Ring Resonator

We developed our first generation terahertz metamaterial absorber with a single unit composes of two discrete metallic layers: an electrical square ring resonator and cut wires as depicted in Figure 3.6. Magnetic vector of incident wave induces an anti-parallel current in the resonator's arms and cut wires, which generates a circulating current in the square ring, resulting in magnetic resonance (magnetic coupling). This turns the square ring into an inductive loop. The electric component of the incident wave forms a strong and uniform electric field in the gap. E field in the gap excites an electric resonance. Therefore, autonomous of the electric resonance, the magnetic reaction can be adjusted by managing the dimensions of the square ring and distances from cut wires. The square ring with a side length of 32 μm is formed on Parylene as a structural substrate. We fix the width of metallic parts and gap as 2 μm because of limitations in fabrication and mask technology. The metal layer, is lossy gold with a conductivity of $\sigma = 1.0 \times 10^7$ (S/m) on a Parylene base ($\epsilon_r = 2.95$). A 10 μm layer of air separating two metallic elements. The substrate is a silicon wafer.

First the transmission ($|S_{21}|^2$) and reflection ($|S_{11}|^2$) coefficients of a single unit cell were simulated. Perfect electric conductance (PEC) along the $\tilde{x}$ and perfect magnetic conductance (PMC) boundary conditions along $\tilde{y}$ direction were considered (see Figure 3.6) . The equation $A = 1 - |S_{21}|^2 - |S_{11}|^2$ computes the amount of absorption. As depicted in Figure 3.6 the magnetic field induced a circulating current while the ring resonator's gap make of the electirc field to concentarte in it.

The results given in Figure 3.7 are for the case where the E field is along the gap. The other polarization case is presented when the electric field is perpendicular to the gap; an electric resonance can not be excited. Similarly, as the H field is perpendicular to the wires and arms, as parallel wires are not existing for the magnetic field to produce a flux, a magnetic response can not be excited. This behavior is called a polarization-sensitive response. Such a device is desirable for mm-wave, and

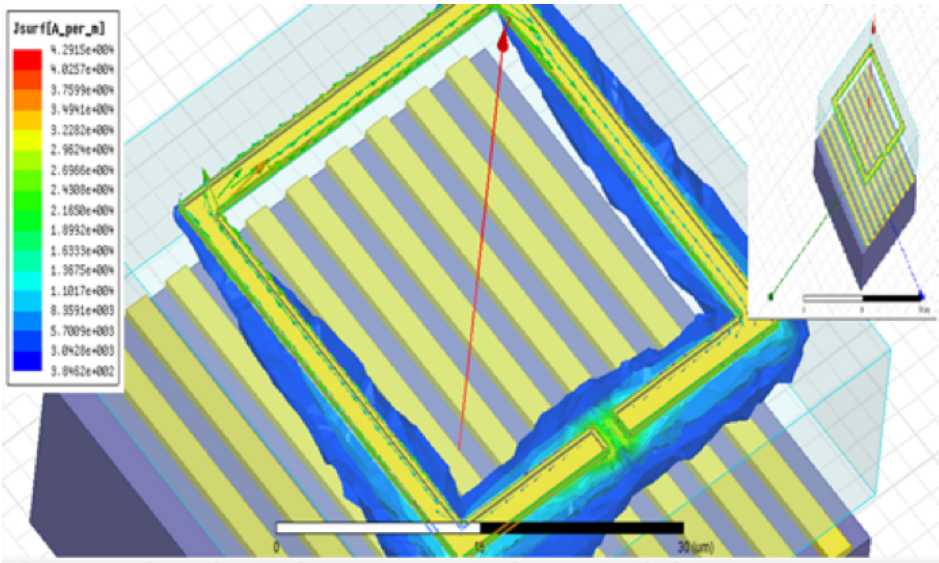

u	44	um	44um	Design
tsub	10	um	10um	Design
w	2	um	2um	Design
tm	0.5	um	0.5um	Design
tg	2.5	um	2.5um	Design
tstruc	10	um	10um	Design
l	32	um	32um	Design
g	2	um	2um	Design
tvac	20	um	20um	Design
hight	60	um	60um	Design

Figure 3.6. Top view layout of the proposed THz absorber: an electric resonator on top of a Parylene spacer; cut wires on Si wafer.

THz imaging applications as saturation of the imager due to reflections from metallic samples deteriorate the performance seriously. The error known as “glint” [53].

3.2.2. THz MM Absorber Based on Square Patch Resonator

As discussed in section 3.2.1, square rings’ polarization sensitivity motivates us to design a model that is polarization independent. The other optimization we considered is to eliminate the transmitting power among the ports to increase the absorptivity. For this aim, THz metamaterial absorber was designed using a metallic square patch made of titanium separated from another Ti ground plane on a Si wafer by a Parylene layer

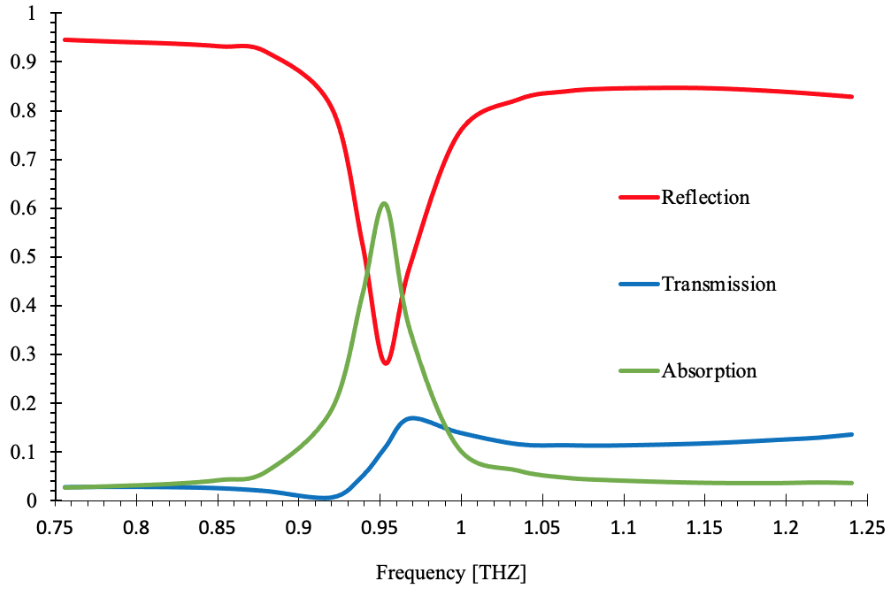

Figure 3.7. Simulated reflection (red) and transmission (blue) for the electric square ring resonator and cut wires. The absorptivity (green) results in a value of 60% at 0.95 THz. Reflection .

as schematically illustrated in Figure 3.8. Impedance matching to the free space at certain THz frequencies cancels the reflection employing that kind of combination. At the same time, the ground plane blocks transmission, which causes raising the amount of absorption.

A single unit cell of the absorber has two distinct metallic layers made of 200 nm-thick titanium, much thicker than the typical skin depth of metal in the THz regime. A square patch as a resonator and a ground metallic layer as transmission eliminator are utilized. The side length, l, of the square patch is adjustable. Parylene thickness is 2 μm which is placed as a spacer. All structures are implemented on a Silicon substrate.

3.2.3. Characterization

The most important aspect of using metamaterial is achieving a negative refractive index. Refractive index in terms of frequency-dependent permittivity ($\epsilon(\omega)$) and

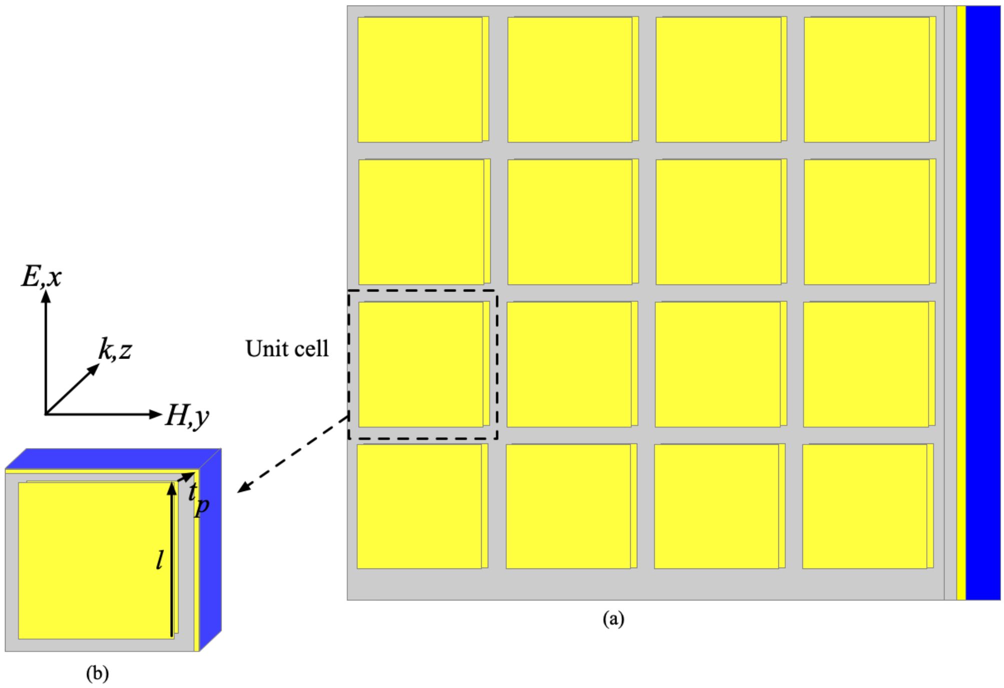

Figure 3.8. THz absorber based on square patch metamaterial structures.

permeability ($\mu(\omega)$) is given as;

$$n(\omega) = \sqrt{\epsilon(\omega)\mu(\omega)}. \tag{3.1}$$

In this part, it has been shown that by engineering multilayer structure, the real portion of the index can be negative, and the imaginary part of complex refractive index, which defines the loss, can be maximized or minimized corresponding to the application. Strong absorption as a result of the maximum amount of imaginary portion of $n(\omega)$ can be achieved by tuning the $\epsilon(\omega)$ and $\mu(\omega)$ through devices are made artificially. Therefore, it is possible to absorb electromagnetic wave by tuning $\epsilon(\omega)$ and $\mu(\omega)$, and achieving excellently match the impedance to the free space: $Z(\omega) = \sqrt{\mu(\omega)/\epsilon(\omega)} = 377\Omega$. Matching the impedance to free space, i.e. $\epsilon_r(\omega) = \mu_r(\omega)$ thus Z $= Z_0$ minimizes the reflectance at a specific frequency.

An equivalent LC resonator circuit [106, 107] with resonant frequency of $1/\sqrt{LC}$ can describe the behaviour of electromagnetic radiation inside a metamaterial structure. Faraday's law prescribes that a time-varying magnetic field confronting a small coil of conducting wire induces a current into it with inductance L. Due to skin effect, induced current concentrates toward the metal surface as the frequency becomes higher. The skin depth becomes around 100 nm and less (Au at 1 THz has a skin depth of 82 nm) near the terahertz region [108]. Ampère's law characterizes a local magnetic dipole moment which is generated by induced circulating current. Now consider that we excite a single unit cell as E-field along $\tilde{x}$ and H-field is along $\tilde{y}$ direction. The self-inductance of a single patch can be calculated utilizing the current sheet theory. A current sheet is a extermly thin conducting sheet (Figure 3.9). Current flows circumferentially around the sheet, producing a magnetic field inside the sheet. The approach, presented by Welsby [109] which is simple to apply to the critical problems. The produced results are mostly acceptable. For a current sheet where $l \gg t_p$, the inductance can be estimated as follows;

$$L = \mu_o \mu_r \frac{A}{l}, \tag{3.2}$$

where A is the cross-sectional area of the current sheet and equals the side length of patch times thickness of spacer: $l \times t_p$, it is obvious that inductance is just a function of the thickness of spacer (Parylene). The total capacitance, C, explains the charge growth the external electric field induced. it can be calculated with a parallel plate model,

$$C = \epsilon_o \epsilon_r \frac{A}{d}, \tag{3.3}$$

where A is the area of overlapping plates and d is the distance between the plates, in this case, the spacer's thickness, t_p. Substituting L and C formulas will give the resonance frequency f_0,

$$f_0 = \frac{1}{2\pi\sqrt{\alpha\beta l^2}}. \tag{3.4}$$

The resonance frequency of a patch MM is a function of side length, as it is proved

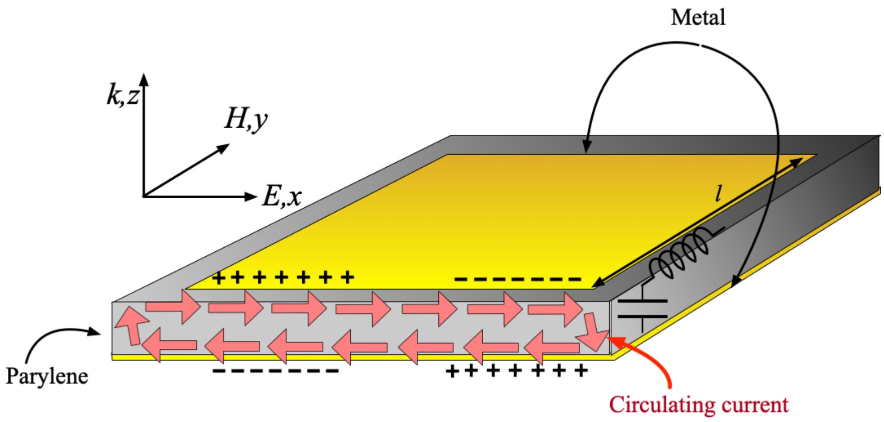

Figure 3.9. Single patch MM absorber modeling based on lumped inductance and capacitance.

by Eq. 3.4 and the dielectric constant of the spacer. α and β are mathematical factors proportional to effective permittivity and permeability of the spacer between two metallic layers. We started our design with patch sizes which correspond to 1 THz resonant frequency. According to equation 3.2 to 3.4, 90 μm-side length patch results in a resonance at 1 THz.

3.2.4. Simulation

Based on the FDTD by CST Microwave Studio software, a full-wave EM simulation has been performed. Boundary conditions are periodic and used in the $\tilde{x}$ and $\tilde{y}$ directions (see Figure 3.9), and a plane incident wave hits the MM unit cell structure along $\tilde{z}$ direction with the electric field polarized along the $\tilde{x}$-direction and the magnetic field along the $\tilde{y}$-direction. Ports are placed in $\tilde{z}$ direction. For TEM plane wave incident to the proposed structure, no transmission can be monitored, as the continuous Ti films block it off. Hence, the absorption equation is $A = 1 - |S_{11}|^2$ in our designs. The period of the square patch array (i.e., the length of the unit cell) along $\tilde{x}$ and $\tilde{y}$ directions are 90μm. The length, l, of the square patch is adaptable and are chosen as 86, 76, 65, 53, and 43 μm. It is clear that for $l = 86\mu$m the resonance occurs at 0.86 THz and the amount of absorption for 86 μm patch is 42 %.

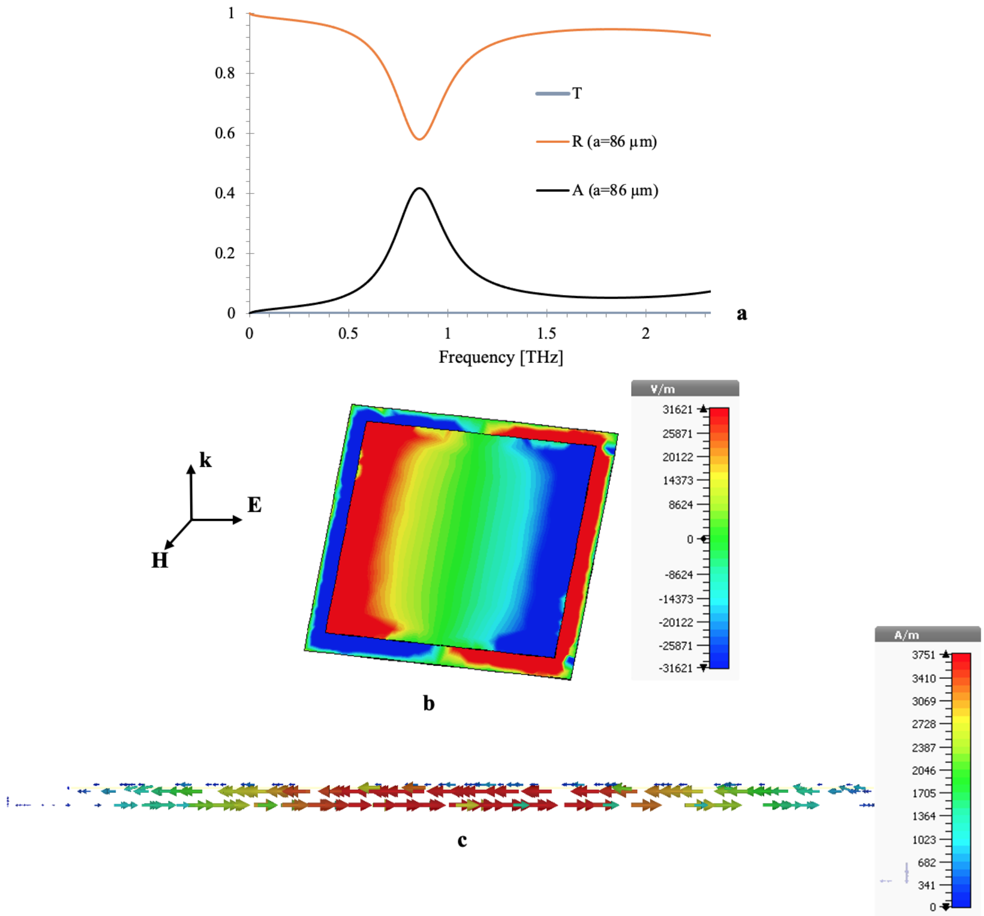

Figure 3.10. (a) Simulated transmission (T), reflection (R), and absorption (A) for the single square patch absorber structure, (b) electric field distribution, and (c) surface current distribution density.

To obtain physical insight, the electrical field distribution and surface current distribution were simulated at resonance as shown in Figure 3.10 (b,c). The E field distribution shows a positive to negative charge polarization in the upper metallic layer, which induced opposite charges to the lower metallic layer, causing capacitance formation as predicted in Figure 3.9. It is noticed that the currents are circulating at surface in a way that they are anti-parallel in the two metallic parts and based on the right-hand rule, circulation trend pointing the magnetic field direction (strong magnetic coupling) [110]. An electric excitation causes the square patch to form a dipole, which couples to the incident EM wave's external electric field, makes resonance happens in higher frequencies (beyond 2.5 THz). It is worth noting that the symmetrical properties of the structure make it polarization-insensitive for normal incident EM waves; hence, changing E and H field direction does not affect the resonant behavior. The absorbing property of this MM is additionally investigated by changing the side

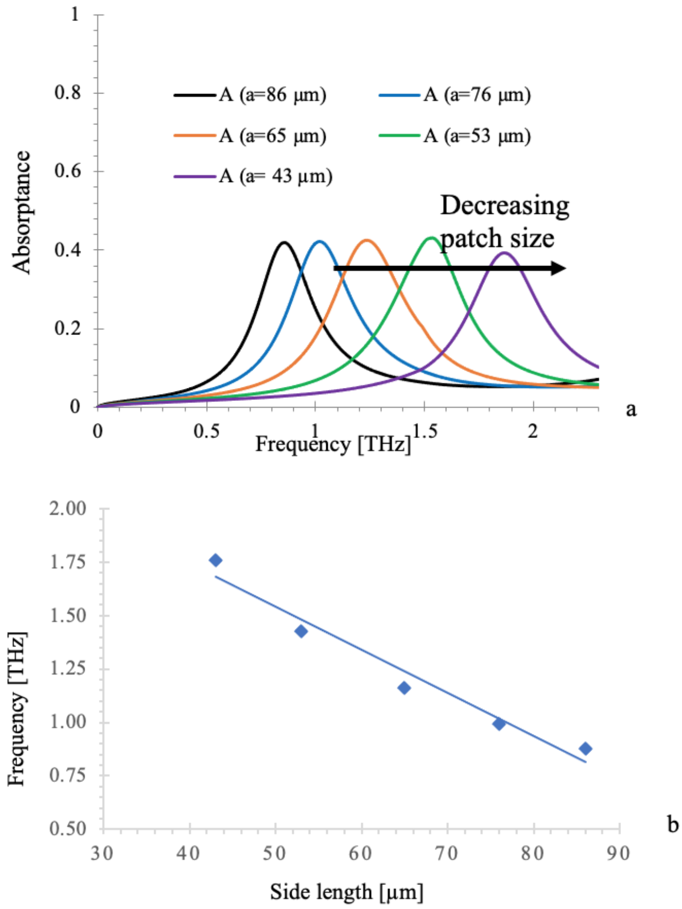

Figure 3.11. (a) Absorption spectra for various side length sizes, l, of the square patch, (b) the dependency of the resonant frequency of absorption on the side length of square patch, l.

length, l, of the designed square patch structure. As illustrated in Figure 3.11, there is a exceptional blue-shift of the resonant absorption peak frequency when l decreases from 86 μm to 43 μm. The linear dependence of the resonance frequency on square patch length, l, is proved as adjust-ability by Eq.3.4, which agrees well with the dependence of simulated peak value. Simulation results with individual square patch structures verify the resonant frequency's dependency to the patch size as shown in Figure 3.11

(b). We must note that in the case of the parallel plate capacitor, Because of the fringe effect as the electric field extends from the edges, the overlapped area is more than the case when we neglect the fringing capacitance. Thus the capacitance calculated by the formula is less than the actual value.

3.2.5. Multiband and Broadband THz Absorber

A parametric sweep with different side lengths, l, of square patches motivates us to assemble a multi-band or broadband perfect THz MM absorber by mapping different patches based on the multi-resonances mechanism at various adjacent frequencies. In this part, we will try to increase the absorption bandwidth by using multi-square structures with different geometries that can maintain various resonant modes placed in vicinity of each other in the absorption spectrum.

Here, the unit cells of four designed THz MM absorber structures are shown in Figure 3.12 (a), which comprises five Ti squares with different dimensions departed from a Ti ground plane by a Parylene layer. To optimize the absorbing spectrum as broadband, as we predicted from the fit function (Figure 3.11(b)), designing semi-size patches would satisfy our aim as they will have very close resonant frequencies. Five patch sizes of 86, 76, 65, 53, and 43 μm are combined in 4 different ways to construct the broadband absorber as shown in Figure 3.12(a). It is evident from Figure 3.12(b) that no matter how we select the different-size patch device arrangement, there always exist resonant peaks corresponding to the side length of a single square patch. The absorption level for all design types is less than 30 %. For less covered samples with patches (design 3), 20 % of incoming EM wave can be absorbed. Design 1 consists of different patch sizes in rows. Each row contains one specific patch size. The simulation result shows peaks at 0.9 THz, 1.09 THz, 1.21 THz, 1.5 THz, and 1.8 THz, which match with predicted resonances coming from a single patch absorber. There is a drop in quality factor with decreasing the patch size as smaller patches are less reflective than larger ones. In this topology for smaller patch sizes, we tried to fit more patches and cover the area as much as possible to compose a mirror surface. The absorption spectra for design 2 is similar to design 1, as we changed the position of rows among

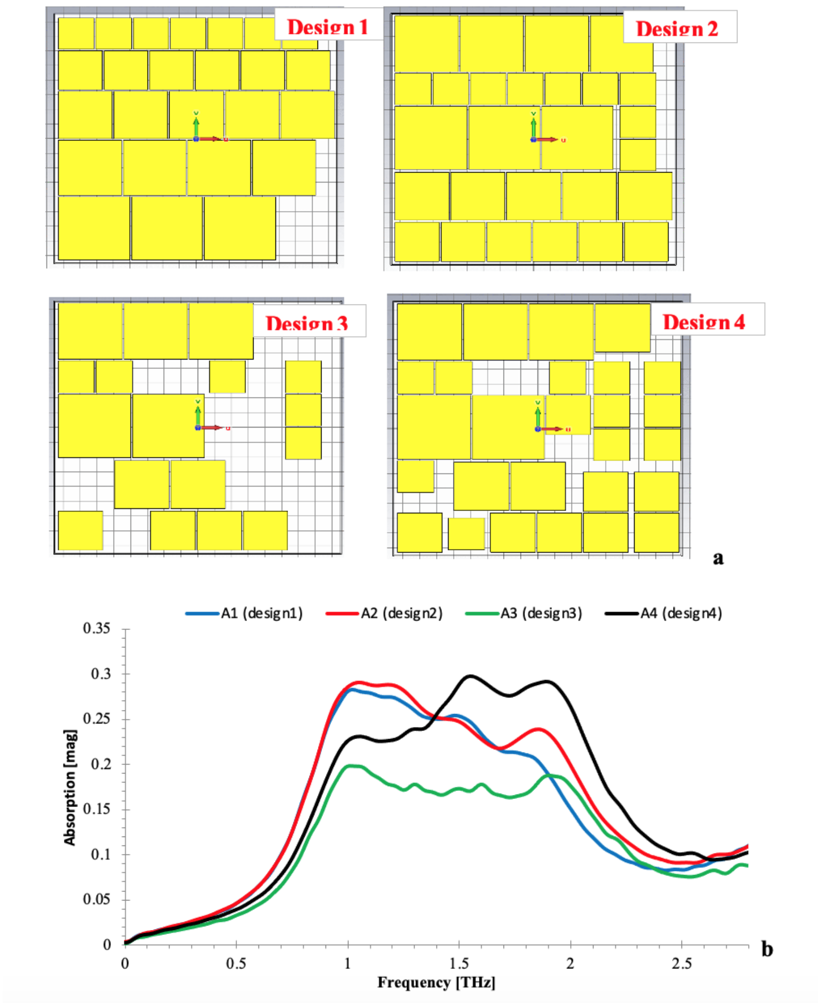

Figure 3.12. (a) Scheme of the unit cells of the broadband THz absorbers based on square patch MMs, (b) simulated absorptions bands for different patch configurations.

them. Design 3 and design 4 are randomly patterned structures. We expect to see similar absorption peaks with two previous designs at corresponding frequencies to the patch sizes. Absorption spectra of single square patches are overlapped to broaden the bandwidth of the THz absorber. The absorption band of new designs is greater than 15% from 0.8 to 2.2 THz. The "full width at half maximum" (FWHM) is about 1.22 THz for design number 1, is about 1.32 THz for design number 2, is about 1.5 THz for design number 3, and is about 1.4 THz for design number 4, which is wider than the previous design of single patch size structures. From the simulated results, to obtain broadband absorption, we should design the combined patch MMs with slightly different side length sizes to guarantee that the resonance frequencies can be closely packed next to each other to broaden the absorption spectra.

3.2.6. Measurement Results

The proposed devices were characterized with a THz spectrometer. For a brief introduction to THz time-domain spectroscopy, refer to Appendix A. We measured the fabricated samples' absorption characteristics using a terahertz time-domain spectroscope (THz-TDS, TERA K15, Menlo Systems GmbH, Martinsried, Germany) maximum optical power of 80 mW, employing a 1550 nm femtosecond fiber laser with a spot size of 2 mm. The laser repetition rate is from 80 MHz to 250 MHz for the transmitter and the receiver. The spectral range is 3 THz, and the spectral resolution is 5 GHz.

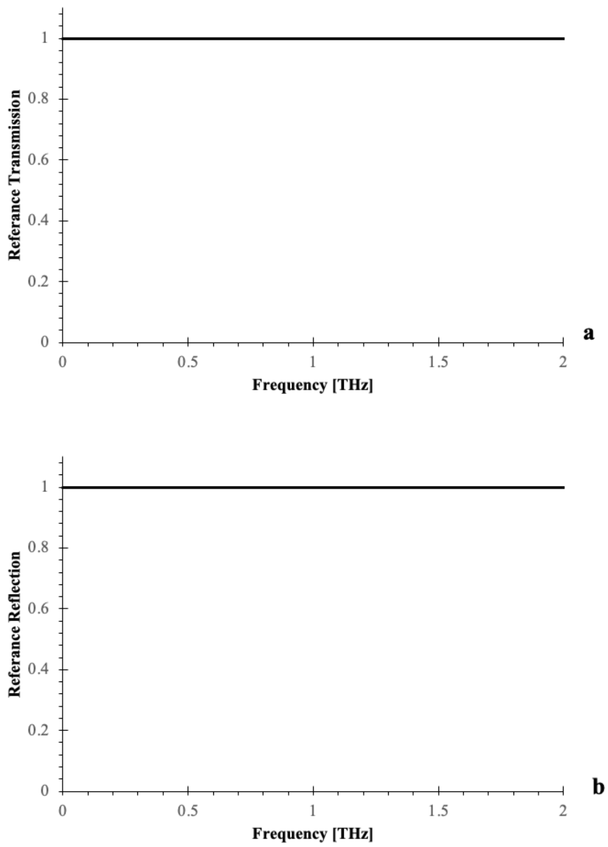

Figure 3.13. Measured reference data for (a) transmission and (b) reflection modes.

First, we collect the reference data for transmission and reflection modes. In transmission mode, first, we measure the amount of emitted energy by using the receiver antenna. Simultaneously, no sample is present between the emitter and the receiver antennas of the spectrometer. Then we placed a thick metal reflector (in this part, a Si substrate coated by a thin layer of Ti) between the antennas inclined 90 to collect the reflectance reference. The reference data for transmission and reflection are shown in Figure 3.13. Before starting the measurement of scattering parameters for designed samples, we have characterized the behavior of common materials such as air, copper plate, and bare silicon substrate in THz frequencies. The results are gathered in Appendix A.

In this part, we report the measured data for design number 4 previously mentioned. We illuminated the whole array. We obtained the absorber's transmission and reflection spectra using reference measurements and calculated the absorption spectrum shown in Figure 3.14. As can be seen in Figure 3.14(a), the experimental transmission characteristics of the square patch sample together with blanket metal is zero. The array depicts absorber characteristics between 0.4 THz and 1.7 THz. The FWHM is about 1.03 THz. Notice that there is a good match between the results of the experiment and simulation. However, measured R differs slightly from that simulated. We should note that we estimated values used in the simulation for the material properties of Parylene based on published values at lower GHz frequencies [111]. Further, the Parylene layer's and metallic film's thickness were designed to be 2μm and $200n$m respectively. In reality, physical parameters are measured to be closer to these values. Measurements in reflection mode for Si substrate is one of the difficulties. Reproducing the reference data is complex as Si depicts resonance behavior in THz frequencies. (Refer to Appendix A for more detail).

3.2.7. Further Discussion on Second Order Effects

In the patch broadband absorber design, we have an obvious problem: quality factor which corresponds to the amount of absorption. We aim to design and fabricate a perfect absorber that absorbs more than 90 % of incident EM wave power. Let us

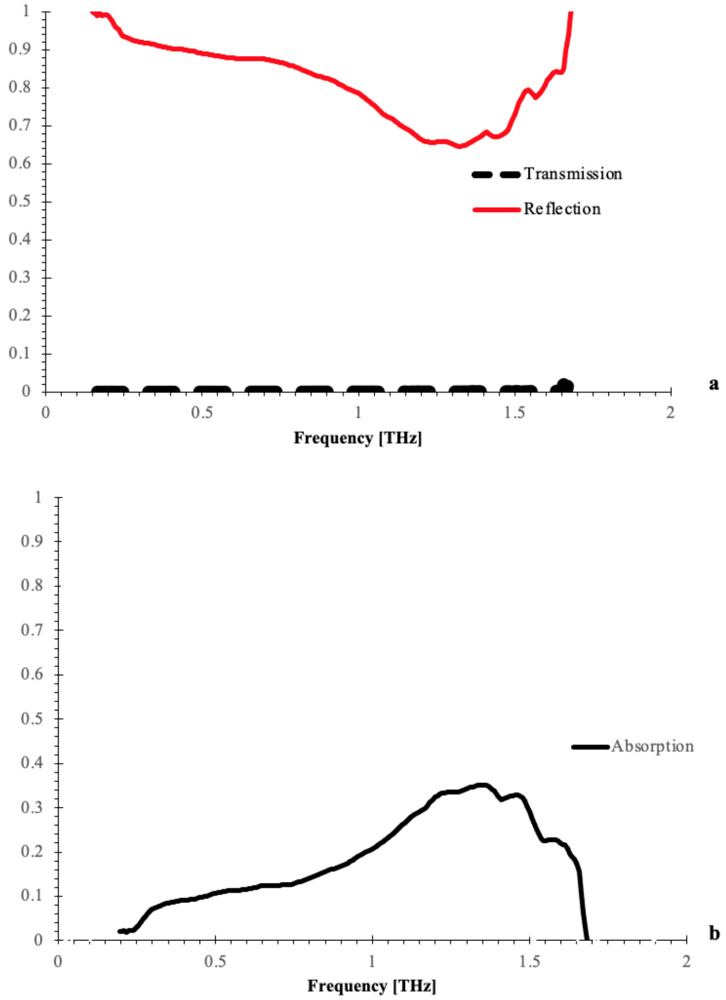

Figure 3.14. Measurement results for design no.4 (a) reflection and transmission, (b) absorption.

discuss the lumped model more by including the resistance. From the current flow schematically described in Figure 3.9 and from the voltage distribution, it is clear that the distributed capacitance between the upper metallic film (with the side length of l) and the lower blanket metal are connected in series with the total inductance of unit cell. The distributed capacitance is modeled as two lumped capacitors among edges. The accurate equivalent circuit for lossy conductors status of the multi-layer resonator is now shown in Figure 3.15. We added a series resistance, R_{sc}, to take the conductor's losses into account. The current passing through the same path with the path of total inductance and, thus, R_{sc} is in series with the total inductance. Therefore, we can cast the total series resistance in the same form as L, and written as $R_{sc} = \rho l/A$ which ρ is the electrical resistivity of the metal and t_p is the thickness of the spacer layer (Parylene). Thereby, assuming that the metal thickness is smaller than the skin depth, the final expression of the total series resistance given as;

$$R_{sc} = \frac{\rho \cdot l}{A} = \frac{\rho}{t_p}. \tag{3.5}$$

As comes from Eq. 3.5 the series resistance is a function of distancing between metallic layers (spacer thickness). This resistance R_{sc} determines the amount of power absorbed due to Ohmic losses.

One of the main concerns related to metamaterials is their narrow bandwidth of operation, which comes inherently. The bandwidth of the metamaterial is directly related to the resonance performance. The resonant circuit presented in Section 3.2.3 can drive the resonance behavior of the compositions. It is also acceptable to analytically demonstrate the foreseen operative bandwidth of a metamaterial. A reliable evaluation of the bandwidth may be determined as the inverse of the quality factor Q related to the resonance of the individual patch resonator. Considering generic equivalent RLC circuit representations like the ones proposed in Figure 3.15, one can write the quality factor in the presence of the loss in the metallic conductor as [112]

$$\frac{l}{Q} = \frac{1}{Q_c}, \tag{3.6}$$

where Q_c is the quality factor related to the losses in the metallic conductor in series and is given by

$$Q_c = \omega_0 \frac{L}{R_{sc}}, \tag{3.7}$$

which ω_0 is the angular resonant frequency of the circuit and equals to $\frac{1}{\sqrt{LC}}$. Substituting resistance, inductance and capacitance prove that the quality factor is proportional to thickness squared and inversely related to side length. Increasing the spacing between metallic layers will increase the Q factor. It means that one could achieve maximal loss by modifying the side length l of the square patch and the thickness of spacer t_p accurately at a resonant frequency. The amount of separated distance has a limit so that the induced charges between metallic layers will maintain the coupled electric field ($E \propto t_p$). This will guarantee the presence of capacitance, thus the resonance.

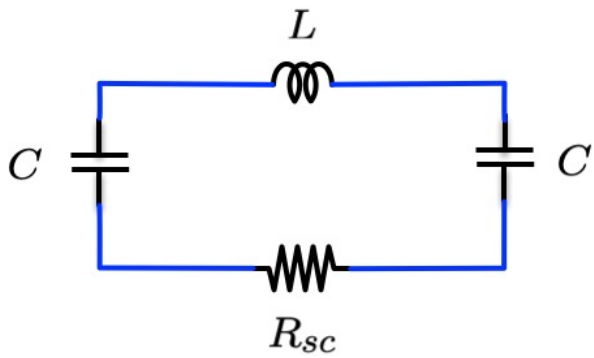

Figure 3.15. RLC equivalent circuit for a lossy patch absorber.

We should mention the fringing effect once more as one expects an increase in the resonance peak due to decreasing the side length size. By reducing l, the overlapping area between metallic layers decreases; thus, the fringing effect dominates, causing a drop in Q factor, enhancing bandwidth. (See Figure 3.11 (a).) In the next chapter, we will introduce a layer of air gap beneath the Parylene layer to minimize the power reflected from the surface, which is resolute with our intent to match the free space's impedance at resonance, thus absorb much more radiant power. Furthermore, this air layer gives the proposed structure the ability of mechanical movement.

4. A MEMS-Based Terahertz Detector with Metamaterial-Based Absorber and Optical Interferometric Readout

4.1. Overview

High-performance terahertz absorbers can help develop new devices for biomedical imaging purposes [113], detection of explosives, surveillance or quality control purposes [24,114,115]. The lack of natural materials exhibiting high THz absorption makes artificial material absorbers used in THz frequencies very attractive. While sensing in the terahertz regime is flourishing, metamaterials have been presented for terahertz applications [116, 117]. Metamaterials are artificially engineered structures that exhibit unique properties such as negative values of the index of refraction [118–120]. Metamaterial-based terahertz absorbers can absorb EM radiation 100% at resonance and can be utilized as sensors, and detectors [41, 121, 122]. In this chapter, we present a MEMS-based thermo-mechanical detector operating in 0.5-2 THz band. Absorption of the incident THz wave is accomplished by metamaterial-based absorbers, which are patterned metallic square patches on a suspended Parylene pixel.

Integration of simple metallic metamaterial structures to the detector eliminates the need for exotic materials that exhibit high absorption at the THz band. The suspended pixel is mounted on a substrate coated with a layer of the metallic film. The metallic film on the substrate comprises grating structures underneath the suspended pixel. The gratings cover a portion of the pixel and are used for optical displacement readout of the suspended structure. The principle of operation of the proposed device can be summarized as follows. The absorbed THz radiation is converted to heat on the pixel. This causes an increase in the temperature of the released pixel that is thermally isolated from its substrate. The increase in temperature induces mechanical deflection due to suspensions made of materials with different thermal expansion coefficients. The mechanical displacement of the pixel is read out by optical means using a diffraction grating interferometer, which has been employed with thermomechanical infrared detectors [123, 124]. Since the detector's absorption characteristics are based on the metamaterials' geometrical properties integrated into the suspended structure, it is feasible to realize broadband detectors with multiple patches with different geometries on a single pixel. On the other hand, it is also possible to design a detector that is sensitive to a narrow band of interest by integrating a single type of patches on the suspended structure. This is advantageous for thermomechanical detectors as electrically passive detectors can be designed. Therefore, the detectors' thermal conductance can be minimized since there is no need for electrically conductive layers that are also usually thermally conductive. Also, electrically passive thermomechanical detectors do not suffer from Joule heating. We implement a diffraction grating interferometer for the readout, which has been demonstrated as a sensitive readout method for various MEMS devices [125]. It is possible to utilize the readout method for large focal plane arrays using CCD/CMOS cameras [124]. The MEMS chip can also be integrated with a CMOS chip for integrated readout configuration [123]. A typical bi-material detector (see Figure 4.3(a)) consists of a sensing element (absorber) responsible for converting incoming radiation to heat which is transmitted by conduction to two symmetrically located bi-material beams (bi-material legs) connected to the host substrate (heat sink) by supporting structures of lower thermal conductance (anchors). The bi- material legs undergo bimetallic deformation [13] due to the temperature rise upon absorption of incident radiation. The deformation can be probed by different approaches such as piezoresistive [14], capacitive [15, 16] and optical readouts [8, 12, 17, 18]. The latter requires a reflective surface, normally embedded into the absorber, and has the advantage of avoiding the complex on-chip integrated microelectronics necessary for other approaches. Several bi- material based sensors have been demonstrated for IR detection and imaging [8, 19–22]. These detectors either use IR sensitive structural materials such as SiNx and SiO2 or, alternatively, integrate separate IR sensitive layers into the detector. Additional difficulties exist when the detection range is extended to the THz region. The low thermal background power in THz demands highly sensitive detectors and, in most cases, external THz illumination is also required [7–12].

4.2. Metamaterial Absorber for Sensing Applications in THz Frequencies

The primary part of the THz detector is a freestanding movable structure that contains the THz absorber. Chapter 3 introduced a THz absorber based on patterned square patches on a Parylene dielectric layer. To allow the structure to move, we added an air gap. Figure 4.1(a) shows a unit cell of a metamaterial-based terahertz absorber that includes a patch on top of a freestanding Parylene layer of 2 m. The substrate is silicon. A metallic layer for blocking the transmission power is deposited on silicon. There is an air gap separating the Parylene layer and substrate. Patch size varies as of 86, 43, and 30 m.

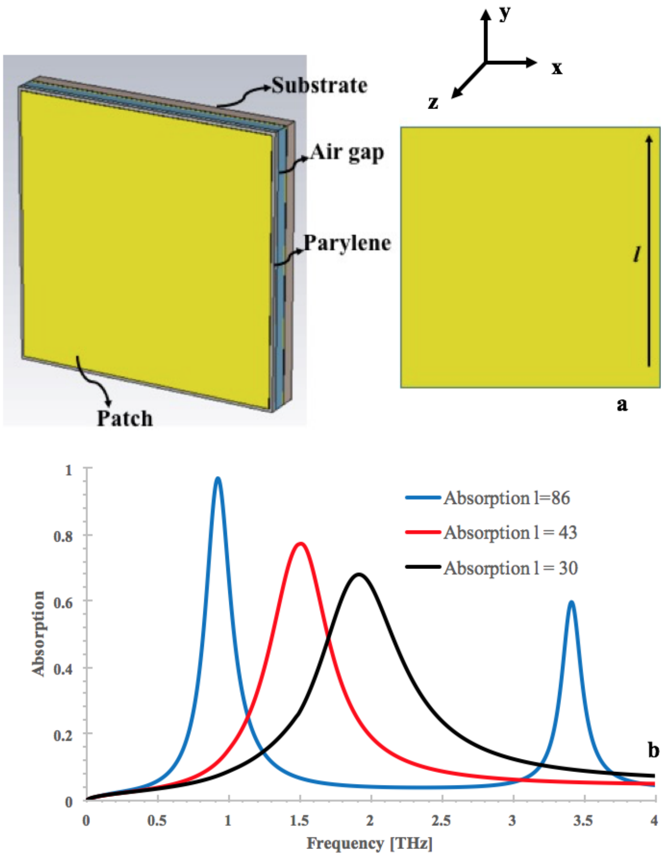

Figure 4.1. (a) Structural schematic of 2D patch absorber, metallic patch size is varying as of 86, 43, and 30 m, (b) absorption spectra for different patch sizes.

Qualitatively, the unit cell is a resonator with resonant frequency of $(f = \frac{1}{\sqrt{LC}})$.

Since as we have proved in Chapter 3 , the capacitance depends on l^2, the resonant frequency of the structures is inversely proportional to the size of the patches, which expected with the simulation observations as illustrated in Figure 4.1(b). The design of the metamaterial structures was performed by FDTD modeling using CST Microwave software. The metamaterial structures' periodic nature allows the simulation to be performed in a unit cell with the appropriate boundary conditions. Perfect electric and perfect magnetic boundary conditions are considered along $\tilde{x}$ and $\tilde{y}$ direction respectively. Incident plane wave is distributed along $\tilde{z}$ direction where we placed the ports to calculate the S parameters. The scattering parameters obtained from the ports determine the proportion of that power that is "reflected" ($R = |S_{11}|^2$) and "transmitted" ($T = |S_{21}|^2$). The dielectric constant of Parylene at THz frequencies was taken from [111] as $3 + 0.3i$ and conductivity of 1.798×10^6 S/m was used for Ti. Let us consider the largest patch where the side length is 86 m. The first resonance frequency, at 0.92 THz, was identified as magnetic resonance. The magnetic field is along the y-axis, and it supports circulating current passing through the patch and bottom plate. Besides, the electric field polarized the patch and divided it into two symmetric portions. This results in two identical circulating currents in the left and right halves of the structure as shown in Figure 4.2 (b) (dipole oscillation). The second resonance frequency is observed at 3.4 THz, which is identified as an electric resonant frequency. The conductive path is much shorter than the one in the first mode, so the resonance is locating at a relatively high frequency. The arrows (proportional plot) in Figure 4.2(b) represent the antiparallel currents excited in the two metallic layers in the metamaterial unit cell, while the colored layers in Figure 4.2(a) represent the electric field magnitude. Current distribution takes place in the surface, which indicates that the metallic planes are thicker than the skin depth of Ti (σ is 40 nm for 1 THz), which is a necessity to obtain absorption close to 100% . Notice that there is no transmission of the incident wave or electric field distribution in the substrate and below it.

The electric field distribution is mainly focused on the edges of the square patch structure. We can conclude that the coupling strength of the electric dipoles and the magnetic response are mainly determined by the separation distance (the spacer layer thickness) and the square patch's side length, l; the side that the external electric field

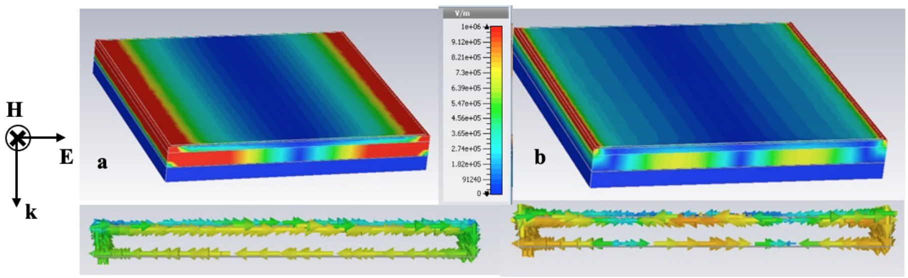

Figure 4.2. (a) Electric field and surface current distribution at resonant frequencies (a) 0.96 THz and (b) 3.34 THz .

is along it. It means that maximal absorption will be obtained by proper formulating of the side length of the square patch and the separation distance at a specific resonant frequency.

4.3. Suspended Array of Square Patch Absorbers for THz Applications

In this part, we present a metamaterial-based terahertz absorber employing metallic square patches with different sizes implemented in the same plane. Figure 4.3(a) shows a three-dimensional drawing of an absorber structure that includes a 4×4 array of patches with a size of 43 μm at the center of the free-standing Parylene layer. The absorber also includes two rectangular patches with a size of 100×43 μm. The metallic patches are fabricated on top of a patterned Parylene layer suspended over a metalized substrate.

Figure 4.3(b) shows the reflection, transmission, and absorption spectra of the absorber obtained using commercially available electromagnetic simulation software (CST Studio Suite, Darmstadt, Germany). The patch structures introduce electric dipole resonances at specific frequencies induced by the electric field in the patches' plane. The absorption spectrum in a band of 0.3-2 THz exhibits two peaks at 0.59 THz and 1.49 THz, respectively. The resonant frequency of the structures is inversely proportional to the patches' size as given by Eq. 3.4. The larger rectangular patches

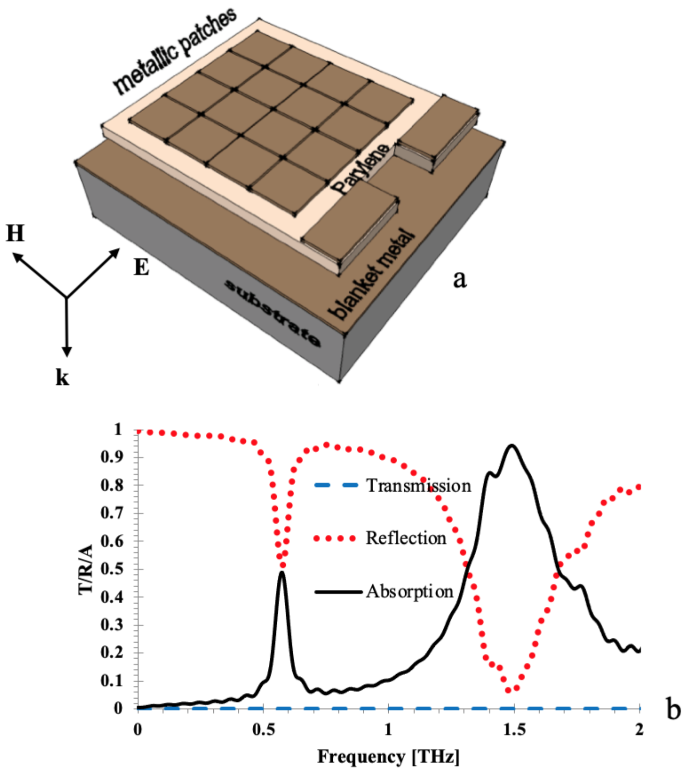

Figure 4.3. (a) Three-dimensional drawing of a metamaterial-based terahertz absorber with a 4x4 array of patches with a size of 43 μm and two rectangular patches with a size of 100x43 μm. (b) Simulated transmission, reflection, and absorption spectra of the absorber [126].

excite a resonance at 0.59 THz, while the smaller square patches excite another resonance at 1.49 THz. The array formation of the square patches enhances the peak of the absorption at the resonance. Note that the maximum absorption for a single 43 μm patch is 0.77, where for the array case, it increases to 0.94. The bandwidth in array form decreases to 260 GHz, whereas it is 415 GHz for a single unit cell.

In the next steps, we implemented absorbers employing different configurations of square patch arrays made of titanium with side lengths of 86 μm, 43 μm, 30 μm and rectangular patches with side lengths of 100 μm and 43 μm on a single free-standing

Parylene layer. The thickness of the patches and the blanket titanium film underneath the patches is 200 nm. The Parylene layer is implemented in a 2 μm-thick released mesa. The thickness of the air gap between the Parylene layer and the blanket metal is 5 μm. The patches' layout is shown in Figure 4.4(a). The computational model for the absorber includes all the structures shown in Figure 4.4(a).

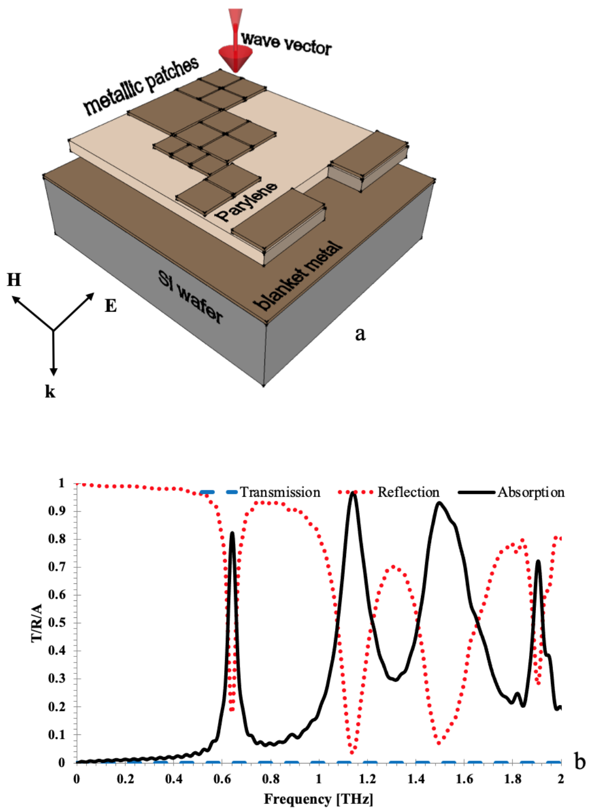

Figure 4.4. (a) Three-dimensional drawing of the metamaterial-based terahertz absorber structure with an array of patches with sizes of 86 μm, 43 μm, 30 μm and two rectangular patches with a size of 100x43 μm. (b) Simulated transmission, reflection, and absorption spectra of the absorber [126].

The intended configuration for the absorber is when the wave vector is perpendicular to the device. The electric field is along the y-axis in the simulations. The reflection, transmission, and absorption spectra of the absorber are shown in Figure 4.4(b). The absorption spectrum exhibits sharp resonant peaks at 0.63 THz, 1.12 THz, 1.48 THz, and 1.87 THz. As we expect from simulation results of single patch unit cells, the corresponding resonances occurred with slight differences with single ones;

this variation comes from coupling between various-size square patches. Compared to Figure 4.3, it can be seen that incorporating patches with different sizes improve the absorption characteristics of the device.

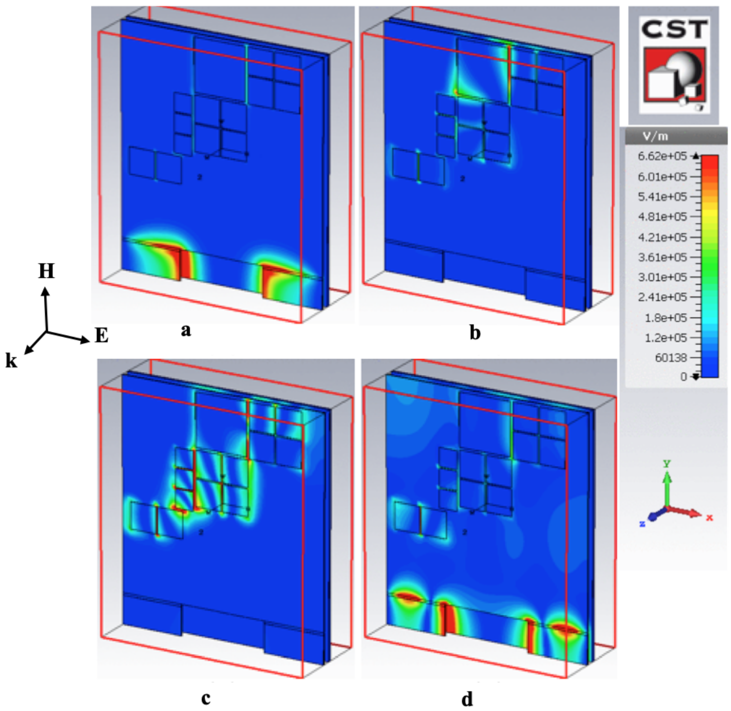

Figure 4.5. Distribution of electric field at (a) 0.63 THz, (b) 1.12 THz, (c) 1.48 THz and (d)1.87. THz [126].

Electric field distributions corresponding to the resonant frequencies are shown in Figure 4.5. Larger patches are associated with smaller frequencies. Patches with 100 μm side lengths excites resonance at 0.63 THz, 86 μm patch excites resonance at 1.12 THz, 43 μm patches and their interactions with 30 μm patches excite resonance at 1.48 THz (see Figure 4.5 (c)). The rectangular patches also excite another resonance at 1.87 THz. The absorber characteristics are different when the electric field is along the x-axis (see Figure 4.4), since the absorber includes two rectangular patches. The resonant frequency of a specific patch element is proportional to the reciprocal of the side length of the patch [127]. So, the electric field orientation determines the effective side length of a rectangular patch. There must be higher resonance modes, which we have not brought here as we consider the frequency band of 0-2 THz.

We introduced another design shown in Figure 4.6(a). We obtained this design by filling the empty spaces of the design shown in Figure 4.4 with different patches. The design includes square patches with side lengths of 15, 20, 25, 30, 43, and 86 μm and two rectangular patches with a size of 100$\times$43μm.

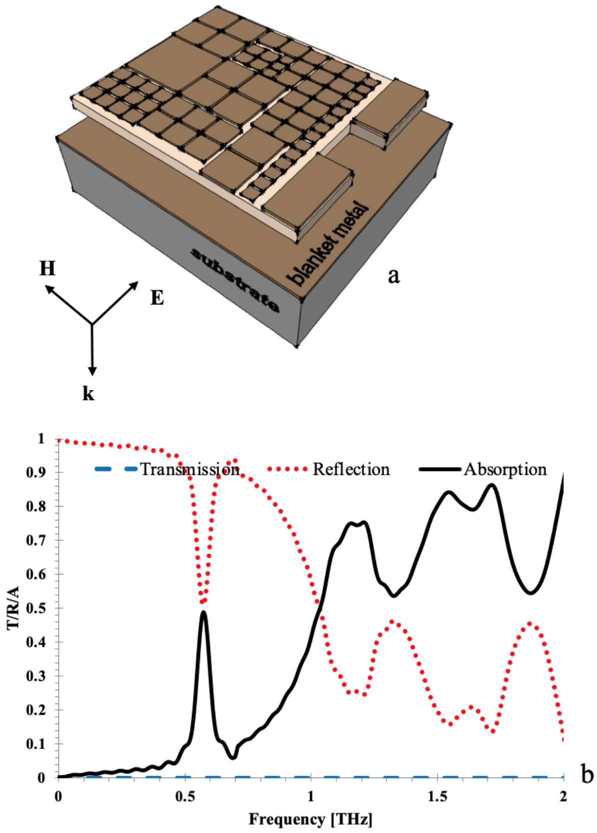

Figure 4.6. (a) Three-dimensional drawing of a metamaterial-based terahertz absorber with square patches with side lengths of 15, 20, 25, 30, 43, 86 μm and two rectangular patches with a size of 100x43 μm. (b) Simulated transmission, reflection, and absorption spectra of the absorber.

Metallic patches with different sizes are laid out on a single Parylene film anchored to the substrate through a set of suspensions. The absorption spectrum presented in Figure 4.6(b) indicates distinct resonances in a band of 0.3-2 THz. We realized a broadband absorber in this design by combining patches with different sizes. The device exhibits significant absorption in the frequency band of 1-2 THz due to the resonances of individual patches and the interactions between patches. This configuration is desirable for terahertz detectors that require detector structures isolated from their substrate. The metamaterial behavior is observed for unit cells, including the metallic patches on top, blanket metal on the substrate, and the Parylene and air spacing in between. Transmission is guaranteed to be zero with the presence of the thin blanket metal underneath the patches. In contrast, reflection from the device diminishes at certain frequencies set by the square patches' geometry, resulting in increased absorption at those frequencies.

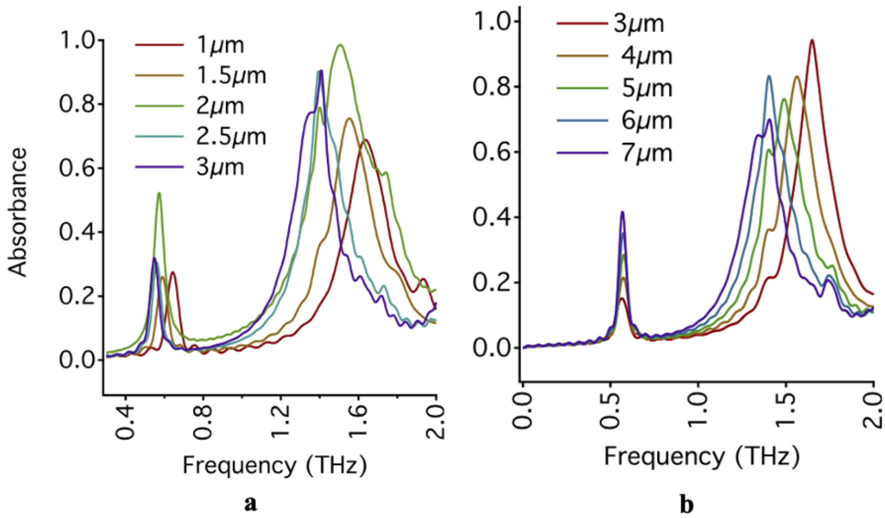

Figure 4.7. The variation of the resonance characteristics of the structure in Figure 4.3 as a function of (a) thickness of the Parylene layer, (b) gap height at the tip of the structure [126].

The resonant frequency of the device is also determined by the effective relative permittivity of the structure. So, the thickness of the Parylene layer influences the resonance characteristics. Figure 4.7(a) shows the distribution of the resonance peaks concerning the changes in the Parylene layer's thickness. The structure's effective permittivity increases with the thickness of the dielectric layer (For the sample in Figure 4.3). This results in a decrease in the resonant frequency of the device, as expected). During the operation of the device, the freestanding structure will be tilted with respect to its substrate. We analyzed the dependency of the resonator behavior by introducing a tilt angle. The position of the edge of the structure where we place the rectangular patches is kept stationary, and the freestanding structure is tilted about the y-axis (Figure 4.4). We varied the gap at the tip of the structure between 3 and 7 μm and observed the resonance characteristics shown in Figure 4.7(b). The resonant frequency of the structure excited by the rectangular patches keeps the same value at 0.59 THz since the effective gap change along the rectangular patches is minimal. However, the resonant frequency related to the array of the square patches decreases with the increasing gap.

To determine the effect of thickness of air gap beneath Parylene layer on absorption, the structure in sample Figure 4.4 was simulated with various thicknesses of air gap ranging from 2.5 μm up to 10 μm while keeping the rest of the dimensions the same.

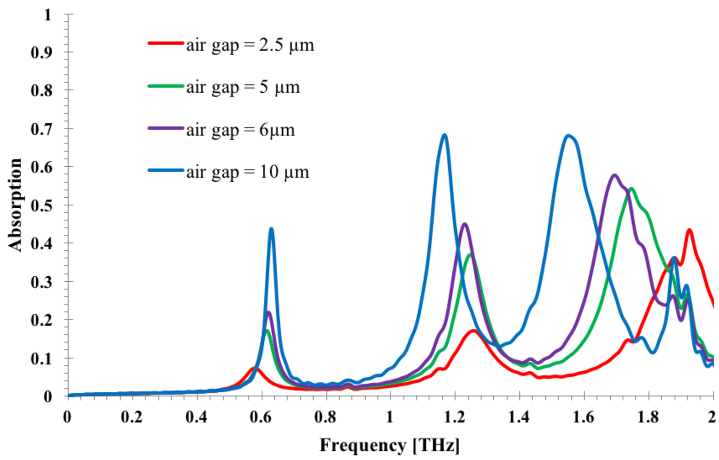

Figure 4.8. FDTD simulation (sample Figure 4.4) for changing air gap thickness from 2.5 μm up to 10 μm

It is clear from Figure 4.8 that the resonant frequency stays constant in the leg part as there is no movement at this point. As the thickness of the air spacer layer is increased, note that in resonance corresponding to larger patch size (1.2 THz), a slight red shift (0.1 THz) of the absorption spectra was observed for thicker air layers due to the increase in the effective overlapped area formed by patch and blanket metal and changes in effective permittivity in spacer region. This variation is much more for higher resonance (1.87 THz). It is 0.4 THz as the interaction and coupling between different patches in this resonance are more complicated, making the calculation of effective length and effective permittivity difficult.

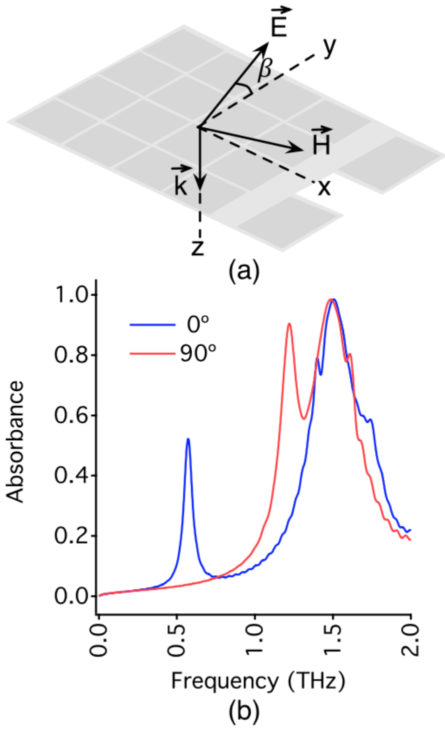

Figure 4.9. The dependency of the resonance characteristics of the structure with respect to the electric field orientation. (a) Variation of the angle between the electric field vector and the y-axis. The electric field and the magnetic field vectors are in the plane of xy. (b) The absorbance of the structure with different values of β [126].

The length of the patches along which the electric field is aligned determines the structure's resonant frequency. Thus, the resonant frequency is ideally the same for the electric field vector aligned along the x-axis or y-axis since the basic structure is a square. We analyzed the dependency of the resonator characteristics concerning the polarization shown in Figure 4.9(a). The field was kept perpendicular to the device along the z-axis, and we varied the angle β between the electric field vector and the y-axis. The absorption spectra for $\beta = 0°$ and $\beta = 90°$ are shown in Figure 4.9(b).

The resonant frequency of the structure at 1.49 THz due to the square patches is not altered. However, the resonance at 0.59 THz due to the rectangle patches disappears for $\beta = 90°$ since the electric field is no more aligned along the larger side of the rectangular patches, a resonance in higher frequencies have been excited corresponding to the smaller side length. On the other hand, another resonance at 1.2 THz is observed for $\beta = 90°$ due to the interaction between the rectangular and square patches at that frequency.

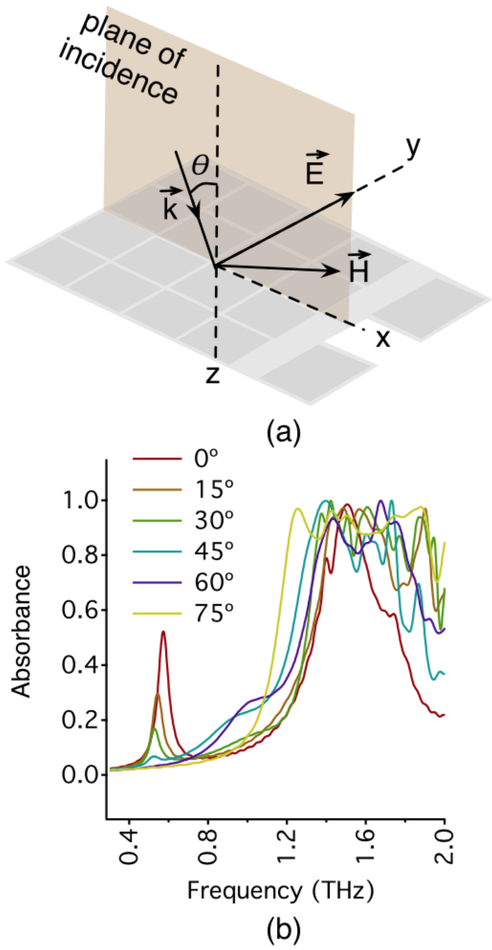

Figure 4.10. The dependency of the resonance characteristics of the structure with respect to the incidence angle. (a) The plane of incidence and the angle between the propagation vector and the z-axis is shown. The orientation of the electric field is stationary and is along the y-axis. (b) The dependency of the structure's resonance characteristics with respect to the changes of the angle θ [126].

Since the electric field vector mainly determines the resonance along the edge of a square or a rectangular patch, the incidence angle should have a minor influence on the resonance behavior as long as the orientation of the electric field vector is kept the same. We analyzed the influence of the incidence angle for TE mode as shown in Figure 4.10 (a) by varying the angle θ between the incoming beam and the z-axis. The absorption spectra of the structure for various angles of θ are shown in Figure 4.10(b). The structure performs well as an absorber even for large incidence angles for TE mode, as expected. By increasing the angle between the incident wave and normal to the absorber's surface, the resonance coming from the rectangle patch disappeared. This configuration has been demonstrated as a polarization-insensitive and omnidirectional THz absorber.

4.4. Microfabrication of Detectors

We designed the absorbers with a size of 200×200 μm and 270×250 μm so that it adequately intercepts the incoming THz flux at a band of 0.5-2 THz. The thickness of the titanium layer is 200 nm. The absorber is located on the movable mechanical structure made of a CVD-deposited layer of Parylene-C. The thickness of the Parylene layer is 2 μm. The structure is suspended over its substrate by two bi-material legs that deflect when exposed to thermal load. The length and the width of the bi-material legs are 45 μm by 75 μm and 43 μm by 100 μm for two sets of absorbers, respectively. The bi-material legs are connected to the substrate through the Parylene layer to isolate the detector structure from its substrate thermally. The length and the width of isolating legs are 5 μm and 75 μm, respectively. Parylene-C has very favorable thermomechanical properties for this application. The thermal conductivity of Parylene-C (0.08 W/m·K [128]) is extremely small. It can provide excellent thermal isolation without the need to extend the thermal isolation legs. Moreover, we can combine it with titanium for an efficient bi-material combination. The coefficient of thermal expansion of Parylene-C is 38 μm/m·K [129], whereas the coefficient of thermal expansion for titanium is 8.6 μm/m·K. We optimize the thicknesses of the titanium and Parylene layer for maximum thermally induced deflection. We fabricated the detectors using a simple microfabrication process with four photomasks. The microfabrication process steps are shown schematically in Figure 4.11. We started the process with a lift-off process to define a layer of 200 nm-thick Ti in the form of a diffraction grating (for optical readout purposes). Then, we spun a 5 m-thick photoresist layer and patterned it as a sacrificial layer, followed by deposition of a 2 μm-thick Parylene-C film. Next, we sputtered a secondary layer of Ti for both bi-material legs and the metamaterial absorbers. The latter Ti film's thickness is 200 nm to yield a thickness ratio of 10:1 between ParyleneC and Ti to maximize the thermally induced deflection. We employed HF wet etching for the definition of the metallic structures. Finally, we released the detector using acetone in a critical point dryer to eliminate the sticking problem.

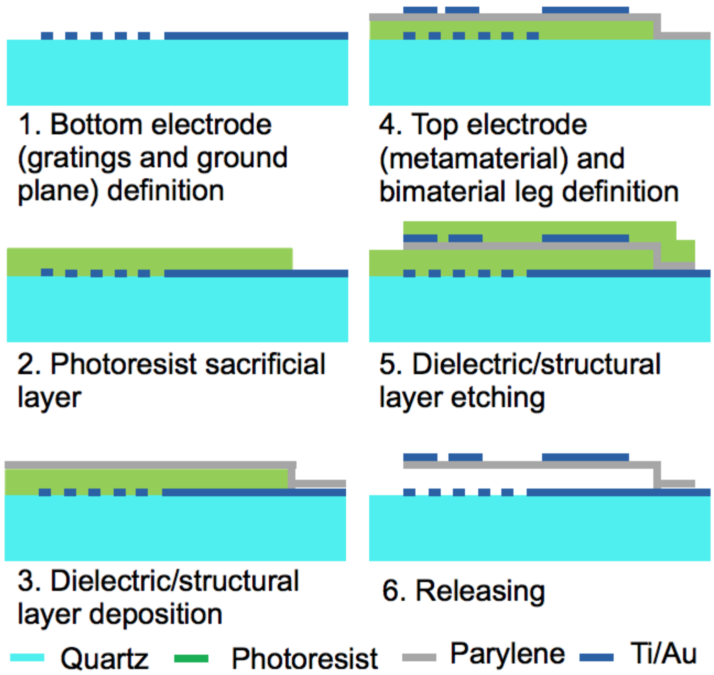

Figure 4.11. The process sequence of the microfabrication. Please note that the figure is not drawn to scale [127].

An SEM image of the fabricated samples in an array formation is shown in Figure 4.12. The Parylene layer is anchored to the substrate near the rectangular patches. The structure is connected to its substrates via legs that thermally isolate the structure and deflect in response to temperature differences induced by the absorbed radiation.

The detector substrate is quartz that allows optical access from the backside of the structure to enable optical interferometric readout. The Parylene layer also includes etching holes that help to remove the sacrificial layer underneath the structure during the releasing step using wet etching.

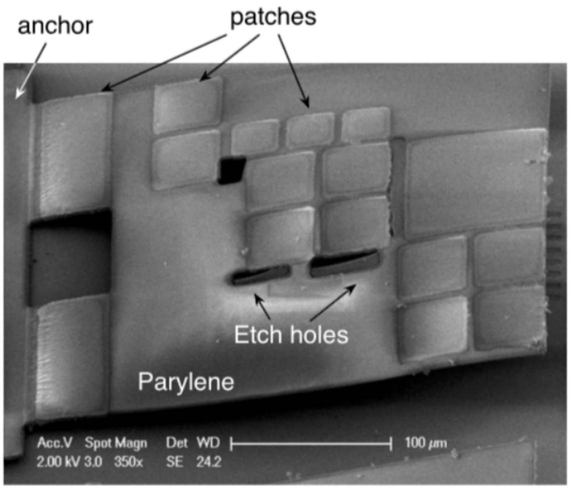

(a)

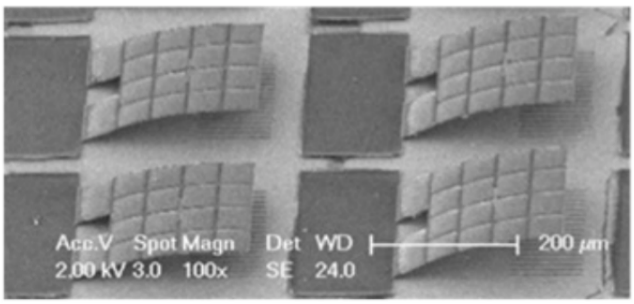

(b)

Figure 4.12. SEM image of a fabricated absorber. (a) absorber with different patch sizes [126]. (b) absorber with 43 μm patch in an array formation of 4×4 [127].

Figure 4.12(b) shows the suspended absorber that is 200×200 μm in size consists of 16 square patches of 43×43 μm, 2 bi-material legs of 75×45 μm, and the bottom metallic layer on the substrate consists of 18 gratings with a size of 5×94 μm, each.

4.5. Experimental Characterization

Measurements of the absorption characteristics of the fabricated detector have been done using a terahertz time-domain spectroscope (THz-TDS, TERA K15, Menlo Systems GmbH, Martinsried, Germany). After performing the reference measurements, we illuminated the whole array to obtain transmission and reflection spectra of the absorber. Absorption spectrum is calculated as Eq. 2.36. The results are shown in Figure 4.13 - Figure 4.17 for 5 different samples. We collected the data as the transmission reference when no sample was placed between the emitter and the receiver antennas of the spectrometer. Then we placed a thick metal reflector facing the antennas that were angled 90 to collect the reflectance reference.

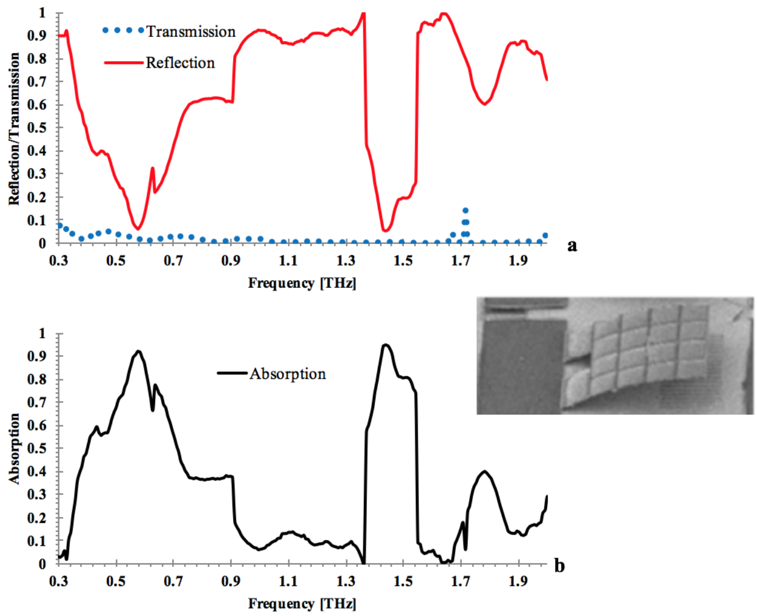

Figure 4.13. Measured spectra of (a) transmission, reflection, and (b) absorption characteristics of the absorber with 43 μm square patches (sample 1). The red line and dashed-blue present reflectance and transmittance, respectively, while the black line shows the absorbance [126].

The larger rectangular patches located on the bi-material legs excite an absorption resonance at 0.59 THz, while the smaller square patches excite another resonance at 1.47 THz. At resonance, the absorbance is almost 100%. We obtained an average absorbance value of 0.4 in a band of 0.5-2 THz using this design.

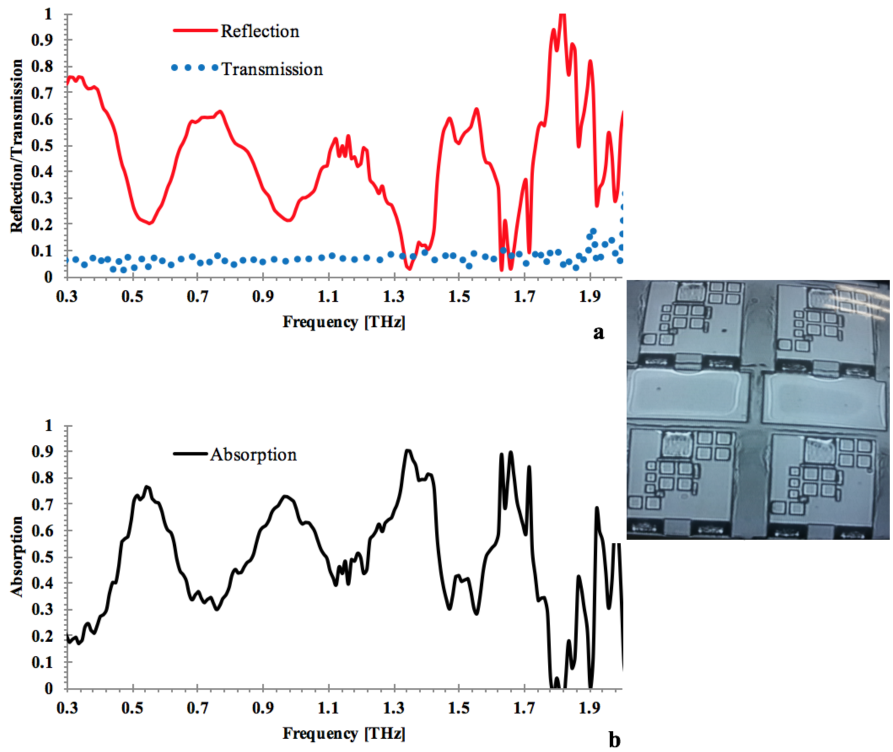

Figure 4.14. Measured spectra of (a) transmission, reflection, and (b) absorption characteristics of the absorber with 86 μm, 43 μm and 30μm patches (sample 2). The red line and dashed-blue present reflectance and transmittance, respectively, while the black line shows the absorbance [126].

The variety of patch sizes and their positions in sample 2, 3, and 4, as seen in insets of Figure 4.14- Figure 4.16, causes different absorption behavior. Sample 4 contains various sub-unit cell patches in dense format, thus overlapping resonances and a broad absorption band. The measured absorption peaks match well with the simulated peaks. The measured resonant frequencies in sample 2 exhibit red-shift concerning the simulation results. The largest deviation is observed with the first resonant frequency where the measured frequency is 20% smaller than the simulation results. We identify the error sources as the differences between the material properties we used for the simulations and the actual ones, the deviation of the incidence angle from the normal incidence angle case, and the deviation of the electric field's polarization. Nevertheless, the measurement results verify our findings in simulations.

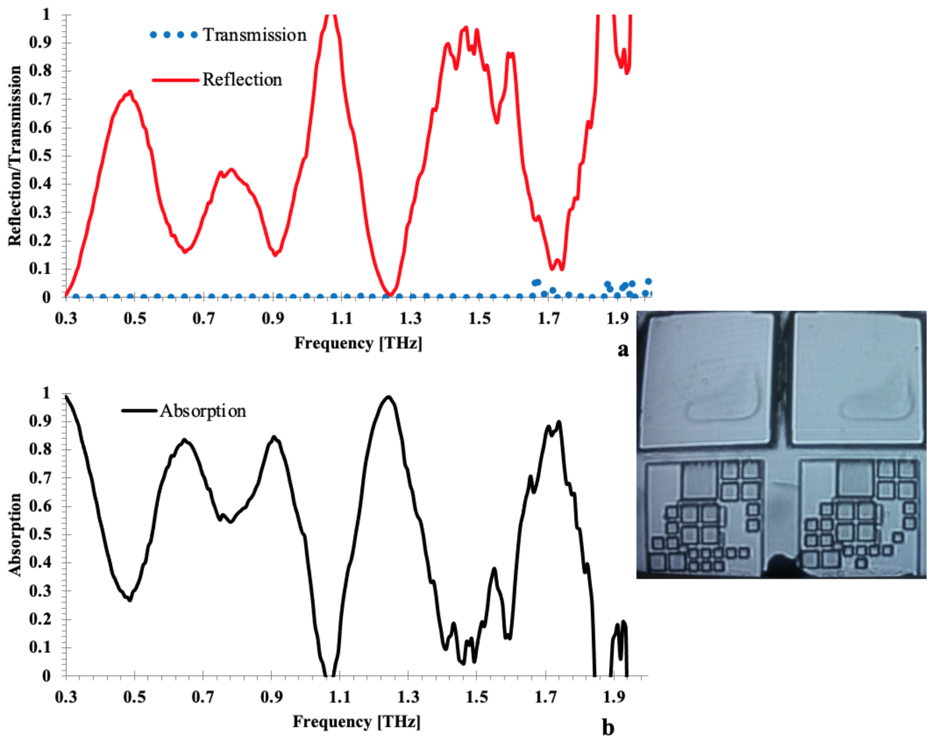

Figure 4.15. Measured spectra of (a) transmission, reflection and, (b) absorption characteristics of the absorber with 86 μm, 43 μm, 30μm and 20μm patches (sample 3). The red line and dashed-blue present reflectance and transmittance, respectively, while the black line shows the absorbance.

We fabricated another design shown in Figure 4.17. We obtained this design by filling the empty spaces of the design shown in Figure 4.12(a)(sample 2) with different patches. The design includes square patches with side lengths of 15, 20, 25, 30, 43, 86 μm and two rectangular patches with a size of 100×43 μm.

The absorption spectrum is shown in Figure 4.17(b) indicates distinct resonances

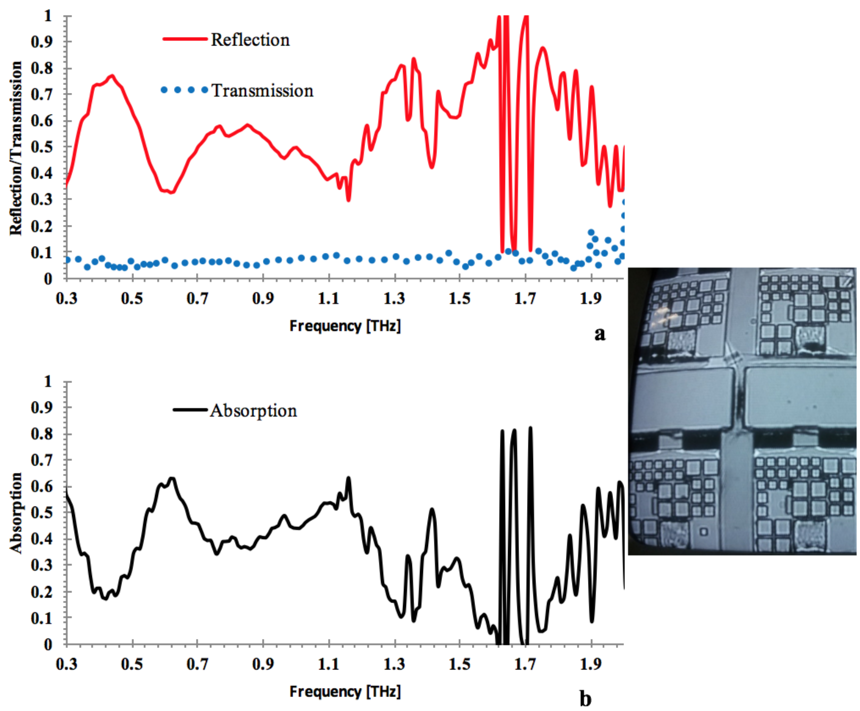

Figure 4.16. Measured spectra of (a) transmission, reflection and, (b) absorption characteristics of the absorber with 86 μm, 43 μm, 30μm, 25 μm and 20μm patches (sample 4). The red line and dashed-blue present reflectance and transmittance, respectively, while the black line shows the absorbance.

in a band of 0.3-2 THz. We realized a broadband absorber in this design by combining patches with different sizes. The device exhibits significant absorption in this band due to the resonances of individual patches and the interactions between patches. We measured zero transmission for this design in the designated band.

However, the transmission we measured for the device of Figure 4.14 (sample 2) is minimal but finite. The most significant difference between the two designs is the fill factor considering the patches on the device's surface. A significant portion of the device of Figure 4.14 does not include any patches, and the incoming radiation impinges on the Parylene surface, which is transparent. We realize the bottom electrode, which is

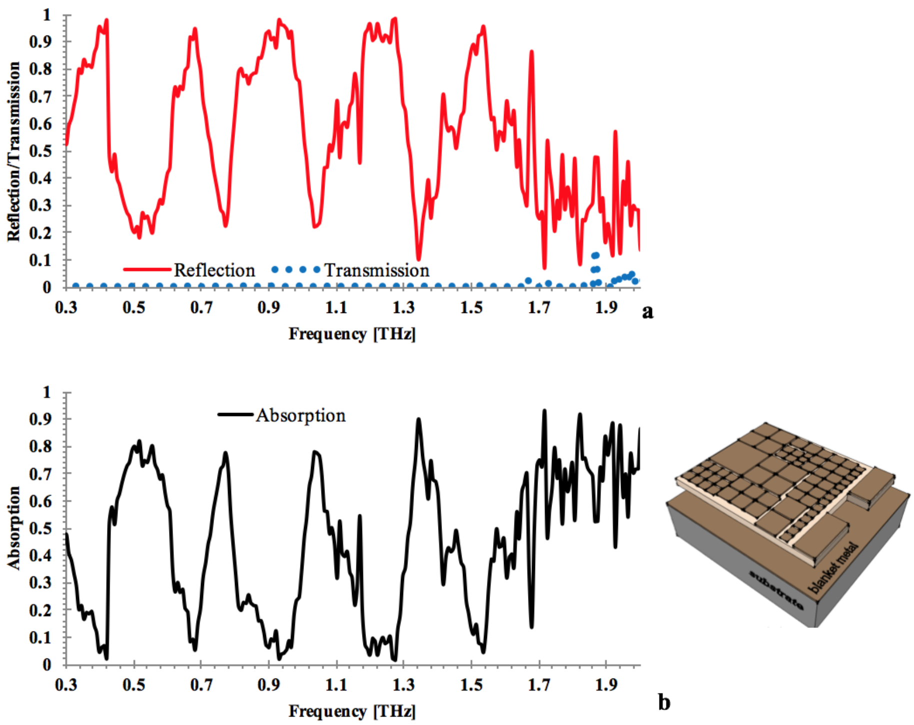

Figure 4.17. Measured spectra of (a) transmission, reflection and, (b) absorption characteristics of the absorber fully covered with 86 μm, 43 μm, 30μm, 25 μm and 20μm patches (sample 5). The red line and dashed-blue present reflectance and transmittance, respectively, while the black line shows the absorbance [126].

200 nm in thickness, transmits some of the power it receives, contrary to our simulation results. Nevertheless, the transmission is deficient (less than 10%) for the entire band for the bottom electrode.

The reference plate used in the experiments should ideally be a perfect reflector resulting in higher reflectivity than any other sample. This expectation may fail to be realized when the signal strength is inadequate. The inset to Figure 4.18 shows an example where the reflectivity of the reference plate can fall below the sample. In such instances, the normalization process can result in the reflected power from the sample above unity, which is not physically valid. Whenever this case arises, the reflectance values are clipped at unity in Figures 4.14, 4.15 and 4.16.

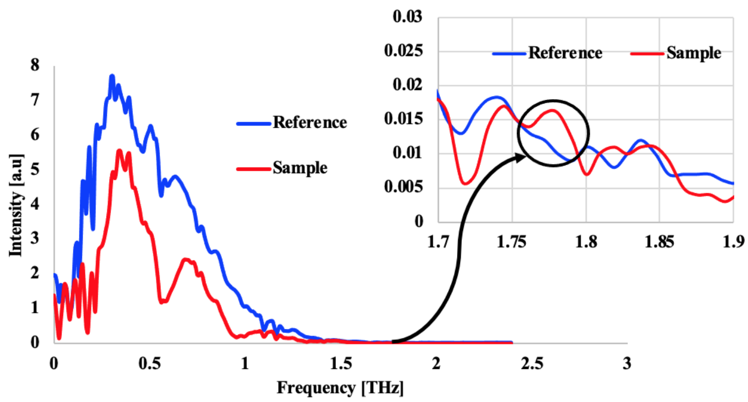

Figure 4.18. The reflectivity of the reference plate in comparison with a sample to explain the clipping.

4.6. Optical Interferometric Readout

We also built two experimental characterization setups based on optical lever detection and a diffraction grating interferometer under ambient conditions. Figure 4.19 shows the layout of the optical lever detection setup. We focused a laser beam (λ=635 nm) on an individual pixel structure using lenses L1, L2, and L3. We arranged the laser beam's spot size on the plane of the detector as 15 μm to ensure that the reflected beam was collected off of the mirror-like metamaterial patches. We used the last lens (L4) to focus the reflected beam on a segmented photodetector (PD). We also used a Peltier thermoelectric cooler (TEC) module with a temperature controller unit for the characterization of thermomechanical response.

Figure 4.20 showed the normalized deflections of two different pixels in comparison to a stationary reference on the chip when we swept the temperature between 18° and 40C. Temperature change results in approximately 5-times larger optical signals on the devices as compared to the reference point. Possible reasons for the shift in reference measurement include the change in the index of refraction due to temperature rise and the drift in the chip's position. Nevertheless, measuring a reference point allows us to implement a differential readout scheme to cancel the signal change due

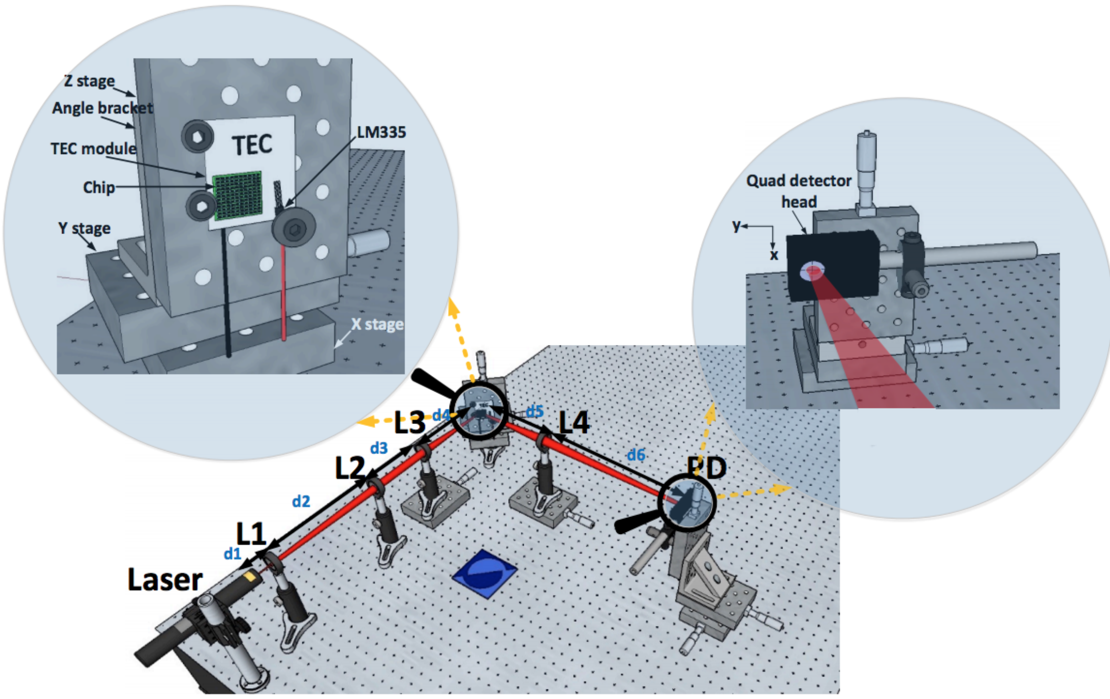

Figure 4.19. Three-dimensional drawing for the experimental characterization setup for the optical readout method [127].

to these.

The optical lever method can be effectively used to assess the displacement of the devices. Position sensitive photodetectors or knife-edge detection methods can be used with the optical lever method. However, only relative displacement can be measured in this method without proper calibration. In the second experimental setup, we implemented a diffraction grating interferometer to measure the absolute displacement of the devices. We again used the laser beam (λ=635 nm) and adjusted the spot size of the readout laser at the detector as 13 μm using lenses L1, L2, and L3 similar to the setup shown in Figure 4.19. We illuminated the diffraction gratings from the backside of the substrate. We placed a PD to capture the 1st diffraction order from the device to obtain the device's thermo-mechanical response. We heated the device directly using an external heat source. The output signal of the photodiode was amplified and directed to a scope and a spectrum analyzer. We monitored the photodiode signal during the

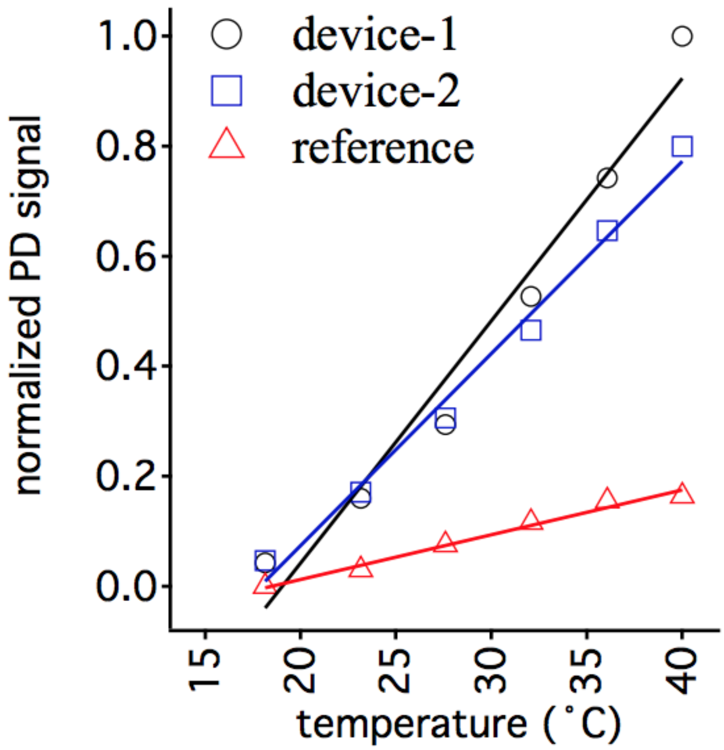

Figure 4.20. Measured photodiode signal using the optical lever method due to temperature difference imposed on the detectors [127].

heating and cooling cycles when the heater was on and off. Figure 4.21 shows the device's response due to temperature difference in the presence of the heater. The amplitude difference between a consecutive maximum and minimum corresponds to a displacement of $\lambda/4$. The voltage difference between the maximum and minimum values is 55.3 mV, as can be inferred from Figure 4.21.

We measured a 4K increase in the temperature of the chip using an external temperature sensor at the end of the heating cycle, during which we observed 4.5 periods of cycles. Each period of cycles corresponds to a displacement of $\lambda/2$. Half of the period for one of the cycles is shown in Figure 4.21(b) to assess the PD signal change as a temperature function. The maximum slope of the fitted function estimates the device's responsivity, and we calculate a responsivity of 193 mV/K. We also measured the noise spectrum of the device in the frequency range of 0-50 kHz using a spectrum

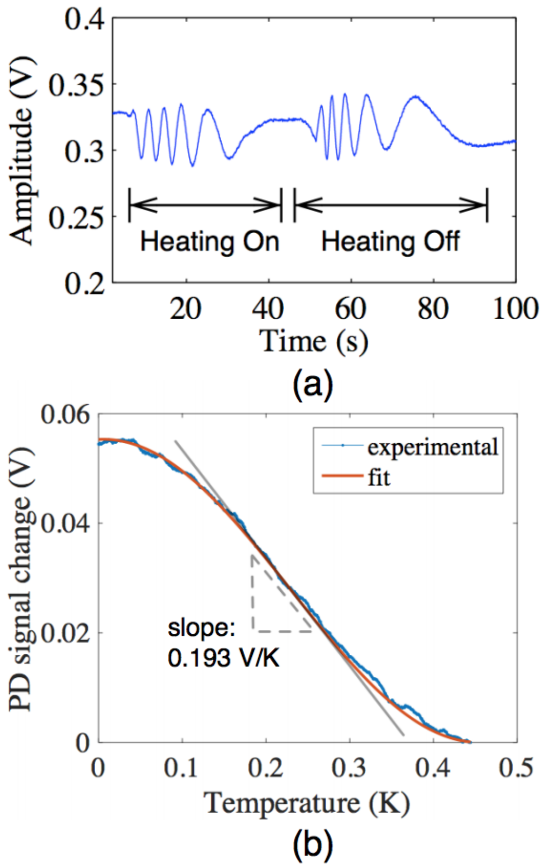

Figure 4.21. (a) Measured photodetector signal at the 1st diffraction order in response to an external heater heating the detector's chip. (b) Change in the photodetector signal as a function of temperature difference at the detector [127].

analyzer monitoring the PD signal. Figure 4.22 shows the power spectral density of the 1st diffraction order in the range of 36-50 kHz when the detector is not exposed to any external stimuli. The resonant frequency of the device at 45 kHz is visible in Figure 4.22 due to the detector's thermal noise. Besides, the device's noise spectrum exhibits spurious sharp peaks due to the external electrical components that affect the measurement. The power spectral density of the device for frequencies below 1 kHz is $3.5\text{x}10^{-7}$ V/Hz. This value corresponds to a total integrated noise level of 35 μK within a detection bandwidth of 380 Hz, corresponding to the frame rate that we calculate for the detector in ambient conditions. The integrated noise level reduces to 8 μK for a frame rate of 20 Hz, corresponding to the value we calculate for the detector at 1 mTorr. The projected NETD value based on the experimentally obtained temperature noise at the detector is calculated as 144 mK for the detector at 1 mTorr.

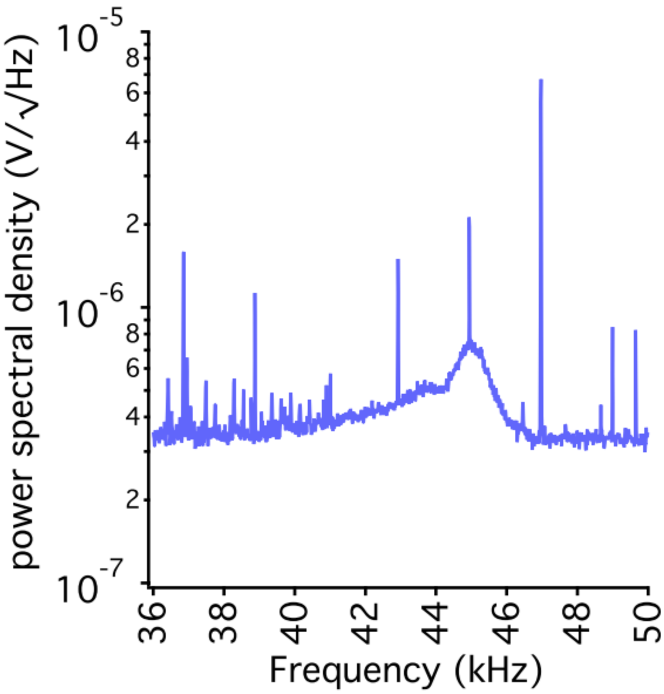

Figure 4.22. Measured power spectral density of the device for setup 2. The resonant frequency of the device due to the thermal noise of the detector is 45 kHz [127].

We demonstrated the ability to integrate highly absorbing metamaterial films into bi-material sensors. The study showed that this combined configuration has great potential in THz sensing and imaging. In detail, we report the design, fabrication, and characterization of highly sensitive micromechanical bi-material THz detectors based on metamaterial structures. Initial work on imaging of a THz-QCL beam using a detector array is also included.

5. Three Dimensional Porous Metamaterial based THz Absorber

5.1. Overview

Although researchers have considered several 1 and 2 dimensional MM absorbers because of the simplicity of fabrication and reduced design complexity, 3D structures can exploit the full potential of the metamaterial concept in reality. A 3D structure has a wider surface area within the same unit cell compared to the structure in 2 dimensions. [130]. This wide area increases the chance of a strike of the incoming EM wave. 3D MM lens antennas achieve the ability to form images at extensive angles compared to conventional 2D ones [131]. Through transforming a 2D resistive metamaterial absorber structure to 3D, absorption performance has been optimized more than 90 % in the range of 8.3-40GHz under normal incidence [132]. General strategies for extending the absorbing bandwidth of THz MM absorbers, such as combining multiple sub-wavelength structures with different sizes or stacking vertically metal-dielectric layers, will make the unit cells too large. Larg unit cells will result in increasing angular dependency. Besides, due to the limited number of multi-size cells, the extension of bandwidth is limited. Stacking metal-dielectric layers expand the absorption bandwidth; however, the stacking method is usually restricted because of fabrication complexity and cost as strict processing and accurate machining are required [133]. Additionally, the thickness will be considerable. Therefore, the design and characterization of simple and high-performance THz MM absorbers is still a significant issue in MMs. It is advantageous to design a multi-band or broadband MM absorber by overlapping the fundamental and high-order resonance modes in a single patterned absorber structure. Overlapping multiple absorption modes satisfies a strong broadband absorption, which can be realized by defining the third dimension into a unit cell. 3-dimensional structures have multi-mode cavities that can be controlled to obtain the desired performance [134, 135]. Recent work by Shen et al. [136] proposed a 3D MM absorber using the stand-up resistive patch arrays, shows a broadband 3D absorber in GHz frequencies. 3D chiral metamaterials that mix electrical and magnetic responses are of particular interest here. Wang et al. used a 3D array of chiral SRRs to fabricate 3D isotropic chiral metamaterials [137]. Uni-axial metamaterial composed of 3D gold helices combine internal and Bragg resonances leading to a broadband response in mid-infrared frequencies [138]. Another work reported the transmission of EM fields within periodic holey-structures as a metamaterial lens and their inherent utilization for ultrasonic imaging and deep sub-wavelength resolution [139]. A periodic 3D porous metamaterial seems to be an assuring alternative to manage wave propagation at specific frequencies. Transmission or reflection of EM wave inside the features (such as holes or channels) of these periodic structures happen due to Fabry-Perot resonances [139]. Photonic crystals, precisely inverse opals (IO), can form three-dimensional porous structures. Photonic crystals (PhC) have a periodic inequality in the dielectric function that affects the propagation of photons; much like semiconductor influences the flow of electrons, a PhC affects the flow of photons. As a consequence of the different dielectric media and the refractive index variation within the crystal, light is scattered and/or diffracted from the various surfaces, causing a band of forbidden frequencies where scattered waves interfere destructively in all directions. Light propagation is prevented inside this range. One of the more popular methods of photonic crystals is the generation of artificial opals by the self-assembly of colloidal spheres of either silica or various polymers [140]. The infiltration of artificial opals with a material of high refractive index and following removal of the spheres by chemical etching to produce a structure of periodic holes (air voids) encircled by a continuously interconnected material forms IOs. This interconnected material creates a considerable refractive index variation that has the potential to produce a full band-gap [140]. Thus the absorption peaks and resonances can be tuned by changing geometrical parameters such as the filling fraction and sizes of spherical voids and lattice constant. Recent research shows that honeycombs and their composite structures as 3D metamaterial have significant benefits on electromagnetic absorption properties in radar [141] and microwave frequencies [142]. In this Chapter, inspired by the performances mentioned earlier, the 3D porous MM based absorbers are introduced in THz frequencies. The structure is made of CoNi alloy on a standard metal-dielectric layer. We studied the

EM responses of 3D MM absorber in 0.3 - 2 THz band. Controlling and optimizing the dimensions of the pores, and thicknesses, in the structure will aid in obtaining the multi-band absorbers and broaden the working frequency band. A design expanded to the third dimension brings new resonance peaks. Hence an out-of-plane length gives us the adaptability to control the incoming beam and polarization direction and optimize the structure for different incident beam and polarization angles. The third dimension allows the creation of resonant structures independent of an oblique EM wave angle, especially for larger angles. Furthermore, fabrication of the structure can be done using a simple standard photolithography technique and does not demand high-tech processes.

A brief introduction about Co, Ni, and their alloys will help understand the inclusive attraction they have received in many research areas as high-efficiency wave-absorbing materials. They have excellent magnetic [143, 144], and optical [145] properties. They have been applicable as highly efficient absorbing materials with light weights, low thicknesses, strong absorptions, and wide-frequency bandwidths [146]. Such materials get attraction in fields including data storages [147], microelectronic devices [148], medical diagnosis [149], and microwave absorption [150, 151]. A recent work by Sun group [146] showed that compositing of graphene with magnetic inorganic nanoclusters (e.g., Ni, Co, LiFeXOY, and FeNi3) could significantly enhance their microwave-absorbing performance. Recently, Cao et al. reported that CoNi alloy nanoparticles with an average size of almost 12 nm anchored on a spherical carbon monolith exhibited improved microwave absorption properties [144]. Boi et al. reported an enhanced saturation magnetization in buckypaper-films of thin-walled carbon nanostructures filled with CoNi, Co, and Ni crystals [152]. Such properties would be beneficial for designing EM wave absorbing structures made of Co/Ni alloys. Here, we reported two different types of 3D CoNi absorbers. The designs exhibit excellent THz absorptivity.

5.2. 3D MM based Absorber Design and Simulations

In this part, we employ two design schemes for the 3D MM based THz absorber; the first is introducing the third dimension to the patch absorber and forming a cubic absorber. We will propose an out-of-plane porous absorber inspired by a cubic absorber in the following.

5.2.1. Cubic MM Based THz Absorber

In this work, we present our approach to modeling 3D MM absorber in the THz regime. We discuss our model towards developing a 3D design and analyzing reflection, transmission, and absorption spectra. Figure 5.1(a) depicts 3D structure of a cubic absorber. The patch on substrate gets the third aspect as it confirms its name, a "three-dimensional" absorber. Apart from a better understanding of the effects that govern such materials' behavior, our aim in this design is to find new unit-cell structures that could advance the MM absorber research field in the THz range.

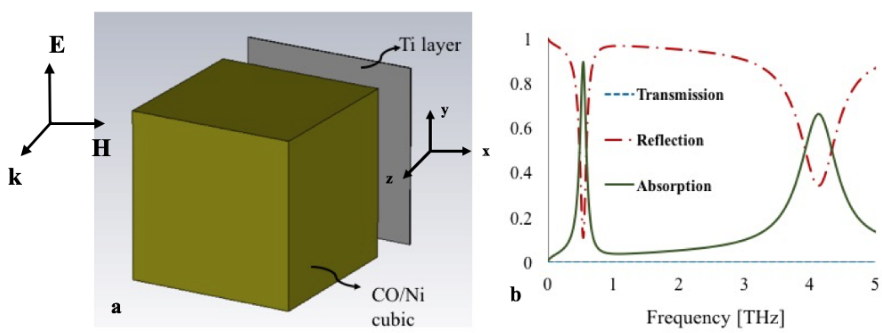

Figure 5.1. (a) Schematic of a cubic MM absorber, (b) Simulated transmission, reflection, and absorption spectra.

The cubic is made of Co/Ni alloy. The electrical resistivity of a specific type of Co/Ni alloy (Elgiloy) is too small, 0.0000996 ohm.cm [153]. A layer of blanket titanium, making transmission zero, is placed on a silicon substrate. The silicon substrate has not been presented to simplify the model. In this case, we canceled the air gap and mechanical (Parylene) layers. The side length of the cubic is 27 μm. The unit-cell structure of the MM is periodic along the $\tilde{x}$- and $\tilde{y}$- axes. We are interested in a frequency range of 1-5 THz. The back-plate metallic layer is made of a Ti film with a thickness of 0.2 μm, larger than the Ti's skin depth in the terahertz regime. Boundary condition consists of perfect magnetic conductance (PMC), and perfect electric conductance (PEC) for a unit cell is considered. E-field is along $\tilde{y}$ direction and H-field is along $\tilde{x}$ direction. Excitation ports are perpendicular and aligned with the $\tilde{z}$-axis. Reflection, transmission, and absorption spectra are simulated as shown in Figure 5.1(b). One can realize perfect absorption of the proposed MM absorber in THz frequency range, as the impedance matched to that of free space at resonances, and stronger absorption observed. Fundamental resonance happens at 0.54 THz. Note that for achieving this resonant frequency with square patch design, we need a patch with almost 100 μm side length size. Higher-order resonance takes place at 4.14 THz.

To explain the absorption mechanism of the recommended MM absorber, the electric field and surface current distributions of the unit-cell structure at resonant frequencies of 0.54 THz and 4.14 THz presented in Figure 5.2. The electric field mainly concentrated on the upper and lower faces normal to the electric field direction. There is a circulating current around the cubic corresponding to the resonant frequency. The H-field is perpendicular to the plane of surface current, confirming a magnetic resonance. As comes from Figure 5.2 (a), at 0.54 THz, the induced current in the backplate metal is in the opposite direction of one in the cubic surface. The current loops are formed by antiparallel currents satisfying magnetic responses. Figure 5.2(d) shows that for the second resonant frequency (f= 4.14 THz), the electric field distribution is mainly concentrated on the edges of upper and lower areas of the cubic structure, as we have seen in square patch cases. Excitation of boundaries causes a response as half-wave resonant mode [154], strongly coupled to the external electric field. Essentially, the higher-order mode responses are occurring at the higher frequencies since the dimension of the cubic structure is larger than the multiple of a half-wavelength of the resonant modes. The H field distributions are depicted in Figure 5.2(e,f) at 0.54 THz and 4.14 THz, respectively, to understand the magnetic coupling. The coupling between cubic and lower metallic plate cause anti-parallel circulating current among them (magnetic coupling).

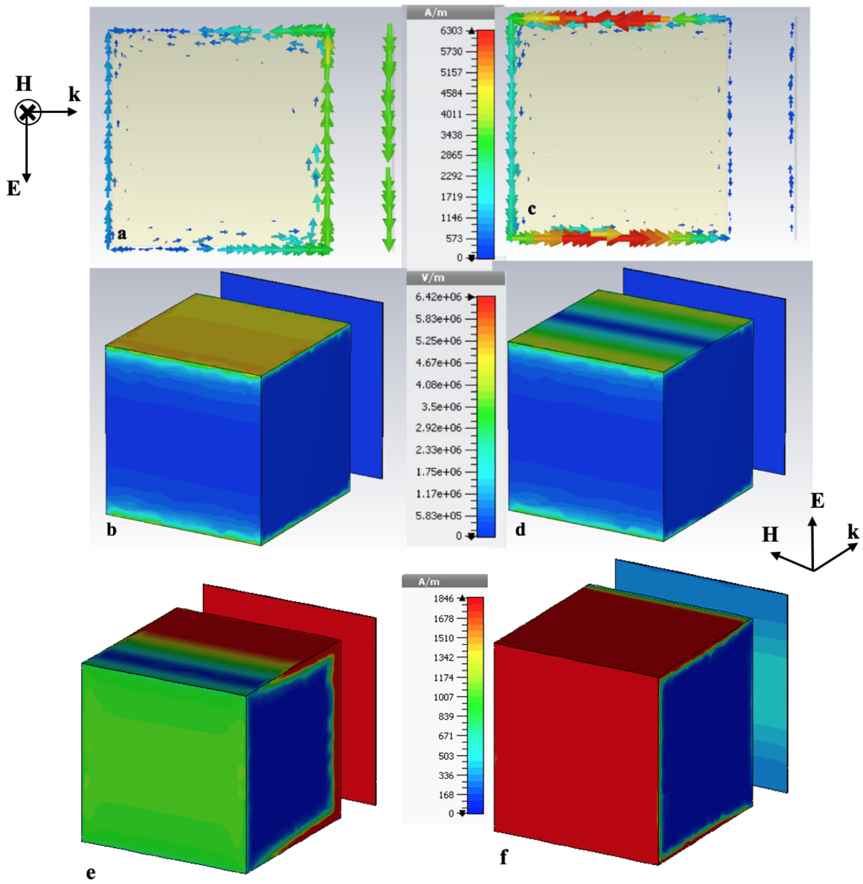

Figure 5.2. (a,c) Distributions of surface current at the upper and lower layer, and (b,d) electric field distributions of the proposed MM absorber's unit-cell. (a, b) f = 0.54 THz, (c, d) f = 4.14 THz. H field distribution (e) 0.54 THz, (f) 4.14 THz. The solid arrow indicates the current flow direction.

As we mentioned earlier, Co/Ni alloy has very small electrical resistivity that means large conductivity, σ. Consider the complex permittivity $\tilde{\epsilon}$ formula defined as Eq 5.1. The imaginary part of complex permittivity characterizes the conduction properties of a medium. Rewriting the Drude model as Eq 5.2 determines that the real part of $\tilde{\epsilon}$ for metals is negative below plasma frequency. Consequently, any electrical field can not penetrate the media, meaning the metallic layer reflects the electromagnetic wave in these frequencies,

$$\tilde{\epsilon} = \epsilon' \left(1 - i\frac{\sigma}{\omega\epsilon'}\right) = \epsilon' - i\frac{\sigma}{\omega}, \tag{5.1}$$

$$\epsilon'(\omega) = 1 - \frac{\omega_p^2}{\omega^2 + \Gamma^2}. \tag{5.2}$$

Current favors to pass along the surface in higher frequencies, providing surface current. The equation for skin depth, δ, is brought as

$$\delta = \sqrt{\frac{2}{\sigma\omega\mu}}. \tag{5.3}$$

As shown in Figure 5.2 (a, c) current concentrates near to the surface. The high conductivity prevents any meaningful penetration at the material. We can consider current flows in patch films with a thickness of δ and length of cubic side length because of the slight conductive depth in each cubic face. The cubic's side length along which the electric field is aligned determines the structure's resonant frequency. The current is circulating in a way that surrounds the cubic. As comes from Figure 5.2 (a) the current path length is 4 times of side length which is $4 \times 31 = 124\mu m$. The corresponding resonance for this size is in a good match with our results in Chapter 3, which confirms the dependency of the resonant frequency of square patches as a function of side lengths summarized in Figure 3.11 (b). Electric filed distribution for second resonance at 4.14 THz shows the polarization of faces of the cubic, therefore the electric dipole resonance under E-field drive. The aimed resonance with patch square ones would achieve by larger patch sizes for 0.54 THz (almost 125 μm) or a minimal size (nearly 5 μm) for 4.14 THz one. Introducing the third feature to patterned media makes it compact.

5.2.2. 3D Porous MM Based THz Absorber

Metals are extremely reflective for electromagnetic waves, particularly at far-infrared and terahertz frequencies. Chapter 4 shows that impedance matching of layered metallic structure (patches) makes reflectively zero in specific frequency bands. Vorobyev and Guo have developed another technique to transform highly reflective metals to either absorptive or reflecting just some part of EM wave named as femtosecond laser ablation, forming the so-called black and colored metals [155, 156]. Recently, a work enhanced the absorptance for metals at terahertz frequencies. The research shows various lateral channels provided on metal exteriors can effectively couple free-space radiation to terahertz "surface plasmon polaritons", SPPs [157]. The absorbers proposed in this part utilizes porous design based on inverse opal structures to obtain perfect absorber in THz frequencies out of metallic alloy material.

5.2.3. Modeling and Mathematical Interpretation of 3D porous MM Absorber in THz Regime

A 3D metamaterial such as cubic studied in the previous section has some problems to solve. Bulkily properties make it heavy for fast responding application. Mechanical structures may not be able to move such a massive cubic. Secondly, the side length of the cubic is the only parameter that defines the resonant frequency. Optimization of the side length size adjusts the absorption band to different frequency regions. Porosity reduces the mass of the absorber. On another point, the porous structure has a small heat capacitance. Thus fast-responding absorbers can be developed by reducing the thermal mass [158]. Moreover, the geometry, porosity, number of porous layers, and pore size of the structures determine the spectral bandwidth of absorption [159]. Adjusting the geometrical properties is a crucial point to tune the spectral bands of absorbers for various applications. Moreover, incident electromagnetic radiation can be trapped in optical cavities formed by engineered structures. Porous structures in the form of metal blacks have been demonstrated as efficient infrared absorbers [158]. Porous structure leads to diffraction of EM waves. If an EM wave is incident on such construction, some wavelengths are forbidden from passing through the material; instead, they are reflected. However, some of the reflected beams will be trapped in pores. The remaining wavelengths are unaffected by the porous structure, and they pass through. The essential aim here is to prevent transferring the EM wave out of the absorber. Like patch MM absorber design, a blank metallic layer on substrate blocks the transmission of EM waves. Metals with porous surface layers exhibited higher efficiencies of light absorption over a wide wavelength range than those with mirror-polished surfaces due to multiple reflections of incoming light and multiple light absorption on the metal surface [160]. Porous metal surface helps to minimize the reflection of an incident wave. Various porous structures can be introduced by size, shape, volume, and pitch of the pores. For example, [161] provide the cloverleaf shape pore. Porous absorbing material can also be granular [162]. In this section, porous

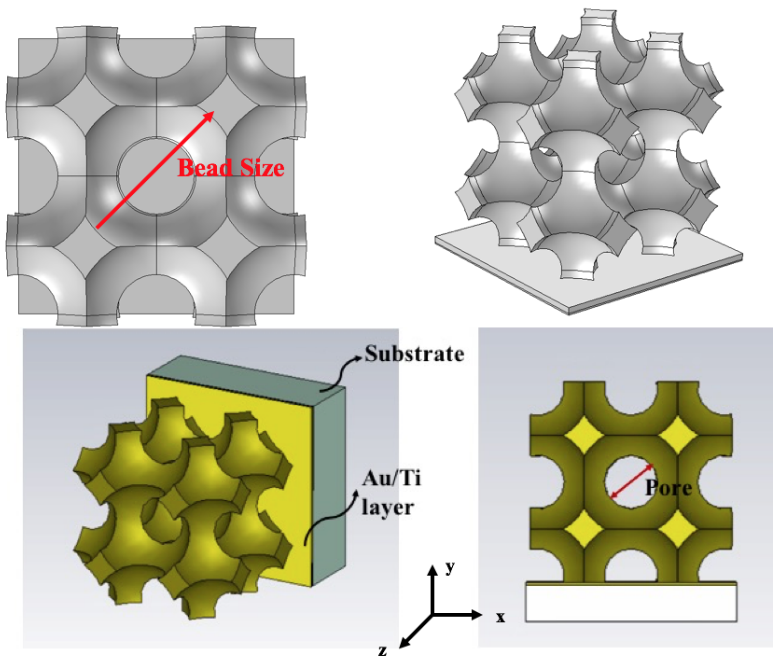

Figure 5.3. Computational model of the porous absorber. The insets show the structure from the top and side.

honeycomb-like composites will be introduced, consisting of a regular arrangement of spherical void spaces surrounded by solid walls as shown in Figure 5.3. The structure consists of a cubic that spheres and cylinders with a radius of R_s and r_s respectively, subtracted in every face of the cubic. The spheres, as we called them beads, incorporate the periodicity of pores. The arrangement and spacing among beads identify the pore size. We will show that with an accurate selection of sizes, resonance will happen in THz frequencies.

5.2.3.1. Modeling Based on Interference Theory . Here we assume the interference method to investigate the absorption mechanism of the porous MM. As shown in Figure 5.4 (a), the incident waves to the structure encounter multiple transmissions and reflections. Various possibilities for the incident beam to happen are reflection (marked as R), transmission through the pore (marked as T), and diffraction from edges (marked as D). The porous MM interference model comprises two interfaces.

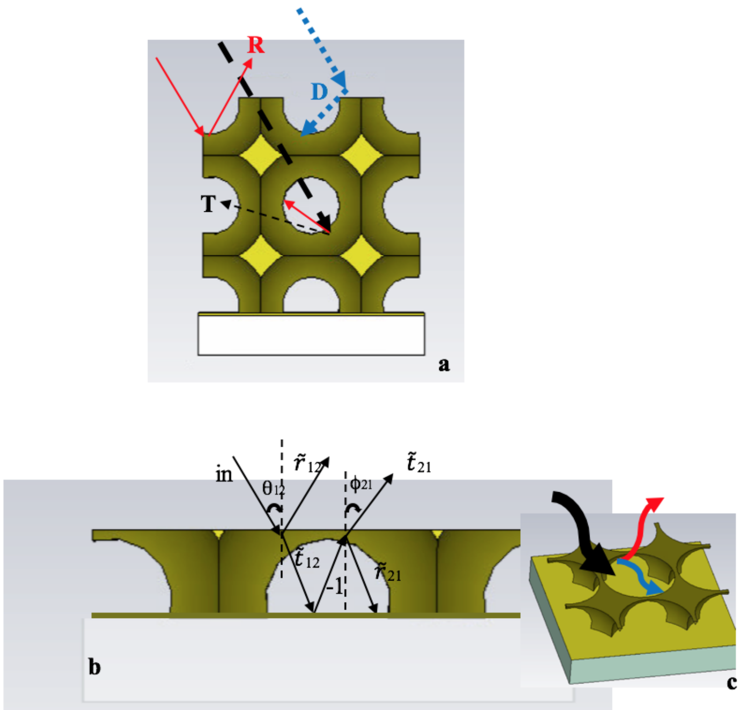

Figure 5.4. Interference model of the porous metamaterial absorber, (a) various possibilities for incident beam, reflection (red-line), transmission through the pore (black-dashed), diffraction (blue-dashed), (b), and (c) multiple reflection model for 1/4 layer MM absorber

The top interface consists of a hole (pore) surrounded by thin walls, and the next porous layer's walls are the bottom interface. Both interfaces are treated as two non-thickness surfaces. Note that some portion of EM wave transmits through the pore in the first layer. In this part, the transmitted beam may continue its way among another pore to below or side layers, either may hit a wall and be reflected. Thus, based on interference theory, the porous MM absorber can be considered as a Fabry-Perot-like resonance cavity [163]. The cavity causes multiple interference effects in the form of multi reflection for the incident EM waves, eventually raising the high-level absorption. Multiple reflections are superpositioned, then destructively interfere with the air interface's direct reflection, reducing the total amount of reflected beam. Aside from the refraction modes, the EM wave incident to the pores' edges will be diffracted, increasing the chance of trapping the EM beam inside the structure. For simplicity we consider 1/4 layer of proposed design as shown in Figure 5.4 (b,c). The walls work as the surfaces which can partially reflect/transmit the incident EM wave. As shown in Figure 5.4 (b,c), at the air interface with the wall array, the incident light is partially reflected back to the air with a reflection coefficient,$\tilde{r}_{12}$ and partly transmitted into the spacer with a transmission coefficient, $\tilde{t}_{12}$,

$$\tilde{r}_{12} = r_{12}e^{i\phi_{12}}, \quad \tilde{t}_{12} = t_{12}e^{i\theta_{12}}. \tag{5.4}$$

The latter continues to travel in the porous area until it reaches the ground plane, with a complex propagation phase as

$$\tilde{\beta} = \beta_r + i\beta_i, \tag{5.5}$$

$$\tilde{\beta} = -\sqrt{\tilde{\epsilon}_{eff}}k_0\frac{P}{2}. \tag{5.6}$$

β_r is the propagation phase, and β_i represents the absorption in the porous layer. $\tilde{\epsilon}_{eff}$ is the effective permittivity of the porous layer, k_0 is the free space wavenumber and $\frac{P}{2}$ is the radius of the pore as thickness. After the reflection at the ground plane, the partial reflection and transmission waves at the wall-air interface occur from reverse direction after additional propagation phase $\tilde{\beta}$ in air void, with coefficients of $\tilde{r}_{21} = r_{21}e^{i\phi_{21}}$ and

$\tilde{t}_{21} = t_{21}e^{i\theta_{21}}$ respectively. Similar to the light propagation in a stratified media [164], the following multiple outgoing waves effectively traps the wave in the porous structure. Then the overall reflection is a superposition of the above multiple reflections. The overall reflection of the proposed structure from the air back to air can be written as [165],

$$\mathbf{R} = \tilde{r}_{12} + \frac{\tilde{t}_{12}\tilde{t}_{21}e^{i2\tilde{\beta}}}{1 + \tilde{r}_{21}e^{i2\tilde{\beta}}}, \tag{5.7}$$

where the first term is the reflection directly from the wall. The second term is the reflection resulting from the superposition of the multiple reflections between the wall-pore arrays and ground plane. The absorption is retrieved through $A(\omega) = 1 - R(\omega)$ since the transmission is zero. The reflection and transmission coefficients in the air-metal interfaces is given by the same Fresnel formulas 2.29 - 2.32 for different polarization (parallel and perpendicular E field), but the value of the refractive index for an absorbing media replaced by the complex quantities,

$$\tilde{n} = n - i\kappa, \tag{5.8}$$

$$\kappa = \frac{\lambda}{4\pi}\alpha, \tag{5.9}$$

where κ and α are the extinction and absorption coefficients, respectively. The angle of refraction is complex as

$$\sin\phi_1 = \frac{n_0 \sin\phi_0}{n_1 - i\kappa_1}. \tag{5.10}$$

For a particular case of $\phi_0 = \phi_1 = 0$ the Fresnel reflection coefficients are the same for both polarization mode (s and P) will be found as

$$\tilde{r}_{12} = \frac{n_0 - n_1 + i\kappa_1}{n_0 + n_1 - i\kappa_1}, \tag{5.11}$$

and the Fresnel transmission coefficient from air to media expressed as

$$\tilde{t}_{12} = \frac{2n_0}{n_0 + n_1 - i\kappa_1}. \tag{5.12}$$

Note that the reflection from ground plane is -1, so,

$$\tilde{r}_{21} = -\frac{2(n_1 - i\kappa_1)}{n_0 + n_1 - i\kappa_1}. \tag{5.13}$$

Because of the negative sign, the reflection coefficient from the wall back to the air ($\tilde{r}_{21}$) is the same with $\tilde{r}_{12}$. This formulation has been done in a region that the walls are skinny compared to the wavelength of interest. We should also extend these calculations to upper and side layers and estimate the wave behavior after entering the pores and traveling to lower layers.

5.2.3.2. Modeling based on Lumped LC circuit. We have already analyzed the electromagnetic properties of patch absorbers in Chapter 3. It proved those patch absorbers behave as an LC resonator that can be excited by an external magnetic field, exhibiting a strong resonance. As comes from the cubic design, 3D structures can be interpreted as resonators. The resonance mechanisms generating by the porous structure also can be interpreted quantitatively by the equivalent LC circuit theory. Figure 5.5(a) shows the unit cell topology of a porous structure while the pore size is at maximum value (after that point, walls could lose the interconnection among them). The metallic traces are inductive, which together with the void capacitances create a parallel combination of inductors with capacitors. C indicates the capacitance between adjacent walls that the parallel plate capacitance model can approximate its value. The flow of surface current from paths to the neighboring unit cells induces electromagnetic induction. As these paths are ring-shaped, the inductance of a single coil with averaged radius r_0 and width w determines L. In this model, we can not control the thicknesses of walls, path length, and uniformity. Instead, we obtained the complementary model [166] for porous structure by replacing the metal parts of the original design with apertures and the holes with metallic alloy as seen in Figure 5.5 (b). In this case, the original composition and its complementary are virtually dual. Here complementary model behaves like an electric dipole that can be excited by an external E-field. Changing C to L and replacing series connections to shunt ones and vice versa converts the circuit model of the complementary to the primary porous LC circuit. As depicted in Figure 5.5 (c), metallic bulk spheres can be excited; form surfaces for circulating current. Two adjacent spheres develop capacitance. We will consider the simple case of a metallic

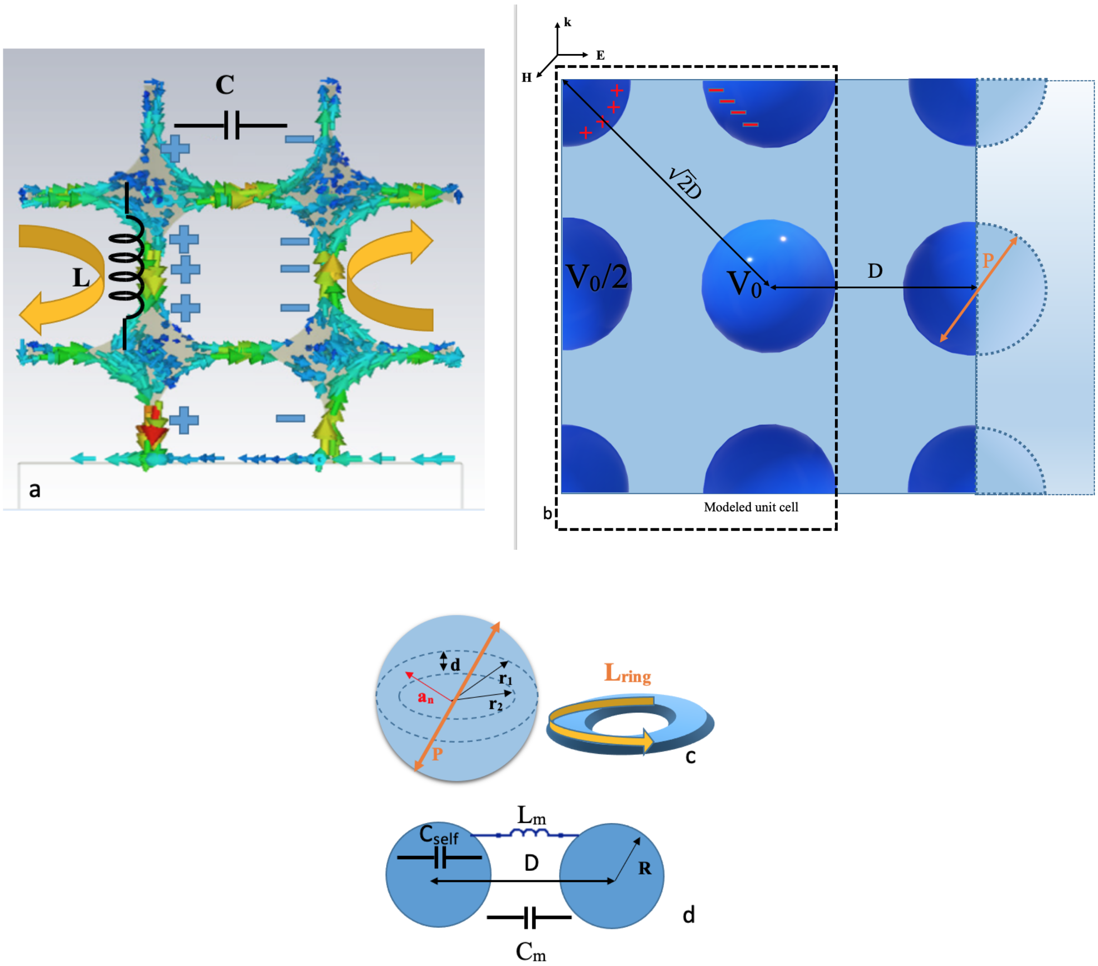

Figure 5.5. Lumped LC model of the porous metamaterial absorber,(a) paths and plates form inductances and capacitances of the porous model, (b) complementary model of porous MM (c) spherical segments for representing inductive rings (self-inductance), (d) mutual and self capacitances of two conductive spheres (mutual inductance originates among spheres).

sphere as an array of rings with mean radius of a_n in each segment , which the diameter of cylindrical ring is d and the cross section area is $S = \pi(d/2)^2$. In THz frequencies the current tends to circulate in surface corresponds to skin depth of δ.In this case $d = \delta$ and the radius of a ring in each segment is $r_n = \sqrt{{r_{n-1}}^2 - \delta^2}$ with knowing that $r_0 = P/2$ where P is the pore size. Assuming a uniform distribution of the current inside the ring, the final expression for the self-inductance of a perfect conducting ring can be efficiently calculated as L_{ring} is [167],

$$L_{ring} = \mu_0 a_n \left[\ln(\frac{16a_n}{\delta}) - \frac{7}{4} \right], \quad a_n = \frac{r_n + r_{n-1}}{2}. \tag{5.14}$$

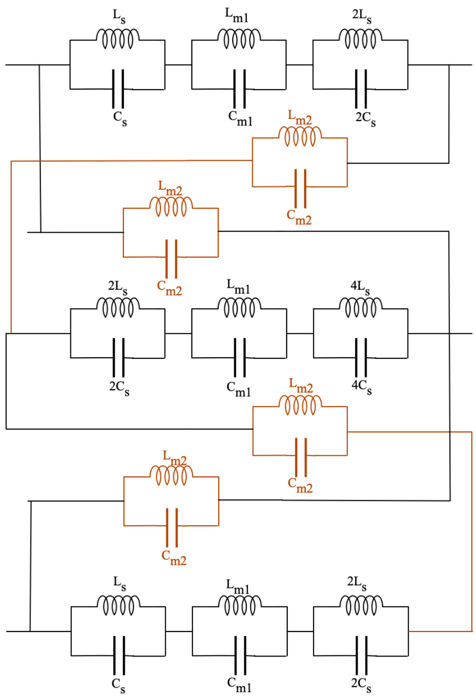

Figure 5.6. 1D equivalent circuit of the complementary model.

Number of rings is a function of skin depth and pore size: $n = \frac{P}{\delta}$. Knowing that the rings are in series, the total inductance for a conductive sphere is estimated as

$$L_{sphere} = \sum_{n=1}^{k} \mu_0 a_n \left[\ln(\frac{16a_n}{\delta}) - \frac{7}{4} \right]. \tag{5.15}$$

We outline the classical results obtained for the capacitance of two conductive spheres with exact sizes using the method of images listed in Maxwell's book [168]. As shown in Figure 5.5(d), two spheres 1 and 2 of identical radii R, and their centers separated by distance D, are held at voltage V. The spheres' charges are related to the given voltages through the matrix equation proved to be the same. self capacitances and mutual capacitance are depicted in Figure 5.5(d) where C_{11} and C_{22} are the self capacitances of the two spheres and $C_{12} = C_{21}$ is their mutual capacitance. These capacitances depend only on radius and spacing between spheres. The capacitances are defined in terms of α as

$$C_{11} = C_{22} = 4\pi\epsilon R \frac{1-\alpha}{\sqrt{\alpha}} \sum_{k=0}^{\infty} \frac{\alpha^{k+1/2}}{1-\alpha^{2k+1}}, \tag{5.16}$$

$$C_{12} = C_{21} = 4\pi\epsilon \frac{R^2}{D} \frac{1-\alpha}{\sqrt{\alpha}} \sum_{k=1}^{\infty} \frac{\alpha^{k}}{1-\alpha^{2k}}, \tag{5.17}$$

where $\alpha = s - \sqrt{s^2 - 1}$ and $s = \frac{D}{2R}$ and the permittivity of the surrounding medium is ϵ which in this case is equal to permittivity of air. There are two types of mutual capacitances. One between contiguous elements (quarter sphere), C_{m1} and the other among spheres across the diameter in a distance of $\sqrt{2}D$, C_{m2}. The current flows in the first sphere I_1 gives rise to a magnetic field B_1. Some of these magnetic field lines will also pass through neighboring spheres. A magnetic flux ϕ_{21} through the second component due to time-varying current I_1 will pass. Mutual inductance is proportional to this magnetic flux. Separation of elements will affect this mutual inductance. L_{m1} is due to D interval, and L_{m2} is due to $\sqrt{2}D$ interval. Figure 5.6 represents the equivalent circuit of the complementary model of porous structure for one dimension.

We converted the inductance to capacitance, replaced the series connections to parallel and vice versa to obtain a one-dimensional equivalent circuit of the porous resonator as depicted in Figure 5.7 (a). The equivalent circuit for 3D porous MM absorber achieved by repeating the LC circuit in Figure 5.7 (a) for two adjoining faces. The circuit simulation results for P = 7.5 μm has been done by "Qucs". Resonant

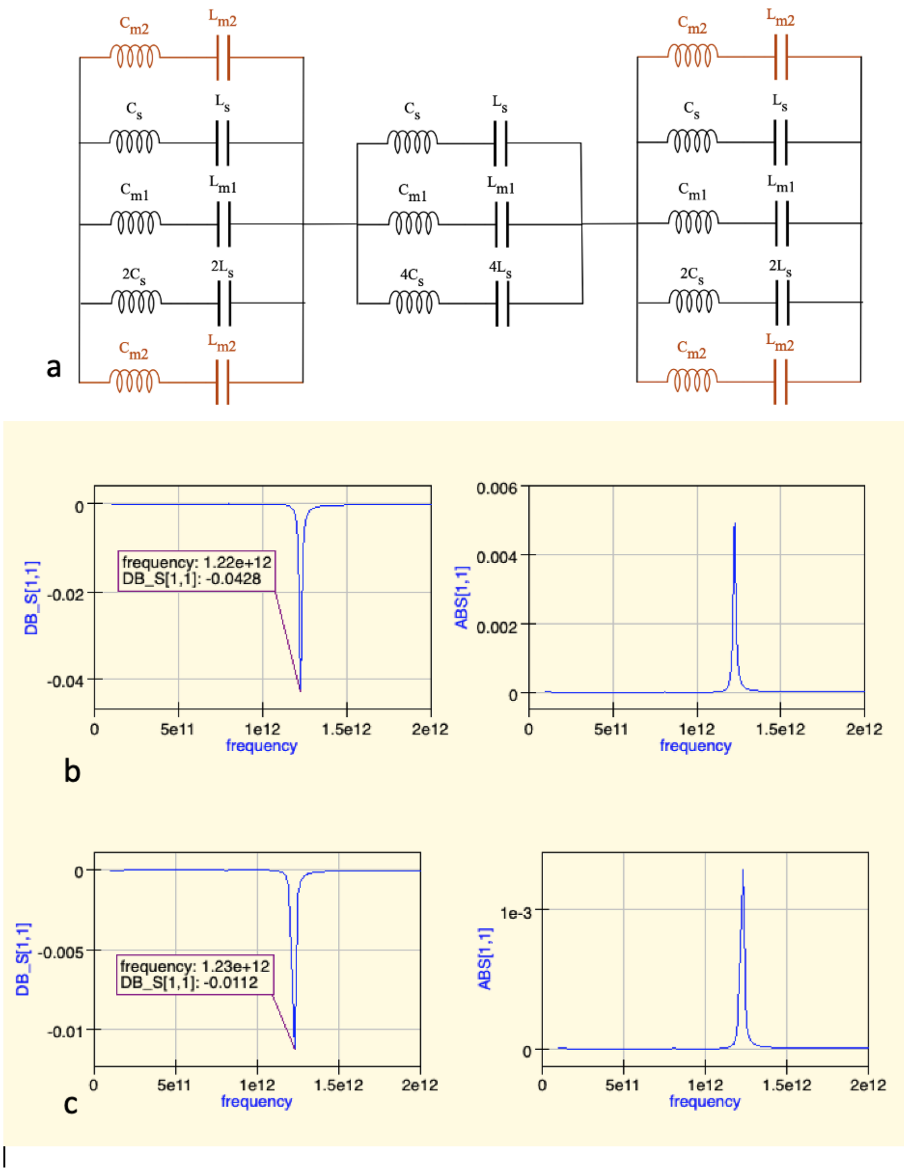

Figure 5.7. (a) Equivalent circuit of porous absorber for one face, (b) resonance happens at 1.22 THz for the 1D model, (c) numeric results for a 3D porous MM absorber showing a resonant frequency at 1.23 THz.

frequency takes place at 1.22 THz. The electrical and magnetic properties of CoNi alloy is estimated based on paper reviewed [153]. Based on the formulas mentioned earlier, the equivalent capacitor and inductance can be denoted almost as a function of R, D, and ϵ, the radius of spheres, intervals between them, and the electrical permittivity of the massy parts, respectively. The dependence of the resonant frequency on R, D, and material type are consistent with the prediction of the LC circuit theory. This consistency provides a chance to shift the proposed MM absorber's operating frequency range by adjusting the R and D of the structure while all the other parameters are fixed.

5.2.4. Simulations, Physical Parameters Dependency, Fields and Current Distributions

We concentrate on modeling a three-dimensional interconnected porous MM absorber with a pore size of p = 7.5 μm and 13.5 μm periodicity. The Absorber is made of Co/Ni alloy formed on top of a background mirror. At the bottom, Ti/Au films are placed on a Si substrate as the background mirror, prevents incident power transmission. Figure 5.8(a) represents the computational model for the 3D porous absorber. We excite the sample through port one by a normal incidence EM wave where port two is grounded. Periodic boundary conditions are considered, PEC and PMC, along $\tilde{x}$ and $\tilde{y}$ directions, respectively. Finite element method has been developed using CST Microwave (frequency-domain solver) and applied to obtain simulated S-parameters so the power transmittance $T(\omega) = |S_{12}(\omega)|^2$, power reflectance $R(\omega) = |S_{11}(\omega)|^2$, and power absorptance $A(\omega) = 1 - T(\omega) - R(\omega)$. Figure 5.8(b,c) shows the transmission, reflection, and absorption spectra of the proposed THz absorber, as well as a non-porous cubic with the same unit cell length of 27 μm. It demonstrates that the BW of absorptivity for a porous absorber improves; its maximum value reaches 81% at 1.47 THz. For the proposed absorber, the first resonance bandwidth becomes almost 300 GHz, and for the second resonance (4.1 THz) 290 GHz, where the BW for the nonporous one is 75 GHz at 0.54 THz and 460 GHz at 4.1 THz. Compared to the numerical calculation based on lumped LC circuit, the simulation results are in a good match where it predicted the resonant frequency could occur at around 1.2 THz. Note that a slight mismatch is because we have not considered the mutual capacitance and inductance in $\tilde{z}$ direction.

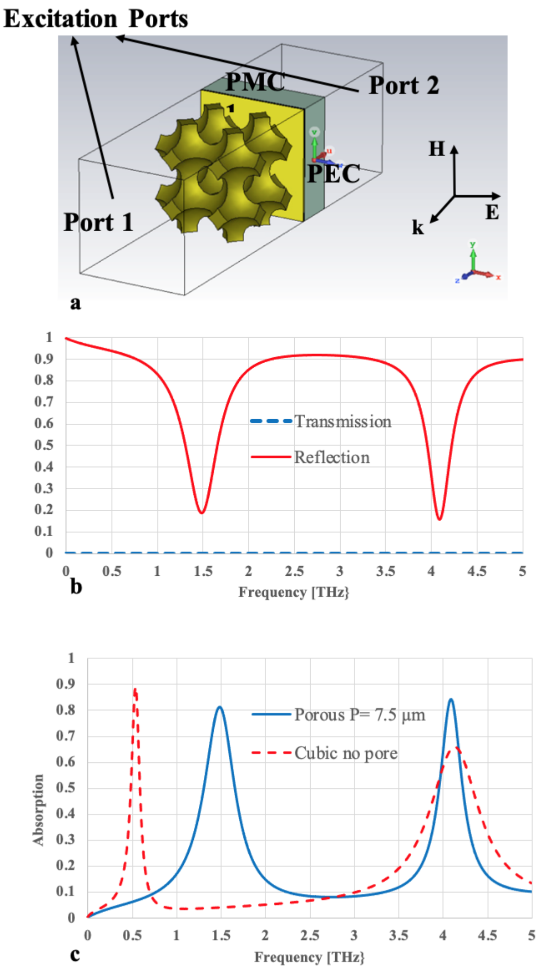

Figure 5.8. (a) Computational model of porous MM absorber unit cell, (b) transmission (blue-dashed) and reflection (red-line) spectra of the proposed design obtained from S parameters, (c) absorption spectra comparing porous MM absorber (blue-line) and cubic absorbers (red-dashed).

To justify the capacitance existence in pores, x,y and z components of E field distribution have been brought in Figure 5.9 (a-f) for $P = 7.5\mu$m and $P = max$ cases. The orientations of $\tilde{k}$, $\tilde{H}$ and $\tilde{E}$ also is playing important role in composition of capacitance. However, the structure is symmetric along $\tilde{x}$, $\tilde{y}$ and $\tilde{z}$. So, unless E and

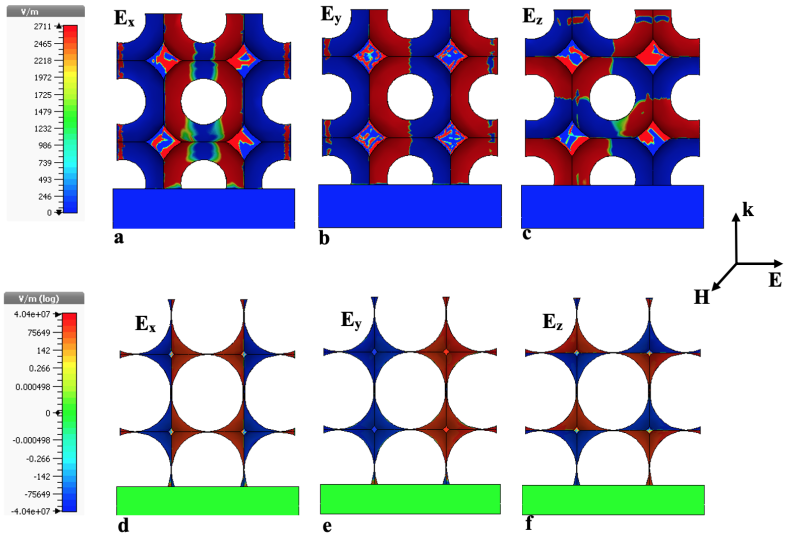

Figure 5.9. Simulated electric field distribution for the porous absorber, (a, d) x component, (b, e) y component, and (c, f) z component, respectively. The first row shows the electric field distribution for P = 7.5 μm (side-view), the second row illustrates it for the P = max (side-view).

H are not oblique with respect to $\tilde{x}$, $\tilde{y}$ and $\tilde{z}$, we expect to excite the same resonant behaviour. Consider red color as positive charge and blue color as negative charges. This polarization proves the presence of capacitance between walls.

To investigate the origins of the absorption peaks, we also presented total electric field and surface current intensities at two resonant frequencies in Figure 5.10 (a-d). The pictures illustrate the electric field and surface current distributions, at 1.47 THz and 4.1 THz. At low frequency, the absorption peak originated by magnetic excitation mode. At the first resonance of 1.47 THz, the electric fields localized at the absorber's left and right aspects uniformly (as we have seen in cubic case Figure 5.2). The surface current flowing in a manner that points to the H-field direction and can be treated as a magnetic resonant mode as depicted in Figure 5.10 (a,b). Figure 5.10 (c) shows that the electric field concentrates more on the edges of the porous structure at f = 4.1 THz. As the frequency increases, field patterns become stronger at both sides of the U-shaped rings. The opposite charges accumulate in the porous absorber's edges and central parts (if we consider the blue color as negative and red color as positive charge). This indicates excitation of dipolar resonance in the patterned structure, which will not produce a considerable reflected power; consequently, most of the incident power will be absorbed by the honeycomb shaped absorber.

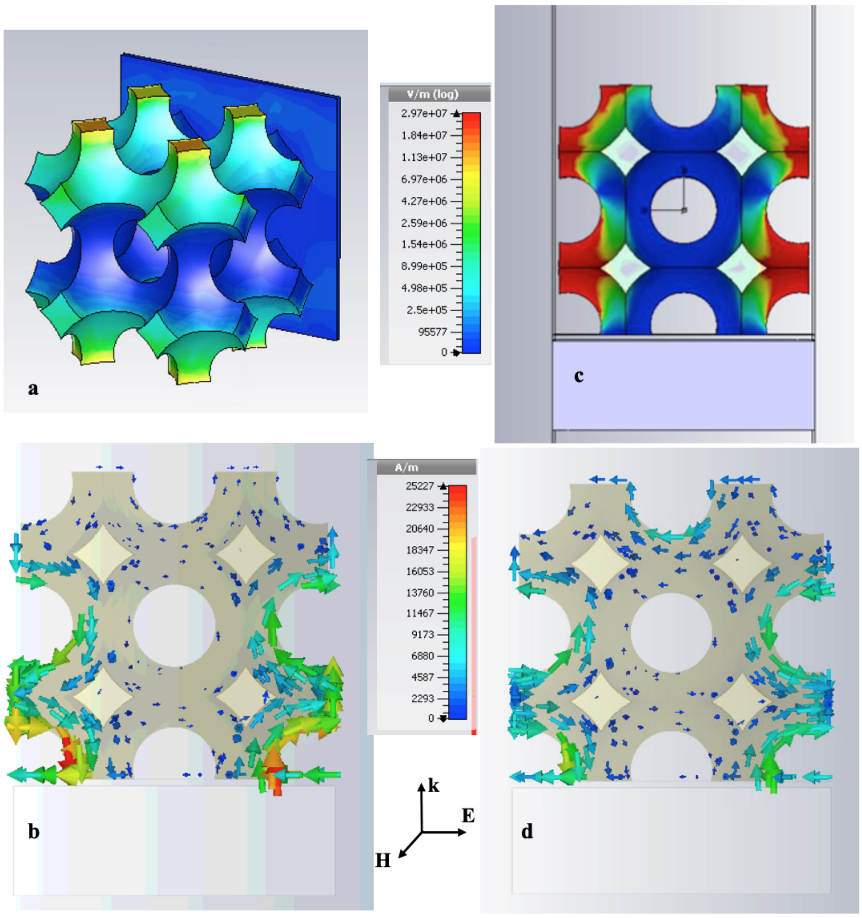

Figure 5.10. Simulated electric field and surface current patterns for the porous absorber at (a, b) 1.47 THz, (c, d) 4.1 THz. The first row shows the electric field (side-view), while the second row illustrates the current distribution.

At f = 4.1 THz, the surface current patterns circulate between points with different potential level as shown in Figure 5.10 (d). This shows the effectiveness of having smaller path sizes to achieve a higher absorption resonant frequency and a wider operating frequency band.

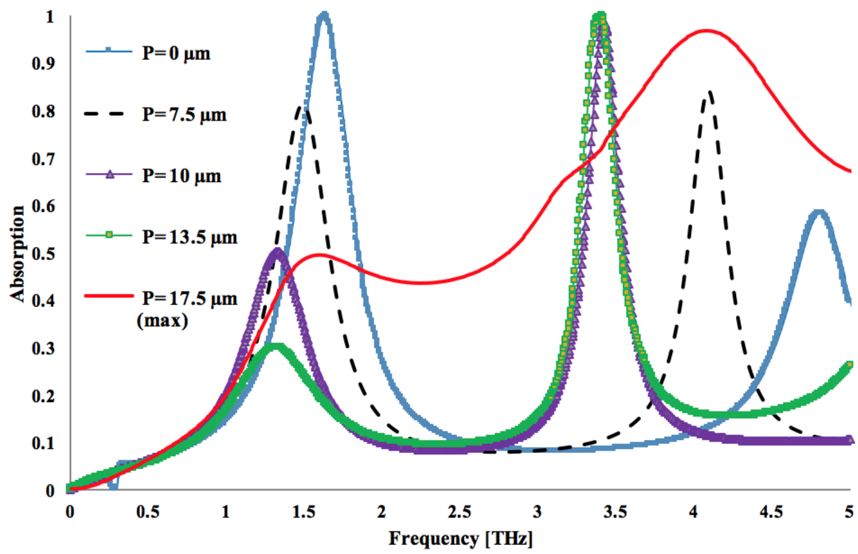

Figure 5.11. Simulated absorption spectra for various pore sizes. P = 0 is for the case where there is no pore but some non-uniformities. Maximum pore size achieved when there would not be interconnection.

Taking a further step, we also studied the influence of the unit-cell structure's geometric parameters on the absorption properties of the proposed MM absorber. Analysis of equivalent LC circuit theory discussed earlier explains the effect of geometric parameters on the MM absorber behavior. According to the LC model, the absorption properties of the MM absorber mainly depend on the pore size P. Firstly, the unit-cell structure of the porous absorber with different pore sizes of $P = 0$ μm, 7.5 μm, 10 μm, 16.5 μm and 17.5 μm (maximum pore size) are examined. At the same time, other geometric parameters as the number of layers and porosity are unchanged. Results shown in Figure 5.11 indicate that the operation frequency at lower resonances are nearly unchanged (0.35 THz variation), while the absorption level has an obvious decrease with the increase of P (except for the maximum P case). This outcome is predictable as increasing pore sizes have minimum effect in circulating current paths (see Figure 5.12); therefore, the resonance shifts are negligible. By increasing the pore size and losing material structure (resistivity), the chance of refraction minimizes; thus, absorption level drops. For maximum pore size, the walls are thin, and as it comes from Figure 5.12 (b), most parts of the proposed absorber can be excited.

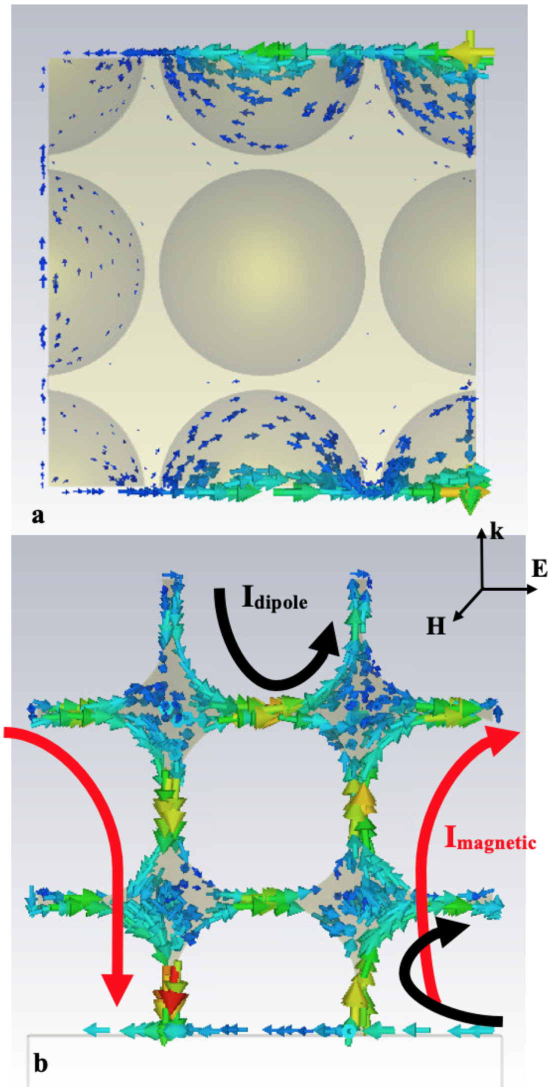

Figure 5.12. Simulated surface current distribution for (a) P = 0 μm and (b) maximum pore size.

There are two types of the current flowing: magnetic excitation current $I_{magnetic}$ and electric dipole current I_{dipole}. The simultaneous presence of these two currents suggests a new way to obtain the ultra-broadband MM absorber designs. The method integrates different resonant modes in a single patterned structure. As pore size goes to the maximum and using structuring technique, a near-perfectly reflective metallic alloy is transformed to highly absorbent material over a broad electromagnetic spectrum, ranging from 1.5 THz to 5 THz.

Next, we discuss the effect of the number of porous layers on the absorptivity. The absorbance of the MM absorber with 0.5, 1.5, and 2 layers is simulated when all other geometric parameters are fixed, as shown in Figure 5.13.

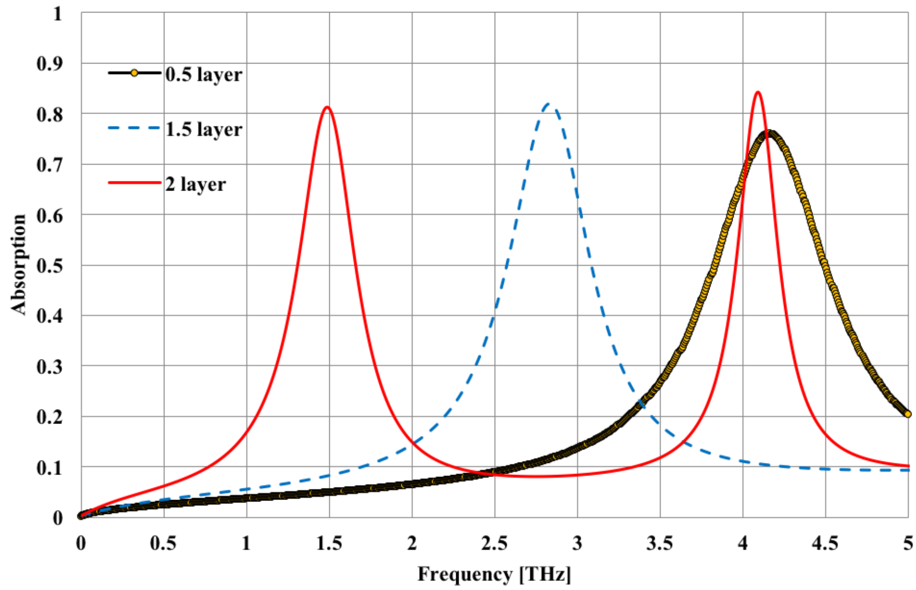

Figure 5.13. Simulated absorption spectra for different layer numbers, 0.5, 1.5, and 2 layers of porous MM absorber.

Figure 5.13 shows that the resonant frequencies tend to the higher frequencies by removing the layers. The absorption peaks remain almost unchanged when the parameter P is unchanged and is 7.5 μm. Based on the multiple reflections interference model, It can be seen that the trapped incident beam travels less absorbing media by removing the layers, and the path becomes shorter.

Furthermore, we discuss the effect of polarization (E-field angle) and incident wave angle (k-vector) on the device's absorptivity. The dependency of the structure's resonance characteristics with respect to the orientation of the electric field is simulated by changing the angle between the electric field vector and the x-axis. The electric field and the magnetic field vectors are in the plane of xy. The incident wave was kept perpendicular to the device along the z-axis. Absorbance characteristics of the structure with different values of β are plotted in Figure 5.14 (a).

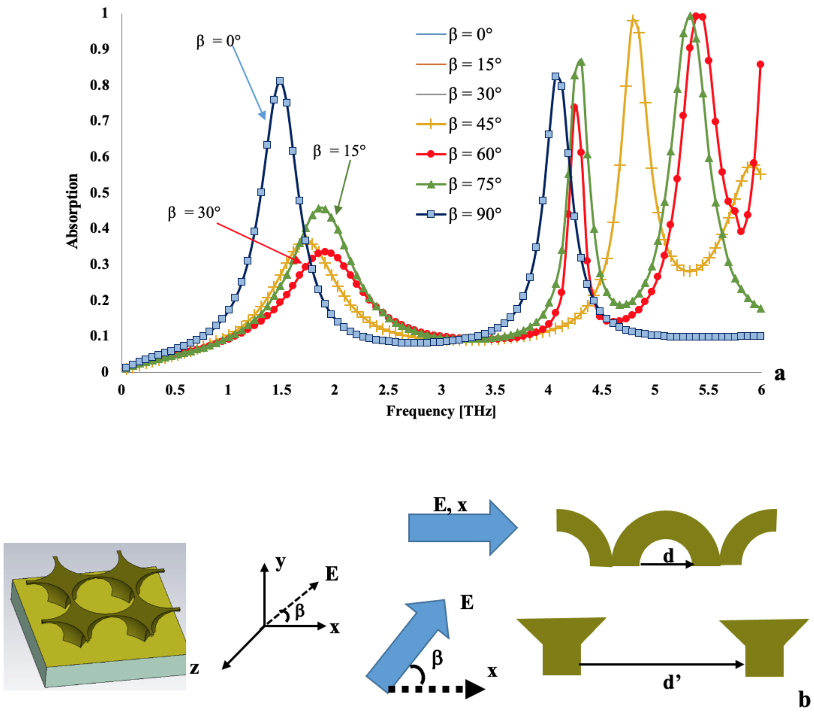

Figure 5.14. Absorption spectra for different polarization angle, (a) simulated result, (b) 1/4 layer porous MM presentation and cross-sections for $\beta = 0°$ and $\beta \neq 0°$ cases.

It is obvious that because of the symmetry of structure when $\beta = 15°$ and $75°$ absorption bands are identical, this is true for the case when $\beta = 30°$ and $60°$, and the absorption spectra are the same. Note that $\beta = 90°$, settled the structure into the same position as $\beta = 0°$ case, and accordingly resonant characteristic repeats itself. The length of the path that induced current is circulating through determines the resonant frequency of the structure. For $15° < \beta < 75°$ this path has been not altered and almost is the same (see inset in Figure 5.14 (b)). In this case, the resonance shift is less than 100 GHz, which is acceptable. However, when $\beta \neq 0°$, $90°$ the structural distance (d') becomes larger, which causes small capacitance, thus higher resonance frequency. A longer inductive path makes a drop in Q-factor as losses increased. In comparison, the dependence of absorption characteristics to the polarization angle is negligible, and this device is polarization independent.

Six different angle values of 0, 15, 30, 45, 60, and 75° were selected to investigate the influence of incidence angle for TE mode on absorbing performance by varying the angle between the incoming EM beam and z-axis. The absorption spectra of the structure for various incident beam angles are depicted in Figure 5.15. Drawing paths for each position, that an EM wave with different incident angle forms, like the polarization-dependent path, can predict the absorber's response. Absorption spectra should not change as the direction of electric and magnetic fields are the same. The symmetry of the structure yields the incident wave angle in-dependency of the absorber. The structure performs well as original absorber ($\theta = 0°$) and absorptivity remains unchanged for $\theta = 30°$, $\theta = 45°$ and $\theta = 75°$ cases by limiting the absorption band between 1 THz and 1.5 THz. The shift of resonant frequencies is 0.4 THz.

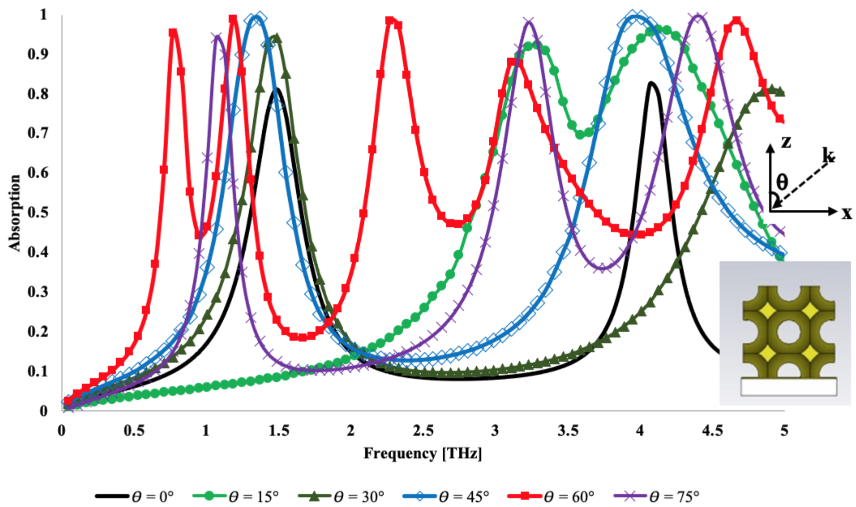

Figure 5.15. Simulated absorption spectra for different k-vector angle.

When θ is 15°, resonant frequency drift to the higher frequency as two modes of excitation overlap, and the absorption peak reaches a high level (98 %). Although there are more than two absorption resonant frequencies for $\theta = 60$, there is an absorption band in 1- 1.5 THz matching the nominal one. It is evident that oblige EM wave enhances absorption peaks thus absorptivity. It will increase with the increase of the incident angle.

5.2.5. Fabrication

In paper [169], porous nanostructures as spectrally selective wideband absorbers are presented. The porous samples we have characterized in this thesis are fabricated at the Institute of Robotics and Intelligent Systems, ETH Zurich, Switzerland by J. Pokki and his group. Porous CoNi nanostructures were fabricated by a custom colloidal lithography process with electrodeposition of Cobalt-Nickel (CoNi) as depicted in Figure 5.16. Silicon chips (<100>) of 1 cm^2 area were used as a substrate. First, the silicon chips were coated by a 2 nm titanium adhesion layer and 6 nm gold seed layer using e-beam evaporation. Gold coating as a conductive seed layer is necessary for electrophoretic deposition (EPD) of polystyrene (PS) beads and electroplating of CoNi nanostructures.

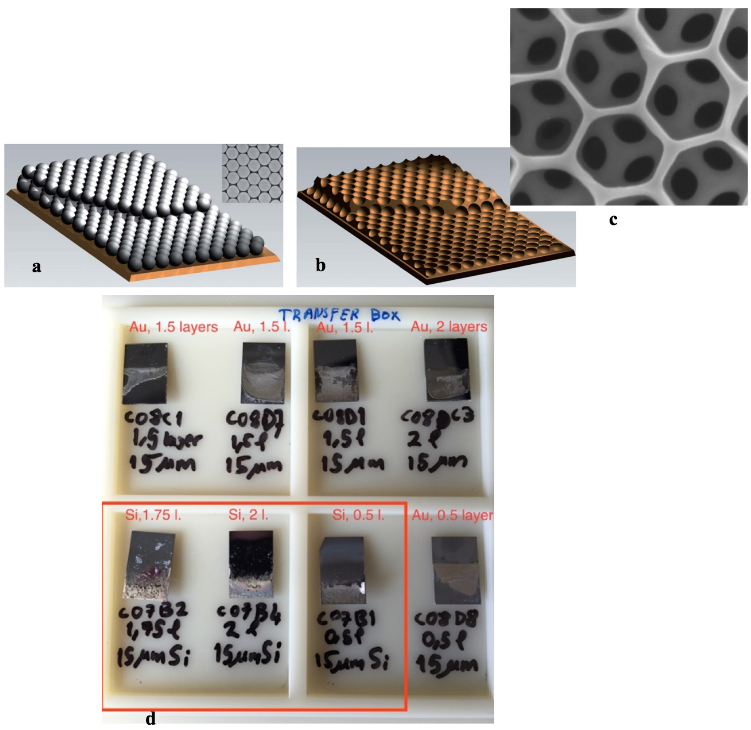

Figure 5.16. Fabrication process: (a) PS beads were EPD-assembled onto a substrate (illustrated in the insets), (b) electrodeposition of CoNi to the interstitial voids of the beads, (c) SEM image of the final porous structure, (d) fabricated samples with different substrates and layers [159].

PS nanospheres of various sizes can be used to tune the pore size in the structure. Directed self-assembly of PS bead, as the most critical part of the fabrication, affects the defect density, thickness, and pore size of the 3D porous nanostructure. Hence, it is important to understand how to control the thickness of the PS nanosphere layers and maintain a constant thickness over the sample. Depositing PS nanosphere layers with a consistent thickness is difficult due to the changing deposition current. The thickness was controlled by keeping the product of the applied electric field and deposition time constant. The PS bead size tuned the pore size of the nanostructure that is critical regarding absorber characteristics. Figure 5.16 (a) shows the PS beads assembled on the chips using EPD. Following the PS-bead assembly, CoNi was electrodeposited into the interstitial voids of the PS beads. The desired thickness was achieved by controlling the current density and deposition duration. After electrodeposition, PS beads were etched by ultrasonicating in chloroform for 10 min (Figure 5.16(b). Figure 5.16(c) shows SEM image of CoNi honeycomb structure. Different thicknesses of deposited CoNi form the layer of honeycombs. The fabricated samples are with 0.5, 1.5, and 2 layer-thick that form 7.5, 22.5, and 30 μm thick CoNi honeycombs. Two sets of the device were fabricated. One set which has Ti/Au layers on silicon, and the second one honeycomb structures are build directly on silicon. They are marked with “Si” in the Figure 5.16 (d). However, the porous structure on the Si wafer was not fully covered because of poor adhesion.

5.2.6. Characterization and Measurement Results of Porous 3D MM THz Absorber

Both transmission and reflection-mode measurements of the different fabricated absorbers and a nonporous sample (blanket CoNi) were performed using a terahertz time-domain spectroscope (THz-TDS, TERA K15, Menlo Systems GmbH,Martinsried, Germany) with spectral coverage from 0.3 to 2 THz. Nonporous sample is used as a reference in reflection mode experiments. Please refer to the Appendix A for measured data. When compared with the blanket substrate, it is clearly shown that the proposed absorber can increase the absorptance due to multiple reflection resonances and minimizing the transmitted power. Measurements have been done for four samples with different layer numbers. Sample 1 is a 0.5-layer, samples 2 and 3 are 1.5-layer structures, and device 4 is a 2-layer one. As shown in Figure 5.17 and Figure 5.19, measured results for sample 1 and 4, in general, agree well with simulated values, the designed resonant frequencies verified. A redshift resonance for the third and fourth samples happened where absorption band dropped to around 0.5- 1.13 THz (Figure 5.18.

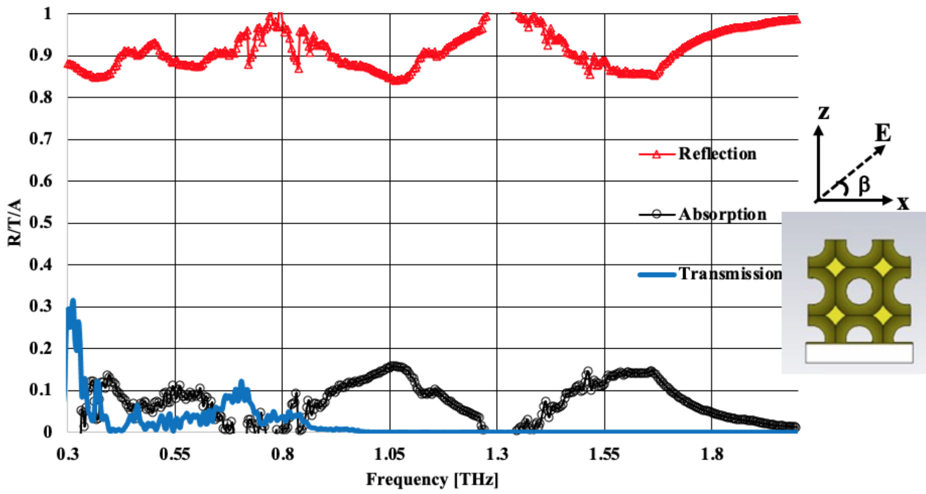

Figure 5.17. Measured reflection (red), transmission (blue), and absorption (black) spectra for sample 1 with 0.5- layer porous structure.

As we expected from simulations carried out from CST, there is no absorption band for 0.5 layer sample in 0.3 -2 THz band, and all of the incident power is reflected. There is a small amount of transmission in lower frequencies as porous MM is not covering the wafer thoroughly (see Figure 5.16 (d)).

Figure 5.18 represents the experimental results of sample 2 and 3 with 1.5- layer porous MM absorber. Sample 2 measurements were performed in two various positions. At Vertical position, the sample is placed on a holder with an angle of 0° concerning the holder's axis. This angle is 90° for the horizontal position. It is evident that the absorption trend in the two situations is similar; hence absorption level is dissimilar, rising from the non-uniformity of the fabricated devices in each dimension.

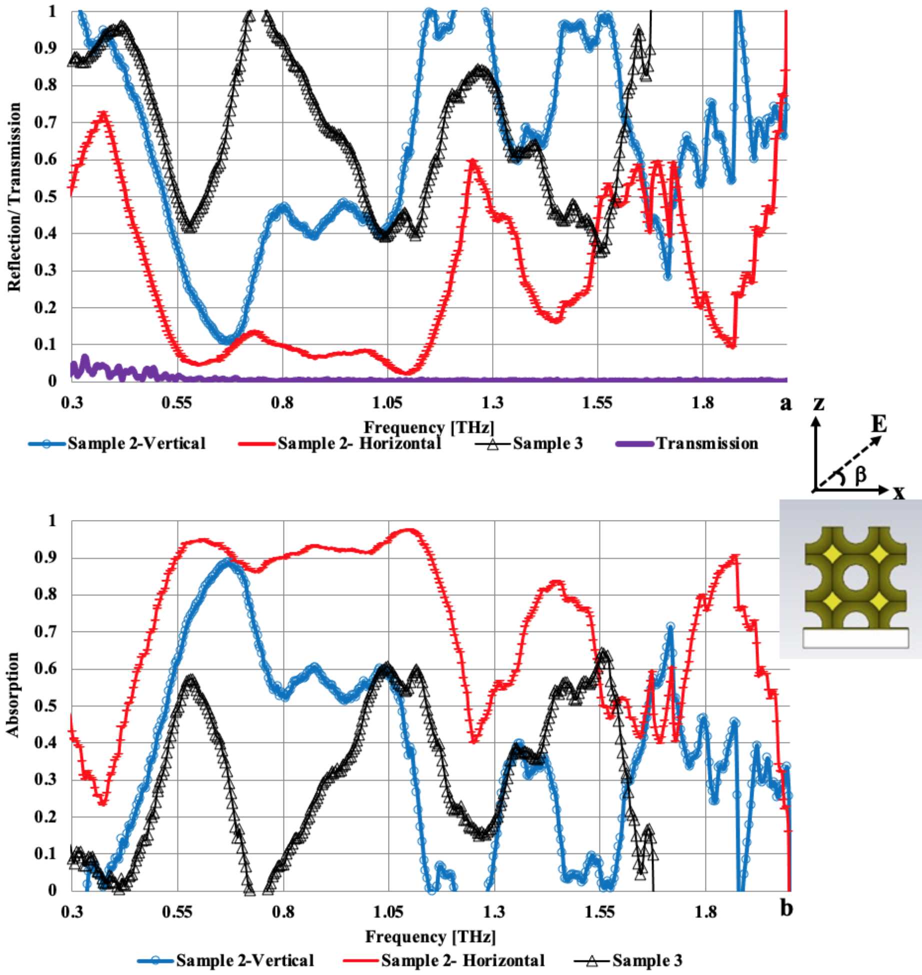

Figure 5.18. Measurement results (a) reflection and transmission(purple), and (b) absorption spectra for sample 2 and sample 3 (black) with 1.5- layer porous MM absorber. For sample 2, experiments have been done in two different vertical (blue) and horizontal (red) positions.

As shown in Figure 5.18, the absorption and reflection spectra for sample 3 (black-line) with the same number of layers (1.5 layers) have a resonant gap between 0.65 THz and 0.95 THz, which is because of the defects in fabricated chips. The transmission of the incident wave is zero over the desired frequency band.

The absorptivity is observed at a wide frequency band for sample 4 with two layers of MM absorber; the behavior is very close to the simulation results, an absorption band of 312 GHz between 1 THz and 2 THz is observed as plotted in Figure 5.19 (b).

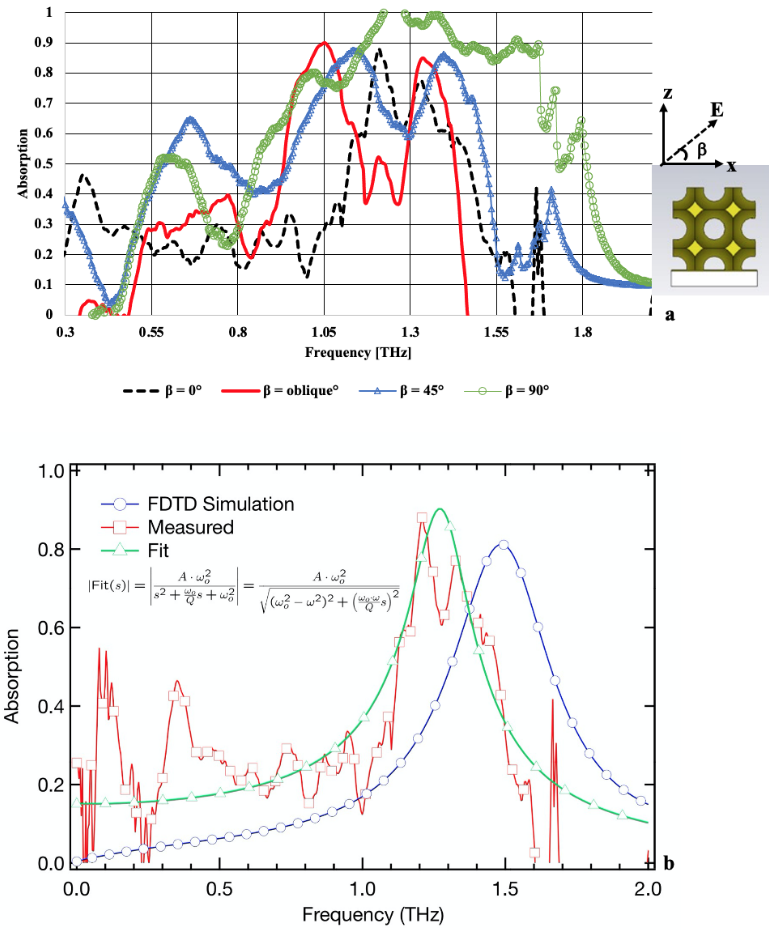

Figure 5.19. Measurement results (a) absorption spectra for sample 4 with 2 layers of porous MM absorber. Experiments have been done in four distinct vertical (black-dash), 45° (blue), oblique (red-line) and horizontal (green) positions, (b) comparison of simulated (blue) and experimental (red) results for 2-layer sample in vertical position case. A polynomial curve is fitted (green).

For sample 4, experiments have been done in four distinct positions vertical (0°), 45°, oblique ($45° < \beta < 90°$) and horizontal (90°) positions. Experiments show a good consistency with the simulation results in each position however expected drop of absorptivity is absent.

The measured amplitudes of absorption for the 1.5- and 2-layer samples are more significant than the numerical results. The minimized reflected power can partially explain it due to the variation of size, porous arrangement, and electromagnetic properties of the material and dielectric loss. The area of the sample illuminated by the antenna may also lead to a drop of reflection much more than simulated ones. As we expected, the simulated and measured amounts of the absorption of device number 4 show good agreement within the frequencies (see Figure 5.19(b)). Accordingly, apart from the fabrication error, the inconsistencies between simulated and measured outcomes originate from disagreements in dielectric properties of Co/Ni alloy in the simulation software and reality. Furthermore, The numerical model considers one unit cell of the proposed design. In real-time measurements, a larger area of the device is illuminated; thus, multiple unit cells will perform as absorbers under test.

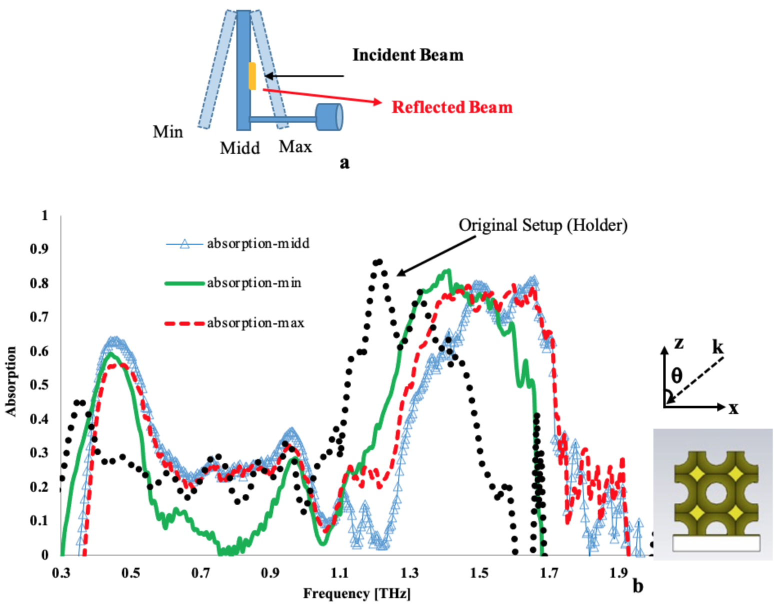

Figure 5.20. (a) Schematic drawing of a kinematic mount and its various positions (b) Measurement results of absorption spectra for sample 4 with 2-layer porous MM absorber in three situations: min (green-line), mid (blue-triangle), and max (red-dash). The curve in black-dots shows the experimental result of the original setup.

To experimentally verify the in-dependency of the resonator's behavior to incident wave angle, we have done a series of measurements using a kinematic mount. Tilting the plate where the sample is on it causes deflection; therefore, the incident wave's angle changes. The mount has 4 of tip and tilt control. Measurement has been done in three positions, Min position where the tilting angle is negative, the middle point where the deflection is zero, and max condition where the tilted angle is positive as shown in Figure 5.20 (a). Analyzing the experimental results of several incident angle values and comparing with nominal absorption spectra which come from previous measurement setup where the holder is a mirror mount instead of a kinematic mount, shows by increasing the tilting angle, a slight change (blue shift) occurs at absorption resonant frequency. The absorbing trend is the same. Comparing with simulation results, one can conclude the correspondence of numerical results with measurement ones. Consider that the maximum deflection we can achieve is 8 degrees.

6. Conclusion

New designs of metamaterial-based THz absorbers for sensing applications are the main objectives of this research. square metallic resonator, a dielectric spacer, and a ground layer modeled, characterized, and experimentally verified. At its resonant frequency, near-unity power absorptance can be achieved as both transmitted and reflected power are minimized. We designed multiple square patches with different geometries on a thin layer of Parylene suspended over a substrate for a frequency range of 0.5-2 THz. For example, the resonance frequency of a patch size of 86 μm is 0.93 THz, and the bandwidth is 155 GHz. These values for 43μm square are f = 1.49 THz and BW = 340 GHz. We reported reduced absorptivity from 95% to 77%. The first metamaterial-based absorber by Landy et al. [53] demonstrated a simulated absorptivity of 70% at 1.3 THz and BW 200 GHz. This thesis presents a MEMS-based THz detector using an array of multi-size square patch resonators that can be used as an effective multiband terahertz absorber. The fabricated device exhibits strong absorption peaks of 80 % at corresponding frequencies and an average absorbance value of 0.4 in the specified band of 0.3-2 THz as reported in Chapter 4. We analyzed the behavior of the absorber under variation of the angle of polarization and incident wave. The absorber performs well even with a large value of incident wave angle. However, changing the absorber position from vertical to horizontal causes the absorption band related to the bi-material leg to diminish (which is not our interest as the bi-material leg is not a part of the absorbing mechanism). Finally, by including more patches with various side length sizes, a wideband THz absorber is fabricated with multi absorption peaks. The analysis and the experimental data indicate that the presented device is suitable to realize a passive, uncooled THz detector. The device is promising for spectroscopy and can be employed as a building block of an imager for security and medical applications. Future studies aim to package thedetector in a vacuum with terahertz optics and implement an imager using a large-array a focal-plane array comprising detector pixels. In principle, this design can operate within both the THz and Far-infrared regions. This will be beneficial for various applications, including sensing [100], wireless communications [170], imaging [113], and energy harvesting [38], where wide bandwidth are essential.

Generating various air cavity modes to diminish the reflection over a large bandwidth, thus broaden the absorption band, is another approach we used to design our next THz absorber. The unit cell consists of a honeycomb-shaped metal alloy formed on a silicon substrate coated by a Ti/Au layer. We have designed, fabricated, and experimentally demonstrated a wideband absorber within the THz and far-infrared spectra. Fabricated unit cell contains 7.5(0.5-layer), 22.5 (1.5-layer) and 30 (2-layer) μm- thick Co/Ni interconnected structure with inner air cavities. For the proposed absorber (7.5 μm pore, 2-layer), the bandwidth at first resonance (1.47 THz) becomes almost 300 GHz and at second resonance (4.1 THz) 290 GHz, where the BW value for nonporous cubic is 75 at 0.54 THz. The power transmittance for both the porous absorber and nonporous sample is zero. In principle, the multiple Fabry-Perot resonance cavities formed within this structure achieved the wideband absorption. The average absorptance with the THz-TDS measurements for the 1.5-layer device is 90% from 0.5 to 1.2 THz. Simulation and theoretical calculation results for 2-layer devices exhibit that the absorbance of 85% between 1.14 THz and 1.44 THz can be realized. For normal incidence, the device's absorbance is 0.45 in a band of 0.3-1.6 THz, and the FWHM is measured to be 40%, which is larger than the experimental value 22% reported for 86 μm patch absorber. This amount is 25% for 43 μm patch size, while for 30 μm and smaller patches, there are no measured amounts. There are no measured results for the 0.5-layer device as the corresponding resonance frequency is out of the spectrometer range. Furthermore, analyzing field and current distributions of porous MM absorbers proves field enhancements are mainly located within faces' apertures. This is highly desirable for biosensing applications as it increases the overlap of the analytes with the electromagnetic field inside the aperture [171]. Further simulations and experiments showed that the designed porous MM absorber could operate well at a wide range of polarization. Thus, it is polarization-insensitive and can consistently sustain high power absorptance for incident angles up to 75°. Comparing with recent examples of 3D MM absorbers help us understand the novelties of our device. In the first one, an ultra-wideband absorption was achieved due to multiple cavity mode resonances in silicon cross resonator with an internal cross-shaped air cavity and bulk absorption of the doped silicon substrate. The measured average power absorptance is 95 % between 0.2 and 2.5 THz [134]. Second one is a GHz Metamaterial absorber consisting of honeycomb and resistive films. It can realize an absorptivity of more than 90% in a wide band of 3.53–24.00 GHz [172]. A single-layer, flexible and broadband terahertz metamaterial absorber consists of four sub-cells with multiple metal rings is reported in [173]; an average absorption amount of 88% from 0.63 to 1.34 THz is reached. Compared with the previously reported THz MM absorbers, the main novelties of our proposed porous structure include the compact unit-cell structure and exclusive operating mechanism as a resonator. Secondly, a nearly perfect THz absorber can be realized with a single resonator structure that operates broadband. Finally, the designed MM absorber is polarization-insensitive, and wide-angle absorptivity for both TE and TM waves is reported. Thus, the porous design has potential applications in communications, sensing, and imaging at THz frequencies.

Future work: We concluded the absorption level and working frequencies are sensitive to the geometrical parameters from numerical calculation and analysis. By adjusting the size of the pore carefully, the MM absorber structure can be an effective broadband absorber. It is theoretically shown that the absorption for a porous absorber improves as the pore size approaches its maximum value, providing an ultra-wideband absorber over 1.5 - 5 THz band. Overlapped resonant modes make the proposed structure with maximum pore size obtain a broadband response. Even though the porous design is promising, but there are some problems to be solved. The fabrication process can not assure the uniformity of pores and their sizes. Releasing the PS beads can be problematic, and some of them may still stick in the structure. Thus the final porous structure may have some dissimilarities over the whole sample. Various areas on a specific sample may show a different resonant behavior while the incoming beam impinges. Resonant frequency would shift whenever the position of the sample is substituted. Accordingly, the characterization should be limited to a tight area on the sample.

APPENDIX A: WORKING PRINCIPLES OF THz-TDS AND MEASUREMENT RESULTS OF REFERENCE MATERIALS

A.1. Introduction

Terahertz time-domain spectroscopy (THz-TDS) is an efficacious method for determining materials properties and process control. Short pulses of terahertz radiation probe characterizations as the conductivity of metals in a non-contact manner. Besides security applications where THz-TDS is used to detect bombs, drugs, and weapons [24, 174], THz-TDS has been illustrated as a powerful tool to validate the continuity and possible microscopic defects of fabricated layers [175]. Furthermore, THz-TDS can also be used to detect microorganism as viruses via THz-metamaterials [176] [177]. Metamaterial based lenses [178], and perfect absorbers [127, 179–181] have been characterized with THz-TDS.

We explain the working principle of THz-TDS in a general sense and extract spectral information from the measured time-domain signal. Different material types have been tested to determine their response to an EM wave in a band of 0.3- 2 THz and provide reference data for experiments we perform.

A.2. Time Domain Spectroscopy (TDS)

Time-domain signal measures the transient electric field of a THz pulse and not just the power. This makes it possible to measure the intensity and the phase shift of the THz electromagnetic wave, leading to determining complex dielectric constants and calculating the complex-valued refractive index $n(\omega)$. A schematic of the measurement setup is given in Figure A.1.

The most important part of any THz-TDS system is an ultrashort pulsed laser.

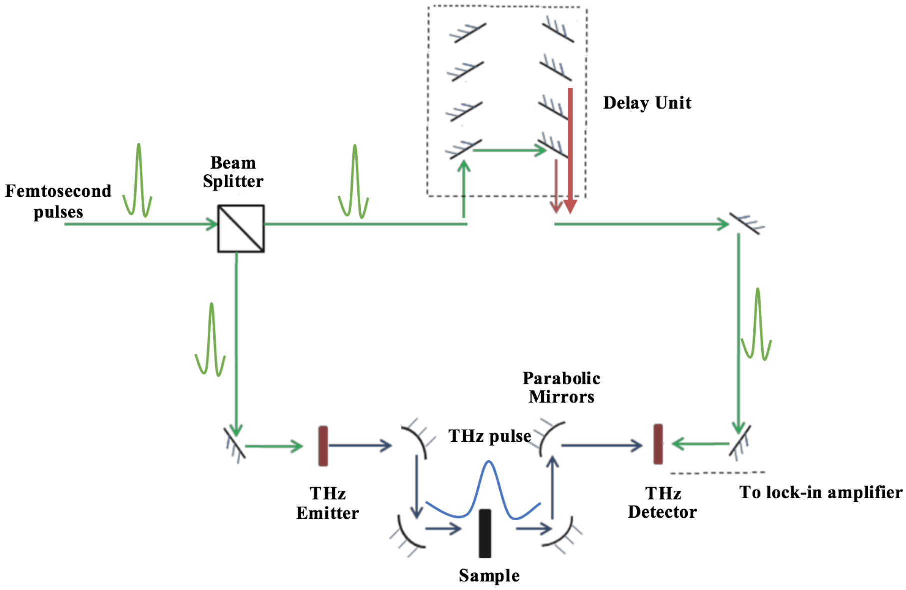

Figure A.1. A basic THz time-domain spectrometer (THz-TDS).

It is used in the terahertz pulse production process. The laser emits optical pulses with femtosecond pulse duration, which are transformed into a picosecond THz pulse using THz emitter (typically low-temperature grown GaAs) as an antenna. Photoconductive antennas are used for both generation and detection of THz waves. As comes from the schematic, the pulse coming out of a femtosecond laser is split into two beams using a beam-splitter: One for the generation of THz radiation and the other as a read-out beam used for identifying THz beam. The basic mechanism for measuring in the time-domain is sampling an unknown THz field with a known femtosecond read-out pulse. This arises by using the convolution of a femtosecond read-out pulse with the picosecond THz pulse. Since the read-out pulse is significantly shorter than the THz pulse, it can be considered a delta-function. To obtain a measured signal, the read-out pulse and the THz pulse should arrive simultaneously. This allows us to measure the THz field as a function of time. The measured signal corresponds to the THz field amplitude at a single point at t_1 time. The read-out pulse relative to the THz pulse should experience an amount of delay to measure all time-points signal. A mechanical delay unit operates the delay. This delay is obtained by increasing the read-out beams' path length to vary the appearance time with respect to the THz signal used for detection. There are position steps in the delay unit that enable us to precise micro-positioning with a computer controller, as shown in Figure A.1. Terahertz pulses are directed from the emitter to the sample and then to the detector by parabolic mirrors. By scanning the delay line, the electric field amplitude and phase of the THz waveform can be mapped out as a function of time. A computer-based program receives the electric field amplitude as a function of time from a digital lock-in amplifier that measures the detector's signal. The system sketched in Figure A.1 uses THz-TDS transmission mode, the simplest one. However, it is also possible to measure the THz pulse in reflection mode. In this case, the angle between antennas should be equal to 90°, and the sample under test should be at the middle with a 45-degree angle concerning antennas. The measured THz transient electric field is Fourier transformed to produce THz pulse in the frequency domain. Fourier transformation is substituted by a discrete Fourier transformation (DFT, or FFT if the fast Fourier transform algorithm is used) for discretized examination data. Figure A.2 shows a measured THz wave in the time domain and tracing FFT in the frequency domain. Afterwards, the complex spectrum can be separated into phase $\phi(\omega)$ and amplitude $A(\omega)$.

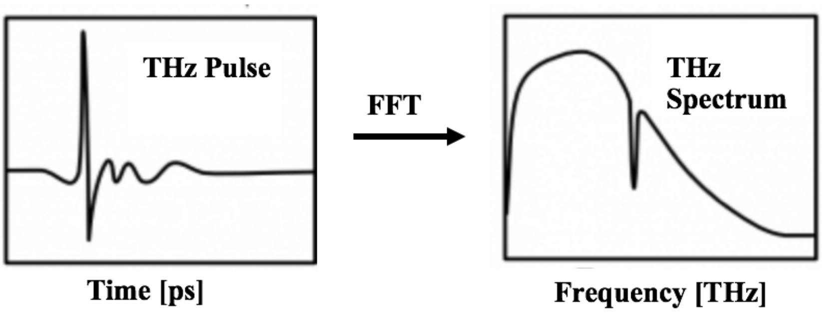

Figure A.2. Measurement result of a THz signal at time-domain transformed to a frequency domain signal by Fast Fourier transformation (FFT).

A.3. Measured References

We characterized the transmitted/ reflected power passing through/ from some selected materials as copper plate, gold plate, Silicon substrate, titanium + quartz substrate, and non-porous CoNi plate. We have calculated S_{11} and S_{12} from exported data. The formulations below determine transmission and reflection coefficient,

$$S_{11} = \frac{E_{rDUT}}{E_{rreference}}, \tag{A.1}$$

$$R = |S_{11}|^2, \tag{A.2}$$

$$S_{12} = \frac{E_{tDUT}}{E_{treference}}, \tag{A.3}$$

$$T = |S_{12}|^2. \tag{A.4}$$

As can be seen from Eq. A.1, E_{rDUT} is the reflected power from device under test and $E_{rreference}$ is the reflected power from a reference plate. In the transmission mode measurements, the reference is air, and we measure the transmitted power through a hole with a diameter of 1mm. In the following, we presented the fast Fourier transformation (FFT)of time-domain signal as raw data for different reference materials.

One can conclude that the amount of transmitted power through metallic plates as gold and copper is zero, as Figure A.3 and Figure A.4 presented. Even a thin Ti layer (200 nm) on quartz substrate eliminates the transmitted power in THz frequencies (see Figure A.5). The transmitted power through a non-porous CoNi layer is zero, shown in Figure 5.18 in Chapter 5. For convenience, we presented Fourier transformed data for a porous sample to compare with a non-porous one. As recorded in Figure A.6, there is a drop in reflected power while THz pulse striking the porous sample.

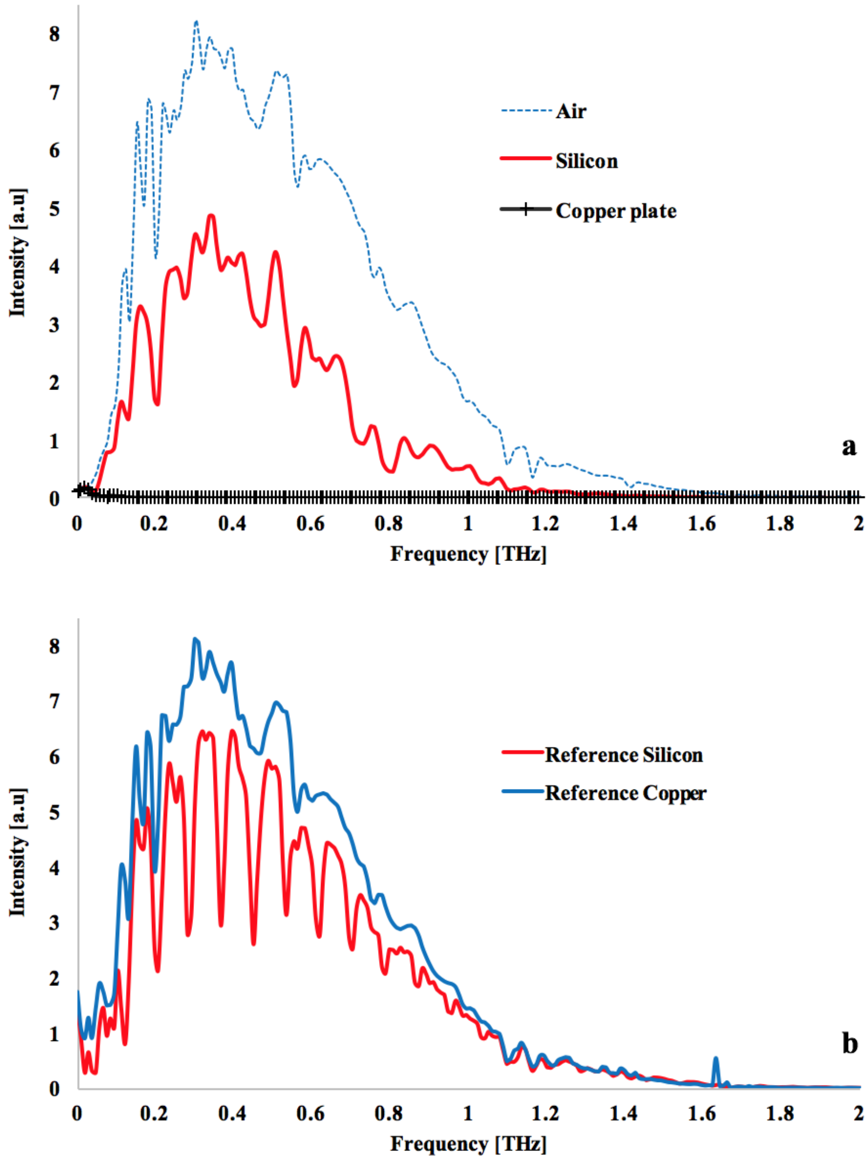

Figure A.3. Fast Fourier transforming the electric field of the THz pulses. (a) Transmitted power through air (blue), a silicon wafer (red), and copper plate (black). (b) Reflected power from a silicon wafer (red) and copper plate (blue).

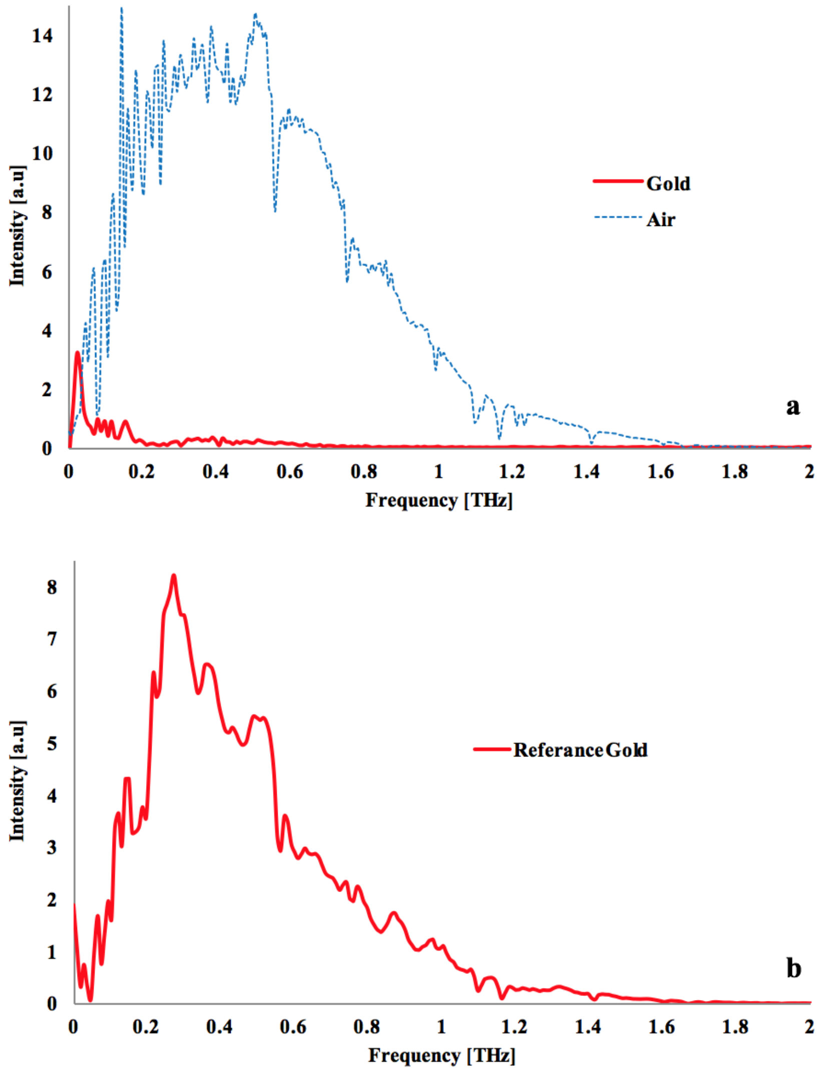

Figure A.4. Fast Fourier transforming the electric field of the THz pulses. (a) Transmitted power through a gold plate (red) and air (blue). (b) Reflected power from a gold plate (red).

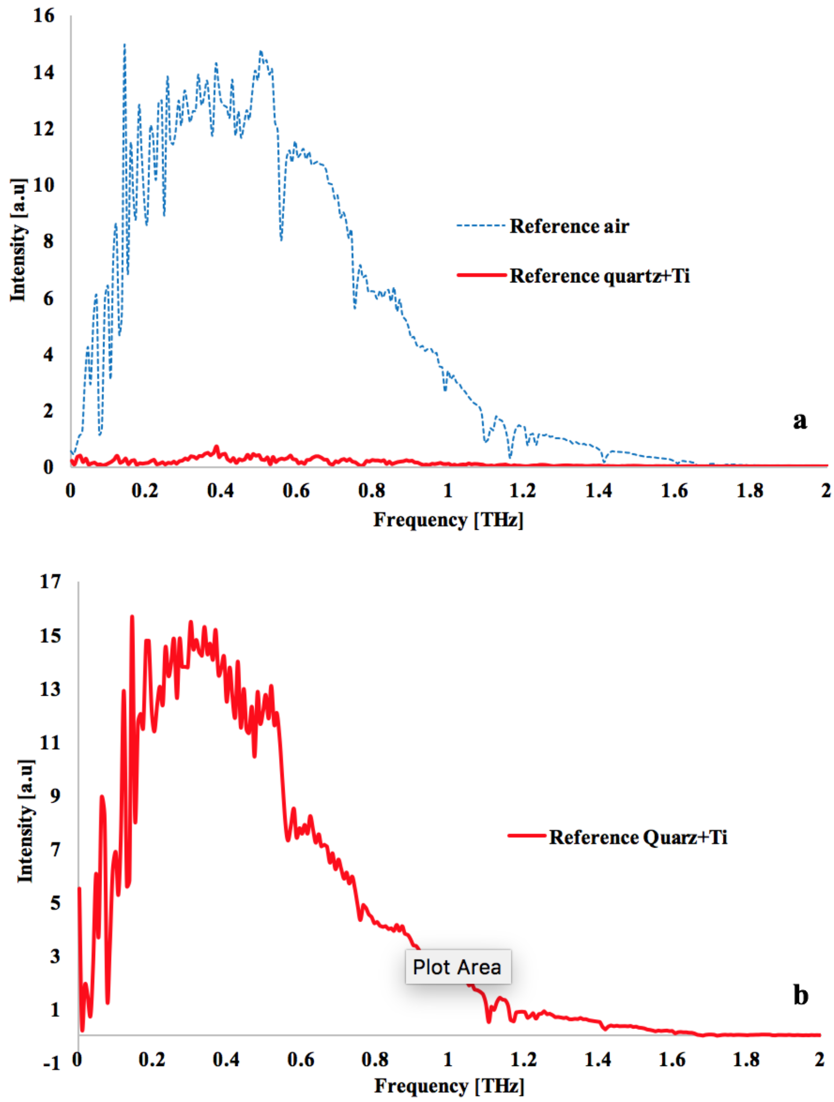

Figure A.5. Fast Fourier transforming the electric field of the THz pulses. (a) Transmitted power through a quartz+Ti plate (red) and air (blue). (b) Reflected power from a quartz+Ti plate (red).

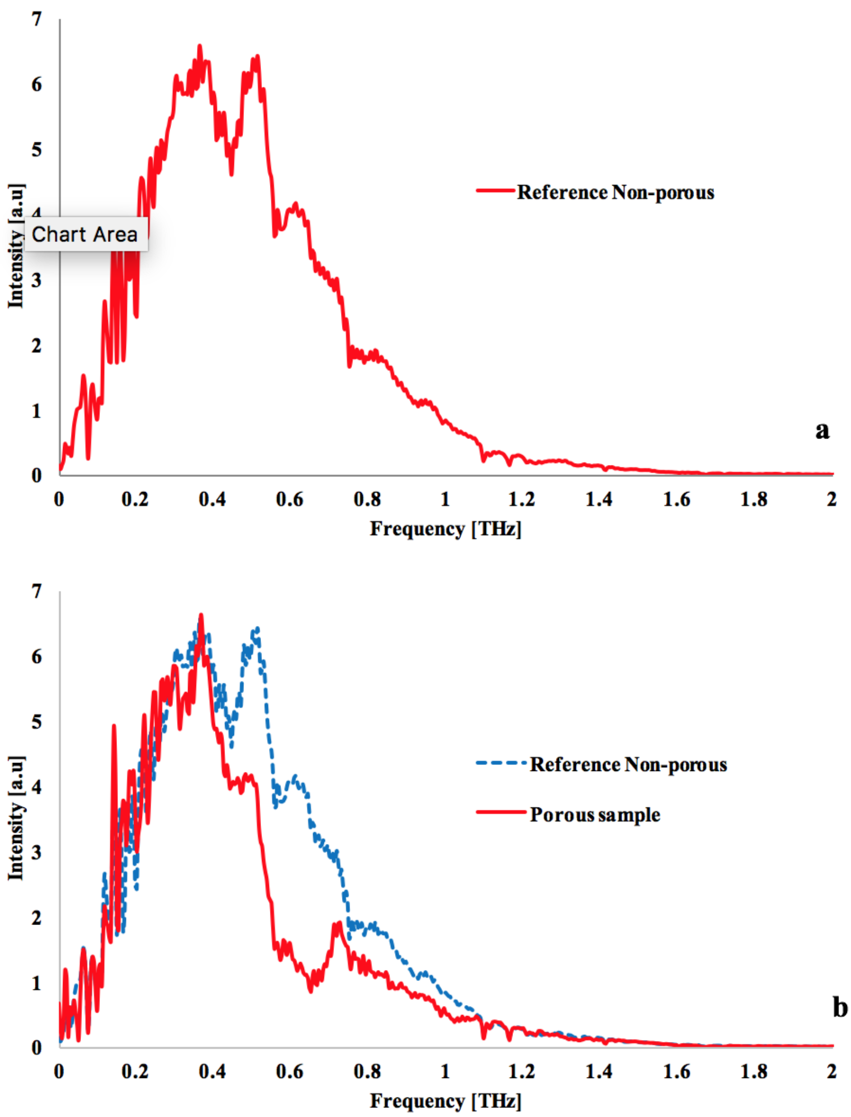

Figure A.6. Fast Fourier transforming the electric field of the THz pulses. (a) Reflected power from a non-porous CoNi plate (red). (b) Reflected power from a porous CoNi sample (red) compared to a non-porous CoNi reference plate (blue).

Figure A.3- Figure A.6 show that the reference measured graphs are not uniform, especially in transmission mode while the material is air. This un-uniformity is because of humidity as water vapor has robust absorption features in the THz range that can interfere with measurements [182].

APPENDIX B: Permissions

B.1. Papers

Dual Band Switchable Metamaterial Electromagnetic Absorber [43]

You are permitted to use the article as you mentioned provided it is cited with acknowledgement to The Electromagnetics Academy.

Bo Zhu, Ci Huang, Yijun Feng, Junming Zhao, and Tian Jiang, "Dual Band Switchable Metamaterial Electromagnetic Absorber," Progress In Electromagnetics Research B, Vol. 24, 121-129, 2010.
doi:10.2528/PIERB10070802
http://www.jpier.org/PIERB/pier.php?paper=10070802
And please make an acknowledgement in each figure caption to read:
[, reproduced courtesy of The Electromagnetics Academy]

Thank you and with our best regards,
--
Editorial and Production Office <work@jpier.org>
Progress in Electromagnetics Research (PIER, PIER B,C,M, PIER Letters)
Suite 207
777 Concord Avenue,
Cambridge, MA 02138, USA
www.jpier.org

Authors Guideline
https://www.jpier.org/Authors/

Figure B.1. Permission letter [43].

Wide-angle infrared absorber based on a negative-index plasmonic metamaterial [45]

American Physical Society
Reuse and Permissions License

07-Mar-2021

This license agreement between the American Physical Society ("APS") and Ayda Mamaghani ("You") consists of your license details and the terms and conditions provided by the American Physical Society and SciPris.

Licensed Content Information

License Number:	**RNP/21/MAR/037318**
License date:	07-Mar-2021
DOI:	10.1103/PhysRevB.79.045131
Title:	Wide-angle infrared absorber based on a negative-index plasmonic metamaterial
Author:	Yoav Avitzour, Yaroslav A. Urzhumov, and Gennady Shvets
Publication:	Physical Review B
Publisher:	American Physical Society
Cost:	USD $ 0.00

Request Details

Does your reuse require significant modifications: No

Specify intended distribution locations:	Turkey
Reuse Category:	Reuse in a thesis/dissertation
Requestor Type:	Student
Items for Reuse:	Figures/Tables
Number of Figure/Tables:	2
Figure/Tables Details:	1)Schematic of the PIMNIM structure. 2)(a) Reflectance, transmittance, and absorbance at normal incidence of a single PIMNIM layer.
Format for Reuse:	Electronic

Information about New Publication:

University/Publisher:	Bogazici university
Title of dissertation/thesis:	Design, Fabrication and Characterization of Micromachined THz Absorbers
Author(s):	Ayda Mamaghani
Expected completion date:	Mar. 2021

License Requestor Information

Name:	Ayda Mamaghani
Affiliation:	Individual
Email Id:	mssida@gmail.com
Country:	Turkey

Figure B.2. Permission letter [45].

High performance optical absorber based on a plasmonic metamaterial [46]

RightsLink Printable License 3/10/21, 10:35 AM

AIP PUBLISHING LICENSE
TERMS AND CONDITIONS

Mar 10, 2021

This Agreement between ayda mamaghani ("You") and AIP Publishing ("AIP Publishing") consists of your license details and the terms and conditions provided by AIP Publishing and Copyright Clearance Center.

License Number	5023640943346
License date	Mar 07, 2021
Licensed Content Publisher	AIP Publishing
Licensed Content Publication	Applied Physics Letters
Licensed Content Title	High performance optical absorber based on a plasmonic metamaterial
Licensed Content Author	Jiaming Hao, Jing Wang, Xianliang Liu, et al
Licensed Content Date	Jun 21, 2010
Licensed Content Volume	96
Licensed Content Issue	25
Type of Use	Thesis/Dissertation
Requestor type	Student
Format	Electronic
Portion	Figure/Table
Number of figures/tables	2
Title	Design, Fabrication and Characterization of Micromachined THz Absorbers
Institution name	Bogazici university
Expected presentation date	Mar 2021
Portions	FIG. 1. a Geometry of the sample FIG. 3. Measured (a) absorbance spectra
Requestor Location	ayda mamaghani buyukcekmece istanbul istanbul, Istanbul 34342 Turkey Attn: ayda mamaghani
Total	0.00 USD

Terms and Conditions

AIP Publishing -- Terms and Conditions: Permissions Uses

AIP Publishing hereby grants to you the non-exclusive right and license to use and/or distribute the Material according to the use specified in your order, on a one-time basis, for the specified term, with a maximum distribution equal to the number that you have ordered.

https://s100.copyright.com/CustomerAdmin/PLF.jsp?ref=e6c8b30a-2041-4963-83df-e8f8bd053b10 Page 1 of 2

Figure B.3. Permission letter [46].

Highly flexible wide angle ofincidence terahertz metamaterial absorber: Design, fabrication, and characterization [54]

American Physical Society
Reuse and Permissions License

07-Mar-2021

This license agreement between the American Physical Society ("APS") and Ayda Mamaghani ("You") consists of your license details and the terms and conditions provided by the American Physical Society and SciPris.

Licensed Content Information

License Number:	**RNP/21/MAR/037319**
License date:	07-Mar-2021
DOI:	10.1103/PhysRevB.78.241103
Title:	Highly flexible wide angle of incidence terahertz metamaterial absorber: Design, fabrication, and characterization
Author:	Hu Tao et al.
Publication:	Physical Review B
Publisher:	American Physical Society
Cost:	USD $ 0.00

Request Details

Does your reuse require significant modifications: No

Specify intended distribution locations:	Turkey
Reuse Category:	Reuse in a thesis/dissertation
Requestor Type:	Student
Items for Reuse:	Figures/Tables
Number of Figure/Tables:	2
Figure/Tables Details:	Figure 1 Terahertz metamaterial absorber consisting of two metallic layers and two dielectric layers. Figure 4 Experimentally measured absorption as a function of frequency for (a) TE and (b) T
Format for Reuse:	Electronic

Information about New Publication:

University/Publisher:	Bogazici university
Title of dissertation/thesis:	Design, Fabrication and Characterization of Micromachined THz Absorbers
Author(s):	Ayda Mamaghani
Expected completion date:	Mar. 2021

License Requestor Information

Name:	Ayda Mamaghani
Affiliation:	Individual
Email Id:	mssida@gmail.com
Country:	Turkey

Figure B.4. Permission letter [54].

A polarization-insensitivebroadband terahertz absorber with a multilayer structure [56]

American Physical Society
Reuse and Permissions License

07-Mar-2021

This license agreement between the American Physical Society ("APS") and Ayda Mamaghani ("You") consists of your license details and the terms and conditions provided by the American Physical Society and SciPris.

Licensed Content Information

License Number:	**RNP/21/MAR/037319**
License date:	07-Mar-2021
DOI:	10.1103/PhysRevB.78.241103
Title:	Highly flexible wide angle of incidence terahertz metamaterial absorber: Design, fabrication, and characterization
Author:	Hu Tao et al.
Publication:	Physical Review B
Publisher:	American Physical Society
Cost:	USD $ 0.00

Request Details

Does your reuse require significant modifications: No

Specify intended distribution locations:	Turkey
Reuse Category:	Reuse in a thesis/dissertation
Requestor Type:	Student
Items for Reuse:	Figures/Tables
Number of Figure/Tables:	2
Figure/Tables Details:	Figure 1 Terahertz metamaterial absorber consisting of two metallic layers and two dielectric layers. Figure 4 Experimentally measured absorption as a function of frequency for (a) TE and (b) T
Format for Reuse:	Electronic

Information about New Publication:

University/Publisher:	Bogazici university
Title of dissertation/thesis:	Design, Fabrication and Characterization of Micromachined THz Absorbers
Author(s):	Ayda Mamaghani
Expected completion date:	Mar. 2021

License Requestor Information

Name:	Ayda Mamaghani
Affiliation:	Individual
Email Id:	mssida@gmail.com
Country:	Turkey

Figure B.5. Permission letter [56].

A micromachined free-standing terahertz absorber with an array of metallic patches [126]

A MEMS-based terahertz detector with metamaterial-based absorber and optical interferometric readout

Author: Habib Bilgin,Shahrzad Zahertar,Seyedehayda Sadeghzadeh,Arda D. Yalcinkaya,Hamdi Torun

Publication: Sensors and Actuators A: Physical

Publisher: Elsevier

Date: 15 June 2016

Journal Author Rights

Please note that, as the author of this Elsevier article, you retain the right to include it in a thesis or dissertation, provided it is not published commercially. Permission is not required, but please ensure that you reference the journal as the original source. For more information on this and on your other retained rights, please visit: https://www.elsevier.com/about/our-business/policies/copyright#Author-rights

BACK CLOSE WINDOW

Figure B.6. Permission letter [126].

A MEMS-Based Terahertz Detector with Metamaterial-Based Absorber and Optical Interferometric Readout [127]

A MEMS-based terahertz detector with metamaterial-based absorber and optical interferometric readout

Author: Habib Bilgin,Shahrzad Zahertar,Seyedehayda Sadeghzadeh,Arda D. Yalcinkaya,Hamdi Torun

Publication: Sensors and Actuators A: Physical

Publisher: Elsevier

Date: 15 June 2016

Journal Author Rights

Please note that, as the author of this Elsevier article, you retain the right to include it in a thesis or dissertation, provided it is not published commercially. Permission is not required, but please ensure that you reference the journal as the original source. For more information on this and on your other retained rights, please visit: https://www.elsevier.com/about/our-business/policies/copyright#Author-rights

BACK CLOSE WINDOW

Figure B.7. Permission letter [127].

REFERENCES

1. Pendry, J., A. Holden, D. Robbins and W. Stewart, "Magnetism from Conductors, and Enhanced Non-linear Phenomena", *Microwave Theory and Techniques, IEEE Transactions on*, Vol. 47, pp. 2075 – 2084, 12 1999.

2. Lim, S., C.Caloz and T.Itoh, "Metamaterial-based electronically controlled transmission-line structure as a novel leaky-wave antenna with tunable radiation angle and beamwidth", *IEEE Transactions on Microwave Theory and Techniques*, Vol. 53, No. 1, pp. 161–173, 2005.

3. Torun, H., S. Sadeghzadeh and A. D. Yalcinkaya, "Note: Tunable overlapping half-ring resonator", *Review of Scientific Instruments*, Vol. 84, No. 10, p. 106107, 2013, `https://doi.org/10.1063/1.4825347`.

4. Landy, N. I., C. M. Bingham, T. Tyler, N. Jokerst, D. R. Smith and W. J. Padilla, "Design, theory, and measurement of a polarization-insensitive absorber for terahertz imaging", *Phys. Rev. B*, Vol. 79, p. 125104, Mar 2009, `https://link.aps.org/doi/10.1103/PhysRevB.79.125104`.

5. Shi, C., X. Zang, Y. Wang, L. Chen, B. Cai and Y. Zhu, "A polarization-independent broadband terahertz absorber", *Applied Physics Letters*, Vol. 105, No. 3, p. 031104, 2014, `https://doi.org/10.1063/1.4890617`.

6. Meng, L., D. Zhao, Q. Li and M. Qiu, "Polarization-sensitive perfect absorbers at near-infrared wavelengths: Erratum", *Opt. Express*, Vol. 21, No. S2, pp. A229–A230, Mar 2013, `http://www.opticsexpress.org/abstract.cfm?URI=oe-21-102-A229`.

7. Lim, J.-H. and S.-S. Kim, "Multiple magnetic resonance and microwave absorption of metamaterial absorbers composed of double split ring resonators on grounded carbonyl iron composites", *AIP Advances*, Vol. 7, No. 12, p. 125223,

2017, https://doi.org/10.1063/1.5013164.

8. Lim, J.-H. and S.-S. Kim, “Multiple magnetic resonance and microwave absorption of metamaterial absorbers composed of double split ring resonators on grounded carbonyl iron composites”, *AIP Advances*, Vol. 7, No. 12, p. 125223, 2017, https://doi.org/10.1063/1.5013164.

9. Alipoor, M. and M. Bahadorzadeh Ghandehari, “High polarization and wide angle independent hexagonal shapes metamaterial absorber”, *2015 International Congress on Technology, Communication and Knowledge (ICTCK)*, pp. 46–50, 2015.

10. Zhu, W., X. Zhao, B. Gong, L. Liu and B. Su, “Optical metamaterial absorber based on leaf-shaped cells”, *Applied Physics A: Materials Science and Processing*, Vol. 102, pp. 147–151, 01 2011.

11. Zou, Y., J. Cao, X. Gong, R. Qian and Z. An, “Ultrathin and Electrically Tunable Metamaterial with Nearly Perfect Absorption in Mid-Infrared”, *Applied Sciences*, Vol. 9, No. 16, p. 3358, Aug 2019, http://dx.doi.org/10.3390/app9163358.

12. “Design of Narrow Discrete Distances of Dual-/Triple-Band Terahertz Metamaterial Absorbers”, *Nanoscale Res Letters*, Vol. 14, p. 64, 2019.

13. Liu, S., H. Chen and T. Cui, “A broadband terahertz absorber using multi-layer stacked bars”, *Applied Physics Letters*, Vol. 106, p. 151601, 04 2015.

14. Wen, D.-e., Y. Helin, Q. Ye, M. Li, L. Guo and J. Zhang, “Broadband metamaterial absorber based on a multi-layer structure”, *Physica Scripta*, Vol. 88, p. 015402, 06 2013.

15. Long, C., S. Yin, W. Wang, W. Li, J. Zhu and J. Guan, “Broadening the absorption bandwidth of metamaterial absorbers by transverse magnetic harmonics of TM210 mode”, *Scientific Reports*, Vol. 6, 02 2016.

16. Ahi, K. and M. Anwar, “Developing terahertz imaging equation and enhancement of the resolution of terahertz images using deconvolution”, *Proc. SPIE 9856, Terahertz Physics, Devices, and Systems X: Advanced Applications in Industry and Defense*, p. 98560N, 05 2016.

17. Armstrong, C. M., “The Truth About Terahertz”, , 08 2012.

18. Karagöz, B., H. Altan and K. Kamburoğlu, “Terahertz pulsed imaging study of dental caries”, *Progress in Biomedical Optics and Imaging - Proceedings of SPIE*, Vol. 9542, 07 2015.

19. Shen, Y.-c., P. Taday and N. Kemp, *Terahertz spectroscopy of explosive materials*, Vol. 5619, pp. 82–89, 12 2004.

20. Huhn, A. K., E. Sáenz, P. de Maagt and P. H. Bolívar, “Broadband Terahertz Analysis of Energetic Materials—Influence of Crystal Structure and Additives”, *IEEE Transactions on Terahertz Science and Technology*, Vol. 3, No. 5, pp. 649–655, 2013.

21. Chen, J., Y. Chen, H. Zhao, G. J. Bastiaans and X.-C. Zhang, “Absorption coefficients of selected explosives and related compounds in the range of 0.1–2.8 THz”, *Opt. Express*, Vol. 15, No. 19, pp. 12060–12067, Sep ts , doi = 10.1364/OE.15.012060,.

22. Trofimov, V. A. and S. A. Varentsova, “High effective time-dependent THz spectroscopy method for the detection and identification of substances with inhomogeneous surface”, *PLOS ONE*, Vol. 13, No. 8, pp. 1–28, 08 2018, `https://doi.org/10.1371/journal.pone.0201297`.

23. Campbell, M. B. and E. J. Heilweil, “Noninvasive detection of weapons of mass destruction using terahertz radiation”, R. J. Hwu and D. L. Woolard (Editors), *Terahertz for Military and Security Applications*, Vol. 5070, pp. 38 – 43, International Society for Optics and Photonics, SPIE, 2003,

https://doi.org/10.1117/12.504297.

24. Federici, J., B. Schulkin, F. Huang, D. Gary, R. Barat, F. Oliveira and D. Zimdars, "THz imaging and sensing for security applications - Explosives, weapons and drugs", *Semiconductor Science and Technology*, Vol. 20, p. S266, 06 2005.

25. Yanwen Jiang, Bin Deng, Yuliang Qin, Hongqiang Wang, Ye Zhang and Xiaoyu Yang, "Experimental results of concealed object imaging using Terahertz radar", *2017 International Workshop on Electromagnetics: Applications and Student Innovation Competition*, pp. 16–17, 2017.

26. Danciu, M., T. Alexa, C. Stefanescu, G. Dodi, B. Tamba, C. T. Mihai, G. Stanciu, A. Luca, I. Spiridon, L. Ungureanu, V. Ianole, I. Ciortescu, C. Mihai, G. Stefanescu, I. Chirila, R. Ciobanu and V. Drug, "Terahertz Spectroscopy and Imaging: A Cutting-Edge Method for Diagnosing Digestive Cancers", *Materials*, Vol. 12, p. 1519, 05 2019.

27. Yang, X., X. Zhao, K. Yang, Y.-P. Liu, Y. Liu, W. Fu and Y. Luo, "Biomedical Applications of Terahertz Spectroscopy and Imaging", *Trends in Biotechnology*, Vol. 34, 05 2016.

28. Fan, S., Y. He, B. Ung and E. Pickwell-MacPherson, "The growth of biomedical terahertz research", *Journal of Physics D: Applied Physics*, Vol. 47, p. 374009, 08 2014.

29. Veselago, V., "Electrodynamics of substa simultaneously negative electrical and magnetic properties", *Soviet Physics Uspekhi*, p. 509–517, 1968.

30. Veselago, V., L. Braginsky, V. Shklover and C. Hafner, "Negative Refractive Index Materials", *Journal of Computational and Theoretical Nanoscience*, Vol. 3, pp. 189–218, 04 2006.

31. Qu, J., K. Muamer, A. Naber and M. Wegener, "Micro-Structured Two-

Component 3D Metamaterials with Negative Thermal-Expansion Coefficient from Positive Constituents", *Scientific Reports*, Vol. 7, 10 2016.

32. Kern, C., G. W. Milton, M. Kadic and M. Wegener, "Theory of the Hall effect in three-dimensional metamaterials", *New Journal of Physics*, Vol. 20, No. 8, p. 083034, aug 2018.

33. Pendry, J. B., "Negative Refraction Makes a Perfect Lens", *Phys. Rev. Lett.*, Vol. 85, pp. 3966–3969, Oct 2000, `https://link.aps.org/doi/10.1103/PhysRevLett.85.3966`.

34. Sadeghzadeh, S., *Split Ring Resonator and Metamaterials at Microwave Regime, Numerical Analysis, Design, Characterization*, Master's Thesis, Bogazici University, 2012.

35. Khuyen, B., B. Tung, D. Nguyen, Y. J. Yoo, Y. Kim, W. Kim, V. Lam, J. Yang and Y. Lee, "Size-efficient metamaterial absorber at low frequencies: Design, fabrication, and characterization", *Journal of Applied Physics*, Vol. 117, p. 243105, 06 2015.

36. Eleftheriades, G. V., "EM transmission-line metamaterials", *Materials Today*, Vol. 12, No. 3, pp. 30 – 41, 2009, `http://www.sciencedirect.com/science/article/pii/S1369702109700732`.

37. Mishra, R. K., R. D. Gupta and S. Datar, "Metamaterial Absorber (MMA) In X-Band, For Stealth Applications", *2019 URSI Asia-Pacific Radio Science Conference (AP-RASC)*, pp. 1–1, 2019.

38. Rufangura, P. and C. Sabah, "Dual-band perfect metamaterial absorber for solar cell applications", *Vacuum*, Vol. 120, pp. 68 – 74, 2015, `http://www.sciencedirect.com/science/article/pii/S0042207X15002535`, sATF 2014: Science and Application of Thin Films, Conference Exhibition.

39. Abdulkarim, Y., O. Altintas, M. Karaaslan and E. Unal, “Metamaterial absorber sensor design by incorporating swastika shaped resonator to determination of the liquid chemicals depending on electrical characteristics”, *Physica E Low-Dimensional Systems and Nanostructures*, 06 2019.

40. Shen, Y., Y. Pang, J. Wang, H. Ma, Z. Pei and S. Qu, “Origami-inspired metamaterial absorbers for improving the larger-incident angle absorption”, *Journal of Physics D: Applied Physics*, Vol. 48, p. 445008, 11 2015.

41. Landy, N., S. Sajuyigbe, J. Mock, D. Smith and W. Padilla, “Perfect Metamaterial Absorber”, *Physical Review Letters*, Vol. 100, p. 207402, 05 2008.

42. García-García, J., F. Martín, J. Baena, R. Marques and L. Jelinek, “On the resonances and polarizabilities of split ring resonators”, *Journal of Applied Physics*, Vol. 98, 08 2005.

43. Zhu, B., C. Huang, Y. Feng, J. Zhao and T. Jiang, “Dual band switchable metamaterial electromagnetic absorber”, *Progress In Electromagnetics Research B*, Vol. 24, pp. 121–129, 01 2010.

44. Bilotti, F. and A. Toscano, “Design of Spiral and Multiple Split-Ring Resonators for the Realization of Miniaturized Metamaterial Samples”, *Antennas and Propagation, IEEE Transactions on*, Vol. 55, pp. 2258 – 2267, 09 2007.

45. Avitzour, Y., Y. Urzhumov and G. Shvets, “Wide-Angle Infrared Absorber Based on a Negative Index Plasmonic Metamaterial”, *Physical Review B*, Vol. 79, 08 2008.

46. Hao, J., X. Liu, W. Padilla, L. Zhou and M. Qiu, “High Performance Optical Absorber Based on a Plasmonic Metamaterial”, *Applied Physics Letters*, Vol. 96, pp. 251104 – 251104, 07 2010.

47. Gansel, J., M. Wegener, S. Burger and S. Linden, “Gold helix photonic metama-

terials: A numerical parameter study", *Optics Express*, Vol. 18, pp. 1059–69, 01 2010.

48. Li, W., Z. Coppens, L. Vazquez Besteiro, W. Wang, A. Govorov and J. Valentine, "Circularly Polarized Light Detection with Hot Electrons in Chiral Plasmonic Metamaterials", *Nature Communications*, Vol. 6, p. 8379, 09 2015.

49. Wang, Z., H. Jia, K. Yao, W. Cai, H. Chen and Y. Liu, "Circular Dichroism Metamirrors with Near-Perfect Extinction", *ACS Photonics*, Vol. 3, 09 2016.

50. Ma, X., M. Pu, X. Li, Y. Guo, P. Gao and X. Luo, "Meta-Chirality: Fundamentals, Construction and Applications", *Nanomaterials*, Vol. 7, 05 2017.

51. Ouyang, L., W. Wang, D. Rosenmann, D. Czaplewski, J. Gao and X. Yang, "Near-infrared chiral plasmonic metasurface absorbers", *Optics Express*, Vol. 26, p. 31484, 11 2018.

52. Watts, C., X. Liu and W. Padilla, "Metamaterial Electromagnetic Wave Absorbers", *Advanced Materials (Deerfield Beach, Fla.)*, Vol. 24, pp. OP98–120, OP181, 06 2012.

53. Tao, H., N. Landy, C. Bingham, X. Zhang, R. Averitt and W. Padilla, "A metamaterial absorber for the terahertz regime: Design, fabrication and characterization", *Optics Express*, Vol. 16, pp. 7181–8, 05 2008.

54. Tao, H., C. Bingham, A. Strikwerda, D. Pilon, D. Shrekenhamer, N. Landy, K. Fan, X. Zhang, W. Padilla and R. Averitt, "Highly flexible wide angle of incidence terahertz metamaterial absorber: Design, fabrication, and characterization", *Physical Review B*, Vol. 78, p. 241103(R), 12 2008.

55. Huang, L., D. Roy Chowdhury, S. Ramani, M. Reiten, S.-N. Luo, A. Taylor and H.-T. Chen, "Experimental demonstration of terahertz metamaterial absorbers with a broad and flat high absorption band", *Optics Letters*, Vol. 37, pp. 154–6,

01 2012.

56. Feng, Z., J.-X. Liu, J. Yang, H. Zhang and H.-M. Li, "A polarization-insensitive broadband terahertz absorber with a multilayer structure", *Results in Physics*, Vol. 11, 11 2018.

57. Zhong, M., X. Jiang, X. Zhu, J. Zhang and J. Zhong, "Design and fabrication of a single metal layer tunable metamaterial absorber in THz range", *Optics Laser Technology*, Vol. 125, p. 106023, 2020, `http://www.sciencedirect.com/science/article/pii/S0030399219319747`.

58. Cen, C., Z. Yi, G. Zhang, Y. Zhang, C. Liang, X. Chen, Y. Tang, X. Ye, Y. Yi, J. Wang and J. hua, "Theoretical design of a triple-band perfect metamaterial absorber in the THz frequency range", *Results in Physics*, Vol. 14, p. 102463, 06 2019.

59. Pang, Y., H. Cheng and Y. Zhou, "Double-corrugated metamaterial surfaces for broadband microwave absorption", *Journal of Applied Physics*, Vol. 113, 02 2013.

60. Hao, J., E. Lheurette, L. Burgnies, E. Okada and D. Lippens, "Bandwidth enhancement in disordered metamaterial absorbers", *Applied Physics Letters*, Vol. 105, pp. 081102–081102, 08 2014.

61. Han, N., Z. Chen, C. Lim, B. Ng and M. Hong, "Broadband multi-layer terahertz metamaterials fabrication and characterization on flexible substrates", *Optics express*, Vol. 19, pp. 6990–8, 04 2011.

62. Liang, L., B. Jin, J. Wu, Y. Huang, Z. Ye, X. Huang, D. Zhou, G. Wang, X. Jia, H. Lu, L. Kang, W. Xu, J. Chen and P. Wu, "A flexible wideband bandpass terahertz filter using multi-layer metamaterials", *Applied Physics B*, Vol. 113, 05 2013.

63. Liu, S., H. Chen and T. Cui, "A broadband terahertz absorber using multi-layer

stacked bars", *Applied Physics Letters*, Vol. 106, p. 151601, 04 2015.

64. Bai, J., S. Zhang, F. Fan, S. Wang, X. Sun, Y. Miao and S. Chang, "Tunable broadband THz absorber using vanadium dioxide metamaterials", *Optics Communications*, Vol. 452, 07 2019.

65. Zang, X., C. Shi, L. Chen, B. Cai, Y. Zhu and S. Zhuang, "Ultra-broadband terahertz absorption by exciting the orthogonal diffraction in dumbbell-shaped gratings", *Scientific reports*, Vol. 5, p. 8901, 03 2015.

66. Kenney, M., J. Grant, Y. Shah, I. Escorcia Carranza, M. Humphreys and D. Cumming, "Octave-Spanning Broadband Absorption of Terahertz Light Using Metasurface Fractal-Cross Absorbers", *ACS Photonics*, Vol. 4, pp. 2604–2612, 10 2017.

67. Richter, J. R., B. B. Kasten and K. R. Zinn, "31 - Imaging and Adenoviral Gene Therapy", D. T. Curiel (Editor), *Adenoviral Vectors for Gene Therapy (Second Edition)*, pp. 767 – 802, Academic Press, San Diego, second edition edn., 2016, `http://www.sciencedirect.com/science/article/pii/B9780128002766000310`.

68. NASA, "NASA's Lunar Reconnaissance", `https://lunar.gsfc.nasa.gov/index.html`, online; accessed 20 January 2020.

69. Vollmer, M. and K.-P. Möllmann, *Infrared Thermal Imaging: Fundamentals, Research and Applications, 2nd Edition*, Wiley, 2018.

70. Kong, S., D. Wijngaards and R. Wolffenbuttel, "Infrared Micro-spectrometer Based on a Diffraction Grating", *Sensors and Actuators A: Physical*, Vol. 92, pp. 88–95, 08 2001.

71. Piazza, R. and V. Degiorgio, "Scattering, Rayleigh", F. Bassani, G. L. Liedl and P. Wyder (Editors), *Encyclopedia of Condensed Matter Physics*, pp. 234–242, Elsevier, Oxford, 2005, `https://www.sciencedirect.com/science/article/pii/B0123694019006483`.

72. Nelson, D., "Polarized Vs Non Polarized Sunglasses: The Science Behind Polarization", *Science Trends*, 10 2018.

73. Staelin, D., *Electromagnetics and Applications*, pp. 30–31, Massachusetts Institute of Technology: MIT OpenCourseWare, Dordrecht, 2009.

74. Smith, D. R., W. J. Padilla, D. C. Vier, R. Shelby, S. C. Nemat-Nasser, N. Kroll and S. Schultz, *Left-Handed Metamaterials*, pp. 351–371, Springer Netherlands, Dordrecht, 2001, `https://doi.org/10.1007/978-94-010-0738-2`$_2$5.

75. Beckers, M., B. Weise, S. Kalapis, T. Gries, G. Seide and C.-A. Bunge, "2 - Basics of light guidance", C.-A. Bunge, T. Gries and M. Beckers (Editors), *Polymer Optical Fibres*, pp. 9 – 46, Woodhead Publishing, 2017, `http://www.sciencedirect.com/science/article/pii/B9780081000397000026`.

76. Leong, K., A. Lai and T. Itoh, "Demonstration of reverse Doppler effect using a left-handed transmission line", *Microwave and Optical Technology Letters*, Vol. 48, pp. 545 – 547, 03 2006.

77. Lakhtakia, A., "Positive and Negative Goos-Hanchen Shifts and Negative Phase–Velocity Mediums (alias Left-Handed Materials)", *International Journal of Electronics and Communications*, Vol. 58, 06 2003.

78. Smith, D., J. Pendry and M. Wiltshire, "Metamaterials and Negative Refractive Index", *Science (New York, N.Y.)*, Vol. 305, pp. 788–92, 09 2004.

79. Caloz, C. and T. Itoh, *Electromagnetic Metamaterials: Transmission Line Theory and Microwave Applications*, John Wiley Sons, Fundamentals of LH MTMs, 2006.

80. Veselago, V., L. Braginsky, V. Shklover and C. Hafner, "Negative Refractive Index Materials", *Journal of Computational and Theoretical Nanoscience*, Vol. 3, pp. 189–218, 04 2006.

81. Lvovsky, A. I., “Fresnel Equation”, *Encyclopedia of Optical Engineering*, pp. 1–6, 02 2013.

82. Antonets, I., L. Kotov, V. Shavrov and V. Shcheglov, “Reflection, transmission, and absorption coefficients calculated for the oblique incidence of an electromagnetic wave on a plate”, *Journal of Communications Technology and Electronics*, Vol. 53, pp. 363–376, 04 2008.

83. Caloz, C. and T. Itoh, “Positive/Negative Refractive Index Anisotropic 2-D Metamaterials”, *Microwave and Wireless Components Letters, IEEE*, Vol. 13, pp. 547 – 549, 01 2004.

84. Eleftheriades, G. V., A. K. Iyer and P. C. Kremer, “Planar negative refractive index media using periodically L-C loaded transmission lines”, *IEEE Transactions on Microwave Theory and Techniques*, Vol. 50, No. 12, pp. 2702–2712, 2002.

85. Baena, J. D., J. Bonache, F. Martin, R. M. Sillero, F. Falcone, T. Lopetegi, M. A. G. Laso, J. Garcia-Garcia, I. Gil, M. F. Portillo and M. Sorolla, “Equivalent-circuit models for split-ring resonators and complementary split-ring resonators coupled to planar transmission lines”, *IEEE Transactions on Microwave Theory and Techniques*, Vol. 53, No. 4, pp. 1451–1461, 2005.

86. Levi, A. F. J., “The Drude model”, *Essential Classical Mechanics for Device Physics*, 2053-2571, pp. 6–1 to 6–20, Morgan Claypool Publishers, 2016, `http://dx.doi.org/10.1088/978-1-6817-4413-1ch6`.

87. Brown, J., “Artificial dielectrics having refractive indices less than unity”, *Proceedings of the IEE - Part IV: Institution Monographs*, Vol. 100, pp. 51 – 62, 11 1953.

88. Jaksic, Z., N. Dalarsson and M. Maksimovic, “Negative Refractive Index Metamaterials: Principles and Applications”, *Microwave Review*, Vol. 12, 04 2006.

89. Banerjee, B., *An Introduction to Metamaterials and Waves in Composites*, CRC Press.s, Electrodynamic Metamaterials, 2011.

90. Pugliese, A., *Metamaterial Employment for the Reduction of LHC Collimators Coupling Impedance Contribution: Study, Planning and M E Asurements of Innovative Structures*, Laurea thesis, U. Naples, 2017.

91. Padilla, W., D. Smith and D. Basov, "Spectroscopy of metamaterials from infrared to optical frequencies", *JOSA B*, Vol. 23, 03 2006.

92. Baena, J. D., R. Marqués, F. Medina and J. Martel, "Artificial magnetic metamaterial design by using spiral resonators", *Phys. Rev. B*, Vol. 69, p. 014402, Jan 2004, `https://link.aps.org/doi/10.1103/PhysRevB.69.014402`.

93. Chen, H., L. Ran, J. Huangfu, X. Zhang, K. Chen, T. M. Grzegorczyk and J. Au Kong, "Left-handed materials composed of only S-shaped resonators", *Phys. Rev. E*, Vol. 70, p. 057605, Nov 2004, `https://link.aps.org/doi/10.1103/PhysRevE.70.057605`.

94. Demetriadou, A. and J. Pendry, "Numerical analysis of Swiss roll metamaterials", *Journal of physics. Condensed matter : an Institute of Physics Journal*, Vol. 21, p. 326006, 08 2009.

95. Ziolkowski, R. and E. Heyman, "Wave Propagation in Media Having Negative Permittivity and Permeability", *Physical Review. E, Statistical, nonlinear, and soft matter physics*, Vol. 64, p. 056625, 12 2001.

96. Lindell, I., S. Tretyakov, K. Nikoskinen and S. Ilvonen, "BW media—Media with negative parameters, capable of supporting backward waves", *Microwave and Optical Technology Letters*, Vol. 31, pp. 129 – 133, 10 2001.

97. Valanju, P., R. Walser and A. Valanju, "Wave Refraction in Negative-Index Media: Always Positive and Very Inhomogeneous", *Physical Review Letters*, Vol. 88,

p. 187401, 06 2002.

98. Mccall, M., A. Lakhtakia and W. Weiglhofer, “The negative index of refraction demystified”, *European Journal of Physics*, Vol. 23, 04 2002.

99. Yen, T. J., W. J. Padilla, N. Fang, D. C. Vier, D. R. Smith, J. B. Pendry, D. N. Basov and X. Zhang, “Terahertz Magnetic Response from Artificial Materials”, *Science*, Vol. 303, No. 5663, pp. 1494–1496, 2004, `https://science.sciencemag.org/content/303/5663/1494`.

100. Ebrahimi, A., W. Withayachumnankul, S. Al-Sarawi and D. Abbott, “Microwave microfluidic sensor for determination of glucose concentration in water”, pp. 1–3, 11 2015.

101. Albishi, A. and O. Ramahi, “Detection of Surface and Subsurface Cracks in Metallic and Non-Metallic Materials Using a Complementary Split-Ring Resonator”, *Sensors (Basel, Switzerland)*, Vol. 14, pp. 19354–19370, 10 2014.

102. Horestani, A. K., J. Naqui, D. Abbott, C. Fumeaux and F. Martín, “Two-dimensional displacement and alignment sensor based on reflection coefficients of open microstrip lines loaded with split ring resonators”, *Electronics Letters*, Vol. 50, No. 8, pp. 620–622, 2014.

103. Elhawil, A., J. Stiens, C. De Tandt, W. Ranson and R. Vounckx, “Thin-film sensing using circular split-ring resonators at mm-wave frequencies”, *Applied Physics A*, Vol. 103, pp. 623–626, 06 2011.

104. Torun, H., S. Sadeghzadeh and A. Yalcinkaya, “Note: Tunable overlapping half-ring resonator”, *The Review of scientific instruments*, Vol. 84, p. 106107, 10 2013.

105. Poole, C. and I. Darwazeh, “Chapter 6 - S-parameters”, C. Poole and I. Darwazeh (Editors), *Microwave Active Circuit Analysis and Design*, pp. 167 – 204, Academic Press, Oxford, 2016,

http://www.sciencedirect.com/science/article/pii/B9780124078239000068.

106. Ahamed, E., M. R. Faruque, M. Mansor and M. Islam, "Polarization-dependent tunneled metamaterial structure with enhanced fields properties for X-band application", *Results in Physics*, Vol. 15, p. 102530, 07 2019.

107. Sellier, A., T. Teperik and A. de Lustrac, "Resonant circuit model for efficient metamaterial absorber", *Optics express*, Vol. 21 Suppl 6, pp. A997–A1006, 11 2013.

108. Tsuchiya, A. and H. Onodera, "Impact of anomalous skin effect on metal wire for terahertz integrated circuit", *2015 IEEE International Symposium on Radio-Frequency Integration Technology (RFIT)*, pp. 217–219, 2015.

109. Welsby, V., *The Theory and Design of Inductance Coils*, p. 40–44, John Wiley and Sons, Inc., 1960.

110. Luo, H., Y. Cheng and R. Gong, "Numerical study of metamaterial absorber and extending absorbance bandwidth base on multi square patches", *The European Physical Journal B - Condensed Matter and Complex Systems*, Vol. 81, pp. 387–392, 06 2011.

111. Liu, X., S. Macnaughton, D. Shrekenhamer, H. Tao, S. Selvarasah, A. Totachawattana, R. Averitt, M. Dokmeci, S. Sonkusale and W. Padilla, "Metamaterials on parylene thin film substrates: Design, fabrication, and characterization at terahertz frequency", *Applied Physics Letters*, Vol. 96, pp. 011906–011906, 01 2010.

112. Sebastian, M. T., "Measurement of Microwave Dielectric Properties and Factors Affecting Them", *Dielectric Materials for Wireless Communication*, pp. 11 – 47, Elsevier, Amsterdam, 2008, http://www.sciencedirect.com/science/article/pii/B9780080453309000029.

113. Fan, K., J. Y. Suen, X. Liu and W. J. Padilla, "All-

dielectric metasurface absorbers for uncooled terahertz imaging", *Optica*, Vol. 4, No. 6, pp. 601–604, Jun 2017, http://www.osapublishing.org/optica/abstract.cfm?URI=optica-4-6-601.

114. Federici, J., D. Gary, R. Barat and D. Zimdars, "THz standoff detection and imaging of explosives and weapons", *Proceedings of SPIE - The International Society for Optical Engineering*, Vol. 75, 03 2005.

115. Xu, W., L. Xie and Y. Ying, "Mechanisms and Applications of Terahertz Metamaterial Sensing: a Review", *Nanoscale*, Vol. 9, 08 2017.

116. Alves, F., D. Grbovic, B. Kearney, N. V. Lavrik and G. Karunasiri, "Bi-material terahertz sensors using metamaterial structures", *Opt. Express*, Vol. 21, No. 11, pp. 13256–13271, Jun 2013, http://www.opticsexpress.org/abstract.cfm?URI=oe-21-11-13256.

117. Tao, H., A. Strikwerda, K. Fan, W. Padilla, X. Zhang and R. Averitt, "MEMS Based Structurally Tunable Metamaterials at Terahertz Frequencies", *Journal of Infrared, Millimeter, and Terahertz Waves*, Vol. 32, pp. 580–595, 05 2011.

118. Suzuki, T., M. Sekiya, T. Sato and Y. Takebayashi, "Negative refractive index metamaterial with high transmission, low reflection, and low loss in the terahertz waveband", *Optics Express*, Vol. 26, p. 8314, 04 2018.

119. Ling, F., Z. Zhong, Y. Zhang, R. Huang and B. Zhang, "Broadband negative-refractive index terahertz metamaterial with optically tunable equivalent-energy level", *Optics Express*, Vol. 26, p. 30085, 11 2018.

120. Suzuki, T. and S. Kondoh, "Negative refractive index metasurface in the 20-THz band", *Optical Materials Express*, Vol. 8, p. 1916, 07 2018.

121. Ni, B., Z. Wang, R. Zhao, X. Ma, Z. Xing, L. Yang, L. Huang, Y. Lin and D. Zhang, "Realisation of a humidity sensor based on perfect metamaterial ab-

sorber", *Optical and Quantum Electronics*, Vol. 49, 01 2017.

122. Ling, X., Z. Xiao and X. Zheng, "Tunable terahertz metamaterial absorber and the sensing application", *Journal of Materials Science: Materials in Electronics*, Vol. 29, 10 2017.

123. Shchegolkov, D. Y., A. K. Azad, J. F. O'Hara and E. I. Simakov, "Perfect subwavelength fishnetlike metamaterial-based film terahertz absorbers", *Phys. Rev. B*, Vol. 82, p. 205117, Nov 2010, `https://link.aps.org/doi/10.1103/PhysRevB.82.205117`.

124. Maier, T. and H. Brückl, "Wavelength-tunable microbolometers with metamaterial absorbers", *Opt. Lett.*, Vol. 34, No. 19, pp. 3012–3014, Oct 2009, `http://ol.osa.org/abstract.cfm?URI=ol-34-19-3012`.

125. Hall, N. A. and F. L. Degertekin, "Integrated optical interferometric detection method for micromachined capacitive acoustic transducers", *Applied Physics Letters*, Vol. 80, No. 20, pp. 3859–3861, 2002.

126. Torun, H., S. Sadeghzadeh, H. Bilgin and A. Yalcinkaya, "A micromachined freestanding terahertz absorber with an array of metallic patches", *AIP Advances*, Vol. 6, p. 035323, 03 2016.

127. Bilgin, H., S. Zahertar, S. Sadeghzadeh, A. Yalcinkaya and H. Torun, "A MEMS-Based Terahertz Detector with Metamaterial-Based Absorber and Optical Interferometric Readout", *Sensors and Actuators A: Physical*, Vol. 244, 04 2016.

128. SCS Coating Inc., "Parylene Properties Chart", `https://scscoatings.com/corporate/technical-library`, 2013, online; accessed 1 January 2020.

129. Para Tech Coating, Inc., "Parylene Properties Chart", `https://www.parylene.com/Parylene-Technology/Specifications-Properties`,

2010, online; accessed 1 January 2020.

130. Lim, D. and S. Lim, "Three-Dimensional Printed Stair-Like Metamaterial Absorber", *2018 International Symposium on Antennas and Propagation (ISAP)*, pp. 1–2, 2018.

131. Cui, T. J., Xiao Yang Zhou and H. F. Ma, "Three-dimensional metamaterial lens antennas", *Proceedings of the 5th European Conference on Antennas and Propagation (EUCAP)*, pp. 3301–3303, 2011.

132. Wang, A., S. Qu, B. Wang, G. Zhang, C. Xu and H. Dai, "A Three-dimensional Resistive Metamaterial with Extremely Broadband Absorption", *2019 Cross Strait Quad-Regional Radio Science and Wireless Technology Conference (CSQRWC)*, pp. 1–3, 2019.

133. Pan, W., X. Yu, J. Zhang and W. Zeng, "A Novel Design of Broadband Terahertz Metamaterial Absorber Based on Nested Circle Rings", *IEEE Photonics Technology Letters*, Vol. 28, No. 21, pp. 2335–2338, 2016.

134. Liu, H., K. Luo, D. Peng and L.-C. Tu, "Ultra-wideband THz/IR Metamaterial Absorber based on Doped Silicon", , 09 2018.

135. Zheng, H., X. Jin, J. Park, Y. Lu, J. Rhee, W. Jang, H. Cheong and Y. Lee, "Tunable dual-band perfect absorbers based on extraordinary optical transmission and Fabry-Perot cavity resonance", *Optics express*, Vol. 20, pp. 24002–9, 10 2012.

136. Shen, Y., Z. Pei, Y. Pang, J. Wang, A. Zhang and S. Qu, "An extremely wideband and lightweight metamaterial absorber", *Journal of Applied Physics*, Vol. 117, p. 224503, 06 2015.

137. Wang, B., J. Zhou, T. Koschny and C. Soukoulis, "Nonplanar Chiral Metamaterials with Negative Index", *Applied Physics Letters*, Vol. 94, 07 2009.

138. Gansel, J., M. Wegener, S. Burger and S. Linden, “Gold helix photonic metamaterials: A numerical parameter study”, *Optics express*, Vol. 18, pp. 1059–69, 01 2010.

139. Amireddy, K., K. Balasubramaniam and P. Rajagopal, “Porous metamaterials for deep sub-wavelength ultrasonic imaging”, *Applied Physics Letters*, Vol. 113, p. 124102, 09 2018.

140. Armstrong, E. and C. O’Dwyer, “Artificial Opal Photonic Crystals and Inverse Opal Structures – Fundamentals and Applications from Optics to Energy Storage”, *Journal of Materials Chemistry*, Vol. 3, pp. 6109–6143, 06 2015.

141. Li, W., L. Lin, C. Li, Y. Wang and J. Zhang, “Radar absorbing combinatorial metamaterial based on silicon carbide/carbon foam material embedded with split square ring metal”, *Results in Physics*, Vol. 12, 11 2018.

142. Yue, H. H., F. Z. Hai, L. W. Ling, S. Wei and Y. M. Chen, “A Novel Broadband Absorber With Honeycomb Lattices Based on the Flexible Metamaterial”, *2016 Progress in Electromagnetic Research Symposium (PIERS)*, pp. 1916–1918, 2016.

143. Zhang, Y., “Synthesis, Structure and Magnetic Properties of CoNi Submicrospherical Chains”, *Advances in Materials Physics and Chemistry*, Vol. 1, pp. 7–13, 01 2011.

144. Li, N., C. Hu and M. Cao, “Enhanced microwave absorbing performance of CoNi alloy nanoparticles anchored on a spherical carbon monolith”, *Physical chemistry chemical physics : PCCP*, Vol. 15, 04 2013.

145. Hilfiker, J. N., Y. B. Zhang and J. A. Woollam, “Optical property influence on magneto-optics of CoNi and TbCo multilayers on noble metal alloy substrates”, *IEEE Transactions on Magnetics*, Vol. 30, No. 6, pp. 4437–4439, 1994.

146. Sun, G., H. Wu, Q. Liao and Y. Zhang, “Enhanced microwave absorption per-

formance of highly dispersed CoNi nanostructures arrayed on graphene", *Nano Research*, Vol. 11, 11 2017.

147. Hu, M.-J., Y. Lu, S. Zhang, S. Guo, B. Lin, M. Zhang and S.-H. Yu, "High Yield Synthesis of Bracelet-Like Hydrophilic NiCo Magnetic Alloy Flux-Closure Nanorings", *Journal of the American Chemical Society*, Vol. 130, pp. 11606–7, 10 2008.

148. Xu, Q., Z.-J. Wang, Y.-G. Wang and H.-Y. Sun, "The effect of Co content on the structure and the magnetic properties of CoxNi1x nanotubes", *Journal of Magnetism and Magnetic Materials*, Vol. 419, 06 2016.

149. Fan, H. M., J. Yi, Y. Yang, K. Kho, H.-R. Tan, Z.-X. Shen, J. Ding, X. Sun, M. Olivo and Y. P. Feng, "Single-Crystalline MFe2O4 Nanotubes/Nanorings Synthesized by Thermal Transformation Process for Biological Applications", *ACS nano*, Vol. 3, pp. 2798–808, 09 2009.

150. Kurlyandskaya, G., S. Bhagat, C. Luna and M. Vazquez, "Microwave absorption of nanoscale CoNi powders", *Journal of Applied Physics*, Vol. 99, 05 2006.

151. Toneguzzo, P., G. Viau, O. Acher, F. Fiévet-Vincent and F. Fiévet, "Monodisperse Ferromagnetic Particles for Microwave Applications", *Advanced Materials*, Vol. 10, No. 13, pp. 1032–1035, 1998.

152. Guo, J., M. Lan, S. Wang, Y. He, S. Zhang, G. Xiang and F. Boi, "Enhanced saturation magnetization in buckypaper-films of thin walled carbon nanostructures filled with Fe3C, FeCo, FeNi, CoNi, Co and Ni crystals: the key role of Cl", *Phys. Chem. Chem. Phys.*, Vol. 17, 06 2015.

153. MAtweb, "Elgiloy® Properties", `http://www.matweb.com/search/DataSheet.aspx?`, online; accessed 1 January 2020.

154. Caloz, C. and A. Rennings, "Overview of Resonant Metamaterial Antennas",

2009 3rd European Conference on Antennas and Propagation, pp. 615–619, 2009.

155. Vorobyev, A. Y. and C. Guo, "Enhanced absorptance of gold following multi-pulse femtosecond laser ablation", *Phys. Rev. B*, Vol. 72, p. 195422, Nov 2005, https://link.aps.org/doi/10.1103/PhysRevB.72.195422.

156. Vorobyev, A. and C. Guo, "Colorizing Metals with Femtosecond Laser Pulses", *Applied Physics Letters*, Vol. 92, pp. 041914–041914, 01 2008.

157. Vorobyev, A., A. Topkov, O. Gurin, V. Svich and C. Guo, "Enhanced absorption of metals over ultrabroad electromagnetic spectrum", *Applied Physics Letters*, Vol. 95, pp. 121106–121106, 09 2009.

158. Becker, W., R. Fettig and W. Ruppel, "Optical and electrical properties of black gold layers in the far infrared", *Infrared Physics Technology*, Vol. 40, pp. 431–445, 12 1999.

159. J Pokki, S. P. B. N. H. T., O Ergeneman, "Nanostructured spectrally selective absorber by colloidal lithography", *24th Micromechanics and Microsystems Europe Conference*, 09 2013.

160. Suzuki, M., T. Yamamoto, Y. Katayama, S. Kuwata and T. Tanaka, "Light Absorption by Metals with Porous Surface Layer Formed by Oxidization-Reduction Treatment", *Materials Transactions*, Vol. 53, pp. 1556–1562, 09 2012.

161. Estermann, M., L. B. McCusker, C. Baerlocher, A. Merrouche and H. Kessler, "A synthetic gallophosphate molecular sieve with a 20-tetrahedral-atom pore opening", , Vol. 352, No. 6333, pp. 320–323, Jul. 1991.

162. Arenas, J. and M. Crocker, "Recent Trends in Porous Sound-Absorbing Materials", *Sound vibration*, Vol. 44, pp. 12–17, 07 2010.

163. Bhattarai, K., S. Silva, K. Song, A. Urbas, S.-J. Lee, Z. Ku and J. Zhou, "Metama-

terial Perfect Absorber Analyzed by a Meta-cavity Model Consisting of Multilayer Metasurfaces", *Scientific Reports*, Vol. 7, 05 2017.

164. Lekner, J., "Light in periodically stratified media", *J. Opt. Soc. Am. A*, Vol. 11, p. 2892, 11 1994.

165. Heavens, O. S., "Optical properties of thin films", *Reports on Progress in Physics*, Vol. 23, No. 1, pp. 1–65, jan 1960.

166. Marques, R., F. Martín and M. Sorolla, *Metamaterials with Negative Parameters: Theory, Design and Microwave Applications*, 01 2008.

167. Landau, L. D., E. M. Lifshitz and L. P. Pitaevskii, *Electrodynamics of continuous media; 2nd ed.*, Course of theoretical physics, Butterworth, Oxford, 1984, `https://cds.cern.ch/record/712712`.

168. Banerjee, S., M. Levy, M. Davis and B. Wilkerson, "Exact and Approximate Capacitance and Force Expressions for the Electrostatic Interaction Between Two Equal-Sized Charged Conducting Spheres", *IEEE Transactions on Industry Applications*, Vol. 53, No. 3, pp. 2455–2460, 2017.

169. Pokki, J., O. Ergeneman, K. Sivaraman, B. Ozkale, D. M. Zeeshan, T. Lühmann, B. Nelson and S. Pané, "Electroplated porous polypyrrole nanostructures patterned by colloidal lithography for drug-delivery applications", *Nanoscale*, Vol. 4, pp. 3083–8, 03 2012.

170. Federici, J., "Review of terahertz and subterahertz wireless communications", *Journal of Applied Physics*, Vol. 107, pp. 111101 – 111101, 07 2010.

171. Turkmen, M., S. Aksu, A. Cetin, A. Yanik and H. Altug, "Multi-resonant metamaterials based on UT-shaped nano-aperture antennas", *Optics express*, Vol. 19, pp. 7921–8, 04 2011.

172. Jiang, W., L. Yan, H. Ma, Y. Fan, J. Wang, M. Feng and S. Qu, "Electromagnetic wave absorption and compressive behavior of a three-dimensional metamaterial absorber based on 3D printed honeycomb", *Scientific Reports*, Vol. 8, 12 2018.

173. Shen, G., M. Zhang, Y. Ji, W. Huang, H. Yu and J. Shi, "Broadband terahertz metamaterial absorber based on simple multi-ring structures", *AIP Advances*, Vol. 8, p. 075206, 07 2018.

174. Davies, A., A. Burnett, W. Fan, E. Linfield and J. Cunningham, "Terahertz spectroscopy of explosives and drugs", *Materials Today*, Vol. 11, pp. 18–26, 03 2008.

175. Buron, J., D. Petersen, P. Bøggild, D. Cooke, M. Hilke, J. Sun, E. Whiteway, B. Jessen, P. Nielsen, O. Hansen, A. Yurgens and P. Jepsen, "Correction to Graphene Uniformity Conductance Mapping", *Nano letters*, Vol. 15, 12 2014.

176. Park, S., J. T. Hong, S. J. Choi, H. Kim, W. Park, S. Han, J. Park, S. Lee, D.-S. Kim and Y. Ahn, "Detection of microorganisms using terahertz metamaterials", *Scientific Reports*, Vol. 4, p. 4988, 05 2014.

177. Park, S., S. Cha, G. Shin and Y. Ahn, "Sensing viruses using terahertz nano-gap metamaterials", *Biomedical Optics Express*, Vol. 8, pp. 3551–3558, 08 2017.

178. Neu, J., B. Krolla, O. Paul, B. Reinhard, R. Beigang and M. Rahm, "Metamaterial-based gradient index lens with strong focusing in the THz frequency range", *Optics express*, Vol. 18, pp. 27748–57, 12 2010.

179. Zhao, X., J. Zhang, K. Fan, G. Duan, G. Metcalfe, M. Wraback, X. Zhang and R. Averitt, "Nonlinear terahertz metamaterial perfect absorbers using GaAs [Invited]", *Photonics Research*, Vol. 4, pp. A16–A21, 06 2016.

180. Schalch, J., G. Duan, X. Zhao, X. Zhang and R. Averitt, "Terahertz metamaterial perfect absorber with continuously tunable air spacer layer", *Applied Physics*

Letters, Vol. 113, p. 061113, 08 2018.

181. Chen, C., S. Can, J. Schalch, X. Zhao, G. Duan, R. D. Averitt and X. Zhang, "Integrated Air Spaced Terahertz Metamaterial Absorber with High Quality Factor", *2019 20th International Conference on Solid-State Sensors, Actuators and Microsystems Eurosensors XXXIII*, pp. 1549–1552, 2019.

182. Xin, X., H. Altan, A. Saint and D. Matten, "Terahertz absorption spectrum of para and ortho water vapors at different humidities at room temperature", *Journal of Applied Physics*, Vol. 100, pp. 094905–094905, 11 2006.